

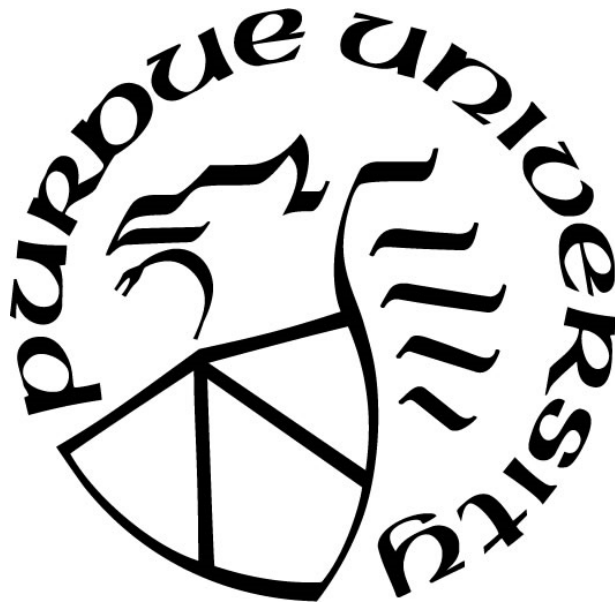
**NUMERICAL INVESTIGATION ON THE MECHANICAL PROPERTIES
OF NEAT CELLULOSE NANOCRYSTAL**

by
Mehdi Shishehbor

A Dissertation

*Submitted to the Faculty of Purdue University
In Partial Fulfilment of the Requirement for the degree of*

Doctor of Philosophy



Lyles School of Civil Engineering

West Lafayette, Indiana

December 2018

**THE PURDUE UNIVERSITY GRADUATE SCHOOL
STATEMENT OF COMMITTEE APPROVAL**

Dr. Pablo D. Zavattieri

School of Civil Engineering

Dr. Na Lu

School of Civil Engineering

Dr. Jeffrey Youngblood

School of Materials Engineering

Dr. George T. Chiu

School of Mechanical Engineering

Approved by:

Dr. Dulcy M. Abraham

Head of the Graduate Program

ACKNOWLEDGEMENTS

I would like to express my profound gratitude to my advisor and committee chair, Professor Pablo Zavattieri, for his guidance, motivation and patience during my Ph.D. His profound knowledge on solid mechanics and computational methods has been a valuable resource throughout my research. I am also extremely grateful to my examination committee members, Professor Jeffrey P. Youngblood, Professor George T. Chiu, and Professor Na Lu, for their insightful comments and inspiration. I would like to acknowledge financial supports by the Forest Products Laboratory under USDA grant: 07-CR-1111120-093, National Science Foundation through Grant No. CMMI-1131596 and CMMI- 1449358.

Last but not least, I would like to thank all my colleagues in Computational Multi-Scale Material Modeling Lab at Purdue University for their suggestions and contributions.

TABLE OF CONTENTS

| | |
|---|----|
| LIST OF TABLES | 7 |
| LIST OF FIGURES | 8 |
| ABSTRACT | 14 |
| CHAPTER 1. INTRODUCTION..... | 17 |
| 1.1 Objectives and Goals | 18 |
| CHAPTER 2. BACKGROUND..... | 23 |
| 2.1 Morphology, Dimension and Structure of CNCs | 23 |
| 2.1.1 Mechanical Properties | 25 |
| 2.2 Surface Properties | 27 |
| CHAPTER 3. MESOSACLE MODELING..... | 29 |
| 3.1 Introduction..... | 29 |
| 3.2 Molecular Dynamics (MD)..... | 32 |
| 3.3 CHARMM | 33 |
| 3.4 REAXFF | 35 |
| 3.5 Finite Element Method (FEM)..... | 36 |
| 3.5.1 Beam Element | 37 |
| 3.6 Coarse-Grained (CG) Modeling | 38 |
| CHAPTER 4. A CONTINUUM-BASED STRUCTURAL MODELING APPROACH .. | 40 |
| 4.1 Introduction..... | 40 |
| 4.2 Continuum-Based Structural Model | 43 |
| 4.3 Determination of The Main Parameters..... | 48 |
| 4.3.1 Cellulose Chain Mechanical Properties | 48 |
| 4.3.2 <i>H</i> -Bond Properties | 50 |
| 4.3.3 Stiffness of Vdw Element..... | 52 |
| CHAPTER 5. ANALYTICAL MODEL FOR ELASTIC PROPERTIES OF CNC | 56 |
| 5.1 Tensile Stiffness..... | 56 |
| 5.2 Shear Stiffness | 63 |

| | |
|--|-----|
| 5.3 Bending Stiffness | 66 |
| CHAPTER 6. THE EFFECT OF BONDED AND NON-BONDED INTERACTIONS ON THE MECHANICAL PROPERTIES..... | 70 |
| 6.1 Methodology | 70 |
| 6.2 Tensile Tests | 72 |
| 6.3 Shear Tests | 77 |
| 6.4 Bending and Torsion Tests | 81 |
| 6.5 Comparing MD, CM and Homogenization Models | 87 |
| 6.6 Summary and conclusion..... | 90 |
| CHAPTER 7. NEW COARSE-GRAINED MODEL FOR ELASTICITY, FRACTURE AND DEBONDING OF CNCS..... | 94 |
| 7.1 Introduction..... | 94 |
| 7.2 CG Model Representation..... | 97 |
| 7.3 CG Model Characterization | 105 |
| 7.3.1 Tensile Loading..... | 106 |
| 7.3.2 Adhesion Energy..... | 111 |
| 7.4 Evaluating The CG Parameters For Different Width of CNC..... | 115 |
| CHAPTER 8. VALIDATION TESTS FOR THE CG MODEL | 119 |
| 8.1 Bending of CNC | 119 |
| 8.2 Shear Between CNC Particles | 122 |
| 8.3 Tensile test of a small staggered structure | 125 |
| 8.4 Complementary Mechanical Tests..... | 127 |
| 8.5 Assembly of Small CNC Bundle | 129 |
| CHAPTER 9. THE EFFECT OF INTERFACE ON THE MECHANICAL PROPERTIES | 132 |
| 9.1 Fracture of A CNC Bundle | 134 |
| 9.2 Mechanical Properties of A Staggered Structure..... | 136 |
| 9.3 Mechanical Properties of A Bouligand Structure..... | 138 |
| 9.4 Summary and Conclusion..... | 141 |
| CHAPTER 10. THE EFFECT OF FIBER LENGTH AND ORIENTATION..... | 143 |

| | |
|---|-----|
| 10.1 Introduction..... | 143 |
| 10.2 Method | 146 |
| 10.2.1 Mechanical properties of the rotated film | 147 |
| 10.2.2 Generation of 3D RVE | 147 |
| 10.2.3 Fiber orientation distribution (FOD)..... | 150 |
| 10.2.4 Fiber length distribution (FLD)..... | 151 |
| 10.2.5 The Effect of Interfacial Properties | 153 |
| 10.3 Results and Discussion | 155 |
| 10.3.1 Mechanical Properties of The Rotated Film..... | 155 |
| 10.3.2 The effect of FOD | 160 |
| 10.3.3 The effect of FLD | 161 |
| 10.3.4 The effect of interfacial properties | 162 |
| CHAPTER 11. CONCLUSION | 164 |
| 11.1 Summary and Conclusion..... | 164 |
| 11.2 Future Works | 165 |
| APPENDIX A. COARSE GRAINING OF CRYSTALLINE NANO-CELLULOSE ... | 168 |
| APPENDIX B. MECHANICS OF CRYSTALLINE NANO CELLULOSE NANOFILM | 172 |
| REFERENCES | 179 |
| VITA | 192 |

LIST OF TABLES

| | |
|--|-----|
| Table 2.1 Properties of CNC and other reinforcement materials (Moon et al., 2011)..... | 26 |
| Table 2.2 Surface energy for dried CNC at different temperatures (Peng et al., 2013) ... | 28 |
| Table 3.1 Structure property relationship for polymer (Gates et al., 2005)..... | 30 |
| Table 6.1 Elastic properties of CNC based on spring-mass model..... | 88 |
| Table 7.1 Force field parameters for CG model of Cellulose I β | 115 |
| Table 8.1 Mechanical Properties from shear test..... | 125 |
| Table 8.2 Mechanical Properties of staggered structure..... | 127 |

LIST OF FIGURES

| | |
|---|----|
| <p>Figure 2.1 Atomistic structure of CNC (Nishiyama et al., 2002) Red spheres denote oxygen ions, gray spheres represent carbon ions and white spheres represent hydrogen ions. (a) 3D view, (b) CNC 3×3 (square) structure is used in this work. The origin and center chains in h-bond plane (c) Unit cell of CNC in x-y coordinate (d) View along the c-axis direction. The intra- and inter-chain h-bonds are shown in blue and green dash lines, respectively. Note that only a fraction of the total length is being showed. (e) h-bond energy depends on distance and angle between donor and acceptor as shown as R and θ respectively....</p> | 24 |
| <p>Figure 2.2 Mechanical properties of cellulose $I\beta$ in compare with other engineering materials are shown in Ashby plot of specific modulus-specific strength (Moon et al., 2011)</p> | 27 |
| <p>Figure 3.1 Modeling landscape for Engineering and science and different length and time sales.....</p> | 31 |
| <p>Figure 3.2 Schematics for different potential terms in CHARMM force field.....</p> | 34 |
| <p>Figure 3.3 A 3D beam element with 2 nodes and 6 degree of freedom per node.....</p> | 38 |
| <p>Figure 4.1 Schematics of the transition from atomistic to continuum by replacing chains with beams, in-plane non-bonded interactions (h-bond and VdW) with in-plane surface and inter-plane non-bonded interactions with Inter-plane surface. (a) Representation of beams and in-plane surface replacing chains and in-plane non-bonded interactions (h-bond and VdW). The small blue spheres represent the beam element nodes (b) 3D representation of continuum model for beam, in-plane and inter-plane surfaces. (c). The cross-section of the 3x3 CNC with intra-plane and inter-plane surfaces shown in green and red colors with k_2 and k_1 as their stiffness respectively.....</p> | 45 |
| <p>Figure 4.3 Finding the mechanical properties of a single chain from MM (a) simple tension test on a single chain (b) Applying torsion displacement to a single chain (c) Applying two bending displacement around x and y axis on a single chain.</p> | 50 |
| <p>Figure 4.4 h-bond stiffness (represented as blue and green contour for inter-chain and intra-chain h-bonds respectively) for the unit cell of CNC structure. Stiffness values are in Kcal/mole-Å². (a) Reduced view along the a-axis (b) View along the c-axis (perpendicular to the page).....</p> | 52 |
| <p>Figure 4.5 Force per length-displacement curves for VdW forces between two Chains with different lengths. (a) Tangential force-displacement response for inter-plane VdW forces (b) Normal force-displacement response for inter-plane VdW forces (c) Tangential force-displacement response for in-plane VdW forces (d) Normal force-displacement response for in-plane VdW forces.</p> | 54 |

Figure 5.1 Schematic representation of the conversion from an atomistic model to a 1D spring model for (a) center plane and (b) origin plane (See Figure 2.1). In the top figure inter-chain h-bonds replaced by linear springs. In middle figure cellulose chains replaced by bar members. In bottom figure 1D model in axial direction is obtained. 58

Figure 5.2 (a) Normalized stiffness (ΔS) as function of α and number of chains (b) Variation of s parameter and elastic modulus with respect to size of CNC (m). 60

Figure 5.3 2D representation of the 3x3 CNC for tensile loading. Chains are shown with blue circles, stiffness in h-bond direction with green spring and stiffness in VdW direction with red spring. The boundaries for applying and fixing displacement are shown in black rectangle. (a) Applying tensile displacement on top chains in the x direction, VdW direction, while the bottom chains are fixed. (b) Applying tensile displacement on right chains in the y direction, h-bond direction, while the left chains are fixed. 61

Figure 5.4 Simplified representation of the cellulose crystal to evaluate the elastic shear behavior: (a) Each cellulose chain is shown with blue circle, the inter-plane stiffness is represented by red springs and the in-plane stiffness by green springs in 3x3 crystal (b) shearxz model with red spring representing the inter-plane VdW forces (c) Shearyz model where red springs represent inter-plane stiffness and green springs show the in-plane stiffness. 65

Figure 5.5 Each cellulose chain is shown with blue circle in 3x3 crystal. Tension, compression forces induced at cross section due to bending of crystal. 67

Figure 5.6 Bending stiffness multiplier, f , for different size of CNC is plotted. The value of f for typical CNC size is 1.2-1.4 with average of 1.28 for $m=4$ with 41 chains. 69

Figure 6.1 Details of the MD model and boundary conditions for a 3x3 square CNC. (a) Tension, bending and torsion displacements are applied on right and left boundaries. The green, red and blue arrows show the direction of tensile, bending and torsion displacement. (b) Displacement for *shearxz* is applied parallel to h-bond plane on top surface, red arrow, while the opposite surface is kept fixed. Blue arrow shows the displacement direction for *shearxy* and the direction of tension displacement for *tensionxx* is shown with green arrow. (c) Displacement for *shearyz* is applied perpendicular to h-bond plane on right surface, red arrow, while the opposite surface is kept fixed. Green arrow shows the displacement direction for tension test in y-direction. 72

Figure 6.2 Stress-strain curves for tension test. Comparing Continuum Model (CM) with molecular dynamics (MD) with different rates. (a) x direction (b) y direction and (c) z direction 75

Figure 6.3 Stress-strain curves for shear tests from MD with different rates and CM with upper and lower bound obtained from upper and lower bound of stiffness respectively. (a) Stress-strain curves for *shearxy* (b) *shearxz* and (c) *shearyz* 79

Figure 6.4 Moment-curvature plots for bending of CNC obtained from MD and CM simulations with different rates and different stiffness respectively. (a) pure bending around y-axis, which is parallel to the h-bond plane. (b) Pure bending around x axis which is perpendicular to the h-bond plane..... 84

Figure 6.5 (a) Torque-twist angle per length curves for torsion test with different torsion frequencies for MD and continuum. (b) Same results in bending scale. 87

Figure 6.6 Moment-curvature plots for bending of CNC around x and y axis acquired from CM, MD and FEM simulations. The solid curves show MD results, dashed lines are FEM results and dashed-dot lines present CM results. The lines with blue and red color represent bending around y and x axis respectively..... 89

Figure 7.1 Justification of using two glucose units (disaccharide) per CG bead. (a) 180 degree rotation of successive glucose units around z axis (backbone chain) relative to the previous repeat unit are shown with green and blue colors. Slip-stick behavior of moving two cellulose chains with 1.038 nm frequency is due to sliding of same and opposite groups on top of each other. (b) Normalized force-displacement curves from AA MD simulation (black solid line) is compared with different CG bead representations. The frequency of the blue dashed line, representing CG model with 1 bead per two glucose units, is the same as AA frequency. 99

Figure 7.2 The structure of the Coarse-grained model. (a) Force-displacement curve for Morse potential which defines all bonds including covalent and weak bonds. The Instantaneous stiffness, bond strength and bond distance associated with bond strength are shown. (b) Replacing a two glucose units with one bead in a cellulose chain. (c) Cross section of CNC with diamond shape. The beads are shown with blue spheres which are connected with red and green breakable bonds, Ewb , to add directionality of Elasticity and strength in all directions (d) The side view of the CNC which shows the beads with blue spheres and the covalent bond which are connecting the beads in the cellulose chain direction with black lines..... 101

Figure 7.3 Tensile loading in the chain direction for parametrizing covalent bond. (a) tensile loading in the chain direction (b) tensile loading perpendicular to the chain direction for parametrizing weak bonds. (c) tensile loading perpendicular to the chain direction for parametrizing weak bonds. 108

Figure 7.4 Comparison of the surface energy for AA and CG models obtained from averaging 10 SMD simulations. (a) Front Surface ([0 0 1]). (b) Side Surface ([1 1 0]). 114

Figure 7.5 Stress-strain curves for CG model with different width and AA with 16 chains. (a) tensile loading in the chain direction (b) tensile loading in the [-1 1 0] direction. (c) tensile loading in the [1 1 0] direction 116

Figure 7.6 Stress-displacement curves for CG models with different with AA with 16 chains. (a) tensile loading in the $[-1\ 1\ 0]$ direction. (b) tensile loading in the $[1\ 1\ 0]$ direction (c) Strain localization of CG model with different size for tensile test in the $[-1\ 1\ 0]$ direction. 117

Figure 7.7 AA and CG adhesion energy Comparison. (a) Front Surface $[0\ 0\ 1]$ and (b) Side Surface $[-1\ 1\ 0]$ 118

Figure 8.1 Comparing the Moment-curvature curve for bending around x and y axis and torsion of CNC from AA and CG modeling. (a) Cross-section of the CNC and the x and y axis have been shown. (b) Moment-curvature curve for bending around x axis. (c) Moment-curvature curve for bending around y axis. 122

Figure 8.2 Force-displacement curves for shear tests from AA and CG modeling are shown in red and black color respectively (a) Shear test. (b) Small staggered structure. 124

Figure 8.3 Force-displacement curves for tensile test of Small staggered structure from AA and CG modeling (a) Small staggered structure. (b) Small staggered structure. 126

Figure 8.4 Comparing the CG parameters for twisted and untwisted interfaces. (a) Stress-strain curves for lateral tensile test (b) Stress-strain curves for longitudinal tensile test. 129

Figure 8.5 Conformational analysis of a 2×2 bundle of CNC by AA and CG modeling (a) curvature-time curves shows the change of twist per length for a bundle. (b) curvature-time curves shows the change of twist per length for an individual CNC inside a bundle. (c) Radial Pair distribution function for 30 A. (d) The twisted structure of the bundle from AA and CG models are shown. 131

Figure 9.1 Nano-indentation of a bundle of CNC (4×4) with 100 nm length (a) Force-displacement curve for different interface properties. (b) Comparing the normalized maximum force, stiffness and fracture energy for different interface properties. The values are normalized with respect to their values at $\epsilon c = 5.0$. (c) Different fracture mechanism for different interfacial strength. 136

Figure 9.2 Stress-Strain curves for staggered structure with different interface strength (a) stress-strain curve. (b) Comparing the normalized strength, elasticity and fracture energy for different interface properties. The values are normalized with respect to their values at $\epsilon c = 5.0$. (c) Different fracture mechanism for different interfacial strength. 138

Figure 9.3 Stress-Strain curves for Bouligand structure with different interface strength (a) stress-strain curve. (b) Comparing the normalized strength, elasticity and fracture energy for different interface properties. The values are normalized with respect to their values at $\epsilon c = 5.0$. (c) Different fracture mechanism for different interfacial strength. 140

Figure 10.1. (a) ‘Brick and mortar’ structure of CNC with 50% overlap length. The overlap length is shown with l_0 and the red dashed rectangle shows the building block (CNC) of the structure (b) Side view of the CG model for CNC (c) Cross section of the CG model for CNC. (d) Molecular structure of disaccharide representing 1 bead in our CG model. 148

Figure 10.2. Representation of the model. (a) CNC particles with different length, width and alignment are shown with random colors in a RVE under tensile test. (b) CG representation of the CNCs are shown with green beads. (c) Chemical representation of the CNC cross-section. 149

Figure 10.3. Two RVEs with two different fiber orientation distribution around the shear direction has been shown. The Herman’s parameter (S) for the RVEs with aligned and random particles are 0.9 and 0.05 respectively. 151

Figure 10.4. Two different FLDs with μL 20 and 60 nm and the corresponding RVEs have been shown. 153

Figure 10.5. Properties of the interface between two CNCs can be varied by changing depth parameter, ϵ , of the LJ potential. (a) The interaction between two CNCs are defined. (b) The force-displacement curves for different depth parameters. The maximum force, F_{max} , and stiffness, K , varies by changing the ϵ 154

Figure 10.6. The effect of loading direction (θ) on the mechanical properties of a 2D staggered film. (a) Elastic modulus. (b) Strength. (c) failure modes for $\theta=0^\circ$, 45° and 90° 156

Figure 10.7. Analytical models for rotated staggered structure of CNC. (a) Main directions and the arbitrary rotation direction (θ). (b) Adhesion between particles. (c) Separation of a mix mode to shear and normal mode. 158

Figure 10.8. Mechanical properties of neat CNC material for different Hermans parameter (S) are shown in red solid line and dashed black line for axial (alignment direction) and transverse direction respectively. (a) Strength, (b) Elastic modulus, (c) Work of fracture, and (d) Failure strain. 161

Figure 10.9. Mechanical properties of neat CNC material for different average length (μ) are shown in red solid line and dashed black line for axial and transverse direction respectively. (a) Strength, (b) Elastic modulus, (c) Work of fracture, and (d) Failure strain. 162

Figure 10.10. Mechanical properties of neat CNC material for different interfacial properties (ϵ/ϵ_0) are shown in red solid line and dashed black line for axial and transverse direction respectively. (a) Strength, (b) Elastic modulus, (c) Work of fracture, and (d) Failure strain. 163

Figure A.1. (a) Bio-inspired crystalline nano-cellulose toolkit. (b) The structure tab in the toolkit allows the user to choose different cross-sections and length for CNCs. (c) Different type and size of cross-section for CNCs are shown. The 6x6 diamond and hexagonal shapes have been mostly employed in the past.

169

Figure A.2. In composite tab, one can choose to generate a staggered or a bouligand structure. (a) In the Bouligand tab, the number of particles in each layer, the pitch angle between layers and the distance between CNCs in and between layers can be modified. (b) The 3D staggered structure can be generated with multiple options on the overlap length in each direction. 170

Figure A.3. The outputs from the tool is the generated structure in form of image and data structure and log files. (a) An example of generated Bouliagnd structure with 60 degree pitch angle. (b) the stress-strain curve for the tensile test. (c) Step-potential energy plot shows the variation of potential energy during the tensile test. (d) Step-pair energy plot illustrates the change in non-bonded energy during the tensile test. 171

Figure B.1 User could select a preset Crystalline Nano Cellulose Structures to speed up the visualization.

174

Figure B.2 Simulation details. (a) Options to choose different simulation time, temperature and visualization option. (b) Different visualization options are shown. 176

Figure B.3 Output of the tool (a) Stress-strain curve. (b) Potential energy-step curve .. 178

ABSTRACT

Author: Shishehbor, Mehdi. PhD

Institution: Purdue University

Degree Received: December 2018

Title: Numerical Investigation on the Mechanical Properties of Neat Cellulose Nanocrystal

Committee Chair: Pablo Zavattieri

Nature has evolved efficient strategies to make materials with hierarchical internal structure that often exhibit exceptional mechanical properties. One such example is found in cellulose, which has achieved a high order of functionality and mechanical properties through a hierarchical structure with an exceptional control from the atomic level all the way to the macroscopic level. Cellulose is present in a wide variety of living species (trees, plants, algae, bacteria, tunicates), and provides the base reinforcement structure used by organisms for high mechanical strength, high strength-to-weight ratio, and high toughness. Additionally, being the most abundant organic substance on earth, cellulose has been used by our society as an engineering material for thousands of years, and are prolific within our society, as demonstrated by the enormity of the world-wide industries in cellulose derivatives, paper/packaging, textiles, and forest products.

More recently, a new class of cellulose base particles are being extracted from plants/trees, cellulose nanocrystals (CNCs), which are spindle-shaped nano-sized particles (3–20 nm in width and 50–500 nm in length) that are distinct from the more traditional cellulose materials currently used (e.g. molecular cellulose and wood pulp). They offer a new combination of particle morphology, properties and chemical functionalities that enable CNCs for use in applications that were once thought impossible for cellulosic materials.

CNCs have shown utility in many engineering applications, for example, biomedical, nanocomposites, barrier/separation membranes and cementitious materials. To gain greater insight as to how best use CNCs in various engineering application areas, a comprehensive understanding of the mechanics of CNCs is needed. The characterization of the mechanical properties of nanomaterials via experimental testing has always been challenging due to their small size, resulting in large uncertainties related to testing near sensitivity limits of a given technique, the same is true when characterizing CNCs. For CNCs, to help offset limitations in experimental testing, numerical modeling has been useful in predicting the mechanical properties of CNCs. We present a continuum-based structural model to study the mechanical behavior of cellulose nanocrystals (CNCs), and analyze the effect of bonded and non-bonded interactions on the mechanical properties under various loading conditions. In particular, this model assumes the uncoupling between the bonded and non-bonded interactions and their behavior is obtained from atomistic simulations.

For large deformations and when there is interaction and dynamics of many particles involved, continuum models could become as expensive as MD simulations. In addition, it has been shown that traditional material models in the continuum mechanics context, cannot model all the mechanical properties of CNC, especially for large deformation. To overcome these setbacks and to be able to model real size of CNC, 50-1000 nm, and/or to increase the number of particles involved in the simulation, a so called “coarse-grained” (CG) model for mechanical and interfacial properties of CNC is proposed. The proposed CG model is based on both mechanical properties and crystal-crystal interactions. Parametrization of the model is carried out in comparison with all-atom (AA) molecular dynamics and experimental results of some specific mechanical and interfacial tests.

Subsequently, verification is done with other tests. Finally, we analyze the effect of interface properties on the mechanical performance of CNC-based materials including, bending of a CNC bundle, tensile load and fracture in bioinspired structure of CNCs such as staggered brick-and-mortar and Bouligand structures of interest.

CHAPTER 1. INTRODUCTION

(A version of this chapter is published <https://doi.org/10.1016/j.jmps.2017.11.006>)

In the past years, biodegradable composites have gained increasing interest for sustainable development due to their lower cost and environmental impact. Some natural fibers, from animal and plant sources, such as cellulose has been shown to be a good candidate to replace petroleum-based fibers due to their high performance (Jarvis, 2003; Klemm et al., 2005; Moon et al., 2011; Quesada Cabrera et al., 2011). These natural materials achieve a high order of functionality and mechanical properties through a hierarchical structure with an exceptional control from the atomic level to the macroscopic level. Cellulose is present in a wide variety of living species (trees, plants, bacteria, tunicates -a group of abundant saclike filter feeding organism found in the oceans), and provides the base reinforcement structure used by organisms for high mechanical strength, high strength-to-weight ratio, and high toughness (Moon et al., 2011). Being the most abundant organic substance on earth, cellulose has been used by our society as engineering materials for thousands of years, essentially for their immense benefits of cost, availability, processing, flexibility, light-weight properties and high mechanical performance (Klemm et al., 2011; Moon et al., 2011). CNCs have shown utility in many engineering applications (Grishkewich et al., 2017; Mariano et al., 2014; Moon et al., 2011), for example, biomedical (Klemm et al., 2011; Lin and Dufresne, 2014), nanocomposites (Huq et al., 2012; Mariano et al., 2014; Miao and Hamad, 2013; Yang et al., 2014), barrier/separation membranes (Carpenter et al., 2015), and cementitious materials (Cao et al., 2016a, 2016b, 2015). While these materials

have evolved for very specific purposes (e.g., structural support in plants, tree, etc.), the potential capacity of these materials to be used environmentally friendly and biocompatible products for advanced application has not yet been fully exploited. Moreover, the properties, functionality, durability and reliability that will be required for the next generation of cellulose based products and their engineering applications cannot be achieved with the traditional cellulose materials. In recent years, there has been a growing interest from the scientific community to understand the structure and properties of the CNCs. Besides thermo-elastic property predictions (Moon et al., 2011a; Dri et al., 2013; Dri et al., 2014; Dri et al., 2015), recently, it was shown that the dimensions of CNC particles are optimized for fracture energy and surface area-to-volume ratio (Sinko et al., 2014). In addition, interfacial study of CNC particles reveals that the contribution of both VdW interactions and hydrogen bonding responsible for the adhesion strength between CNCs (Sinko and Keten, 2015). Sinko and Keten also studied the shear and tensile failure of the interfaces between CNCs and proposed analytical model to describe their energy landscapes (Sinko and Keten, 2015). These examples demonstrate the utility of numerical modeling of gaining insight about the mechanisms that influence the mechanical behavior of CNCs.

1.1 Objectives and Goals

There are many aspects of CNCs that can affect the overall mechanical properties of the nanocomposite such as (1) mechanical properties of the individual CNC, (2) interfacial properties between CNCs, (3) volume content, (4) aspect ratio/length and (5) the degree of

CNCs alignment (fiber dispersion) (Moon et al., 2011). Our main objective is to develop and employ modeling approaches to study these features and facilitate production of CNC-based materials. To achieve this goal, first, having an appropriate model which captures the main mechanical and interfacial properties of CNC and is able to bridge the length and time scale is essential. Therefore, as a minor goal, first, new models for the mechanical and interfacial properties of CNC are developed. The minor goals can be explained as follow: Understanding the structure-property relationship for mechanical properties of CNC particles. In particular, understanding the effect of bonded (e.g., covalent bond) and non-bonded (e.g., h-bond and VdW forces) interactions on the overall mechanical properties help us to only retain the key interactions and have a more simplified model. A continuum-based structural model is developed that uncouples bonded and non-bonded interactions and substitutes them with an equivalent interaction model. The model is implemented under the finite element model (FEM) framework, and it allows us to better quantify the effect of bonded and non-bonded interactions on the overall elastic behavior of CNCs under various loading conditions, including axial loads, bending, torsion and shear. Ancillary MD simulations are employed to (i) inform the continuum model and (ii) verify some key results. For large deformations and when there is interaction and dynamics of many particles involved, continuum models could become as expensive as MD simulations. In addition, it has been shown that traditional material models in the continuum mechanics context, cannot model all the mechanical properties of CNC, especially for large deformation. To overcome these setbacks and to be able to model real size of CNC, 50-1000 nm, and/or to increase the number of particles involved in the simulation, a so called

“coarse-grained” (CG) model for mechanical and interfacial properties of CNC is proposed. After developing the appropriate model for CNC, we can study the mechanical properties of all-CNC materials.

Our main objective here is to study bio-inspired structure of CNC, which can particularly be achieved theoretically for now due to very small size of CNC particles. Here we investigate if there is any advantage in having such structure for CNC structure and understand the effect of interfacial properties on the overall mechanical performance.

This chapter was an introduction chapter to explain the motivation and objectives of this research.

Chapter 2 is a brief essential review on the structure and properties of the CNC. The focus is on the mechanical and interfacial properties of the CNCs.

In chapter 3, the need for meso-scale modeling is explained and different modeling approaches such as MD, FEM and coarse-graining are explained.

In chapter 4, a new model based on continuum-structural approach for elastic behavior of CNCs is explained. In particular, the model is able to separate bonded and non-bonded interactions to study their effect on the elastic properties.

In chapter 5, Analytical solution for elastic properties of defect free CNCs is developed. Developing such analytical solution alongside the continuum-structural model will help to understand the effect of defects on the elastic properties.

In chapter 6, we use the continuum-structural and analytical model to study the effect of bonded and non-bonded interactions on different mechanical tests, such as tensile, shear, bending and torsion. In addition, the effect of defects on some case studies is discussed.

In chapter 7, a new coarse-grained model for elastic, fracture and interaction properties of CNCs are developed. This chapter includes model representation and characterization.

In chapter 8, specific validation tests are performed on the model and compared with full atomistic modeling and existing experimental results.

In chapter 9, we apply our developed CG model to study the effect of interfacial properties on the bending of a CNC bundle and tensile behavior of bio-inspired structures such as Bouligand and brick-and-mortar structure of CNCs.

Chapter 10 investigates the effect of fiber length and orientation on the mechanical properties of CNC nanofilms.

Chapter 11 summarizes this dissertation, discusses the contribution of this study, explains the limitations and recommends possible future work.

CHAPTER 2. BACKGROUND

(A version of this chapter is published <https://doi.org/10.1016/j.jmps.2017.11.006>)

2.1 Morphology, Dimension and Structure of CNCs

Cellulose is a linear chain of 1-4 linked β -D glucopyranose and during the biosynthesis process, cellulose chains bundle together in highly ordered parallel stacking, forming crystalline regions (cellulose I) that have two distinct polymorphs called cellulose I α and I β . Cellulose I β is the more stable phase, dominant in plants and the focus of this study (Jarvis, 2003; Klemm et al., 2005; Quesada Cabrera et al., 2011), X-ray neutron diffraction studies concluded that Cellulose I β contains two cellulose chains in a monoclinic unit cells with different inter-chains *h*-bonding systems which can be distinguished by the so-called A and B *h*-bonding patterns (Nishiyama et al., 2002). We focus on cellulose I β with network A as the most commonly occurring polymorphs in higher plant cell wall (Moon et al., 2011). Figure 2.1 shows an schematics of an idealized CNC extracted from plants/trees, and is within the range of predicted CNC geometries having an estimated width of 2-3.5 nm, consisting of 18-36 chains and different proposed cross-sectional shapes (e.g. diamond, square or hexagonal) (Bergenstrale et al., 2007; Moon et al., 2011b; Zhao et al., 2013). The lattice parameters for cellulose have been experimentally measured by several authors (Nishiyama et al., 2002; Wada et al., 2004; Langan et al., 2005; Nishiyama et al., 2008), using different experimental techniques. For instance, for the cellulose I β with a network A structure, these unit cell values were reported (Nishiyama et al., 2002) to have the

following values: $a = 7.784 \text{ \AA}$, $b = 8.201 \text{ \AA}$, $c = 10.380 \text{ \AA}$, $\alpha = 90^\circ$, $\beta = 90^\circ$, $\gamma = 96.55^\circ$, with a 658.3 \AA^3 volume at 293 K (Fig. 1b-c). Cellulose I β has P21 symmetry and the layers

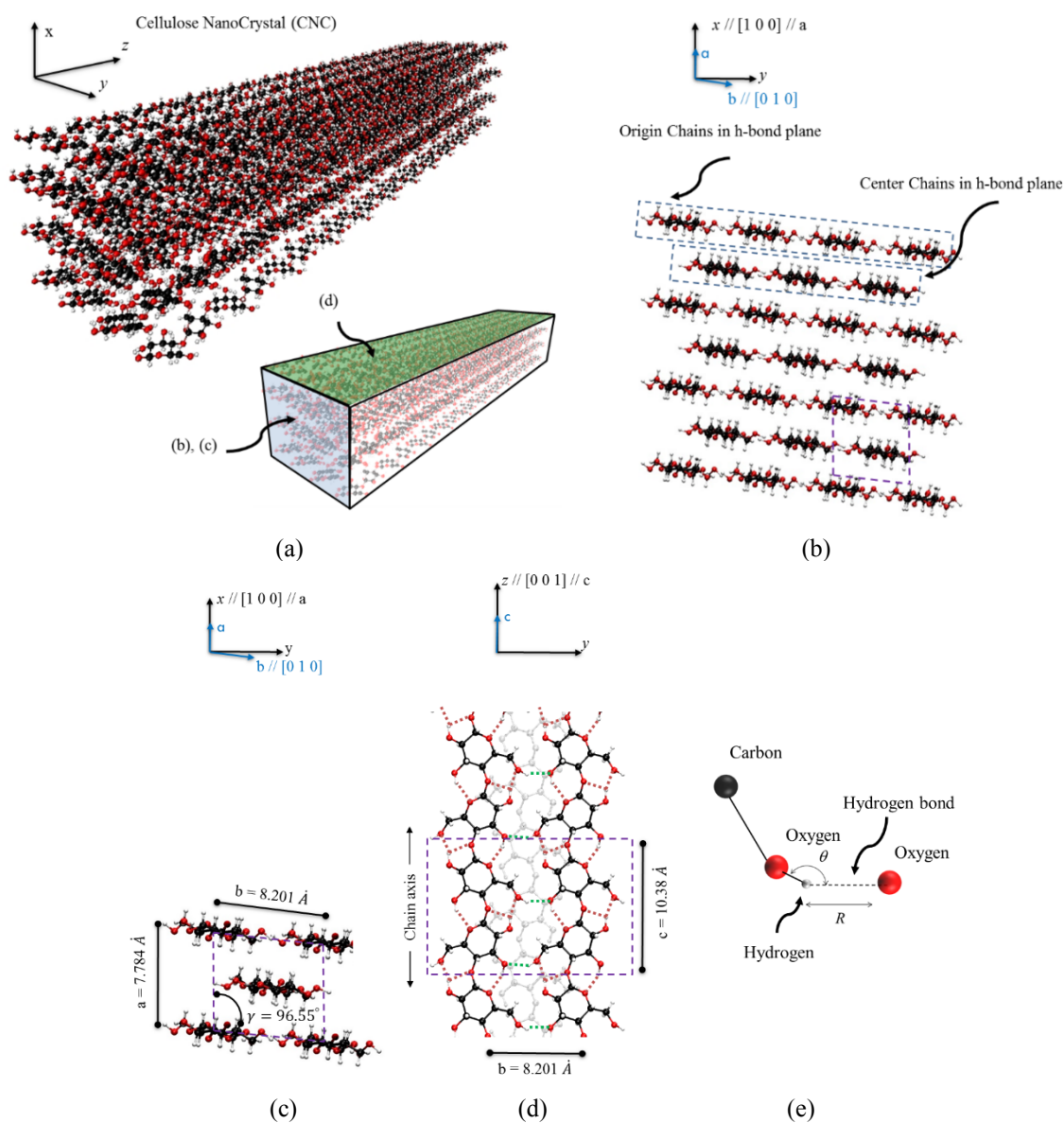


Figure 2.1 Atomistic structure of CNC (Nishiyama et al., 2002) Red spheres denote oxygen ions, gray spheres represent carbon ions and white spheres represent hydrogen ions. (a) 3D view, (b) CNC 3×3 (square) structure is used in this work. The origin and center chains in h-bond plane (c) Unit cell of CNC in x-y coordinate (d) View along the c-axis direction. The intra- and inter-chain h-bonds are shown in blue and green dash lines, respectively.

Note that only a fraction of the total length is being showed. (e) h-bond energy depends on distance and angle between donor and acceptor as shown as R and θ respectively.

are displaced along the c-axis alternatively by $+c/4$ and $-c/4$ forming the so-called center and origin chains respectively (Fig. 1b). Intra- and inter-chain h-bonds are shown in Fig. 1d based on the h -bond pattern A. The inter-chain h -bonding is dominant within the (200) plane, also known as “ h -bonded” plane. A schematics of the hydrogen bond is included in Fig. 1e. On the other hand, VdW forces are believed to contribute to the bonding within planes (110) and $(1\bar{1}0)$ with a lesser influence of the h-bonds.

2.1.1 Mechanical Properties

In addition to being biodegradable, having low density (1.6 gr/cm^3) and reactive surfaces; CNCs have exceptional mechanical properties such as high elastic modulus in axial direction (greater than Kevlar) that makes them promising reinforcement component (Moon et al., 2011). Table 2.1 compares the mechanical properties of CNCs such as strength, elastic modulus in axial and transverse direction with other reinforcement materials such as Kevlar, carbon nanotube and steel fiber. From the recent studies on the strength of CNCs, a range of 2-6 GPa from experiment (Iwamoto et al., 2009; Saito et al., 2013) and a range of 5-8 GPa from atomistic modeling (Wu et al., 2014) were suggested. In addition, new experimental (Wagner et al., 2016) and numerical methods such as density functional theory (Dri et al., 2013) classical forcefield (Wu et al., 2013) and reactive force field (Wu et al., 2014) on elastic modulus of CNCs, suggests a range of 150-200 GPa and 10-25 GPa for axial elastic modulus (E_A) and transverse elastic modulus (E_T) respectively.

Table 2.1 Properties of CNC and other reinforcement materials (Moon et al., 2011)

| Material | Density (g/cm ³) | Strength (GPa) | E_A (GPa) | E_T (GPa) |
|-----------------|------------------------------|----------------|-------------|-------------|
| Kevlar | 1.4 | 3.5 | 124-130 | 2.5 |
| Carbon fiber | 1.8 | 1.5-5.5 | 150-500 | - |
| Steel Wire | 7.8 | 4.1 | 210 | - |
| Carbon nanotube | - | 11-63 | 270-950 | 0.8-30 |
| CNC | 1.6 | 7.5-7.7 | 110-220 | 10-50 |

Figure 2.2 shows the Ashby plot for the specific strength versus specific elastic modulus for CNC, CN neat film and CN reinforced composites. The plot indicates that the mechanical properties of the CNC neat film ($E_A \cong 30$ GPa, $\sigma_f \cong 80$ MPa) and CN reinforced composites ($E_A \cong 40$ GPa, $\sigma_f \cong 400$ MPa) are much lower than the properties of the individual CNC (Moon et al., 2011; Reising et al., 2012). The possible reasons for this gap in the mechanical performance could be (1) weak interfacial properties for CNC-CNC and CNC-polymer. (2) low degree of CNCs alignments. (3) low aspect ratio of CNCs (Moon et al., 2011).

The fact that CNCs can naturally assembled into bouligand structure in addition to their excellent mechanical properties, have made them promising nanoparticle for bioinspired Bouligand composite.(Natarajan and Gilman, 2018). Bioinspired CNC films in the form of Bouligand and/or brick-and-mortar arrangement has been an active area of studies recently (Natarajan et al., 2018; Qin et al., 2017; Zhu et al., 2015).

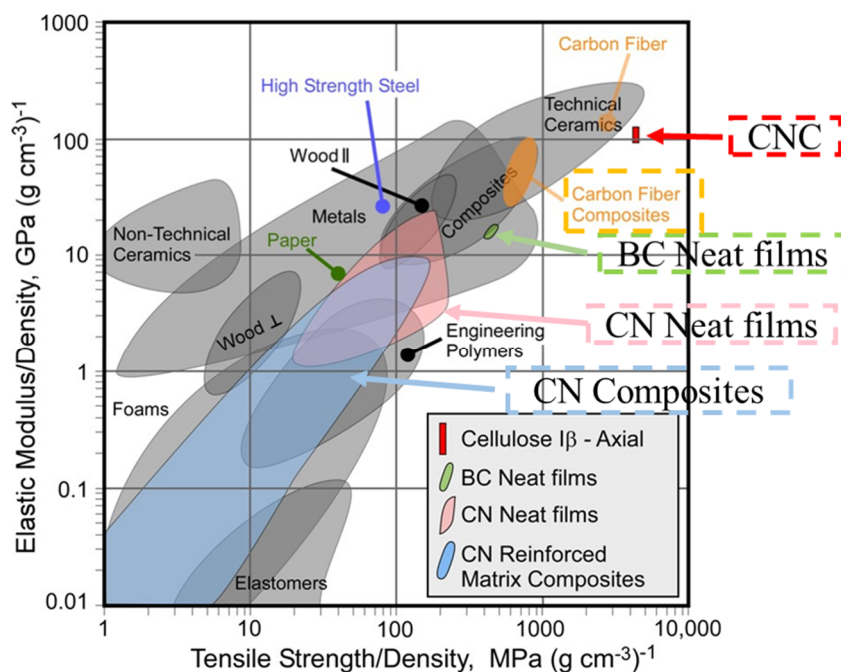


Figure 2.2 Mechanical properties of cellulose $I\beta$ in compare with other engineering materials are shown in Ashby plot of specific modulus-specific strength (Moon et al., 2011)

2.2 Surface Properties

Recently, Peng et al evaluated the effect of drying method and column temperature on the surface energy of dried CNCs using inverse gas chromatography and reported a range of 45-70 mJ/m² (Peng et al., 2013). Table 2.2 represents the surface energy of CNCs from different drying methods such as AD=air-drying, FD=freeze-drying and SD=spray-drying at different temperatures from 30 °C-60 °C (Peng et al., 2013).

Table 2.2 Surface energy for dried CNC at different temperatures (Peng et al., 2013)

| Drying method | Surface energy (mJ/m ²) | | | | |
|---------------|-------------------------------------|-------|-------|-------|-------|
| | 30 °C | 40 °C | 50 °C | 55 °C | 60 °C |
| AD | 68.5 | 61.4 | 55.6 | 53.2 | 50.2 |
| FD | 45.6 | 42.0 | 40.5 | 35.8 | 35.6 |
| SD | 59.7 | 58.2 | 55.5 | 53.2 | 51.3 |

CHAPTER 3. MESOSACLE MODELING

(A version of this chapter is published <https://doi.org/10.1016/j.jmps.2017.11.006>)

3.1 Introduction

Almost all biomaterials consists of hierarchical structures spanning from nanoscale to macroscale, and the overall macroscopic behavior are governed by the performance of these hierarchies at different length scale (Buehler, 2011, 2008a; Buehler and Ackbarow, 2007). In the materials science context, finding the structure-property relationship is essential for design of advanced materials (Gates et al., 2005). For example, Table 3.1 shows how for polymers and polymer-carbon nanotube composite, macroscopic properties are related to structural properties at different scales (Gates et al., 2005). However, for biological materials with multiple hierarchical scales, finding the structure-property relationship is very challenging as the material properties can become significantly size dependent (Buehler, 2008b).

Table 3.1 Structure property relationship for polymer (Gates et al., 2005).

| Structure | | | Property |
|-----------------------------|--------------------|-----------------|------------|
| Molecular | | Meso | Macro |
| Nano | Micro | Milli | |
| Inter-molecular interaction | Molecular weight | Volume fraction | Strength |
| Bond rotation | Cross-link density | Orientation | Modulus |
| Bond angle | Crystallinity | Dispersion | Glass temp |
| Chemical sequence | | | Viscosity |

To overcome this challenge, developing new methods that incorporates different length and time scale has been suggested (Buehler, 2011; Buehler and Ackbarow, 2007). In the past decades, there has been significant advances in largescale simulations in engineering and science due to enhanced computational tools and new numerical methods (Buehler, 2008b; Gates et al., 2005; Steinhauser, 2016). These advanced tools and methods that can bridge multiple length and time scale can facilitate undertaking the structure-property relationships of materials (Jancar et al., 2010; Karakasidis and Charitidis, 2007). At the smallest length (\AA -nm) and time scale (10^{-18} s- 10^{-15} s), Ab Initio calculations aim to solve the electronic structure of materials based on quantum mechanics (QM) and density functional theory (DFT) (Kohn et al., 1996; Steinhauser, 2016) as shown in Figure 3.1. Although DFT calculations is highly accurate and the methodology is very well-established, it is computationally very expensive and cannot model the systems beyond 100 atoms (Buehler and Ackbarow, 2007; Soler et al., 2002). To overcome the time and length scale

limitation of ab Initio calculations, molecular dynamic (MD) modeling was introduced (Buehler, 2008b; Steinhauser, 2016). Since in the MD method the effect of electrons are modeled implicitly through forcefields and the equation of motion for nuclei is solved by classical mechanics, they can model much larger systems (10^9 atoms) for larger time (10^2 s) and length (10^2 nm) scale (Buehler, 2008b) as shown in Figure 3.1.

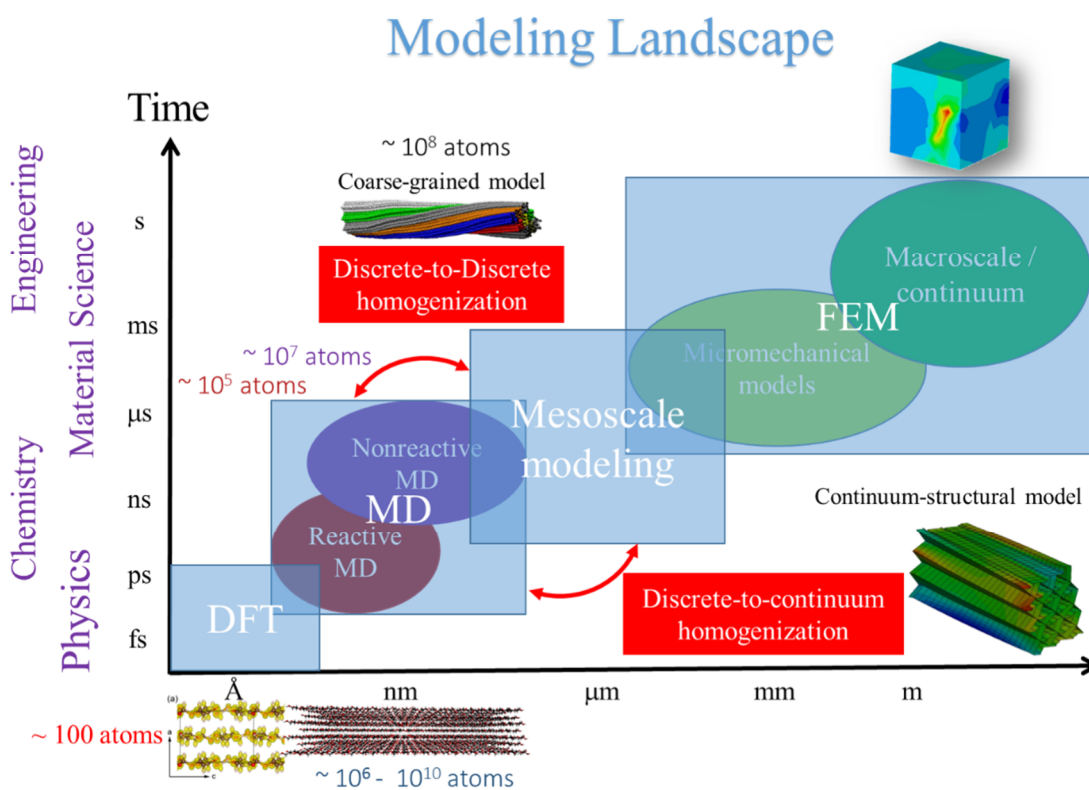


Figure 3.1 Modeling landscape for Engineering and science and different length and time scales.

3.2 Molecular Dynamics (MD)

Molecular dynamics (MD) method is atomist modeling tool that represents a material domain with discrete points (atoms) (Buehler, 2008b; Steinhauser, 2016). The fundamental assumption in MD method is Born-Oppenheimer approximation indicating that the motion of atomic nuclei and electrons can be separated due to significant difference in electron and nuclei masses ($\approx 1:1850$) (Buehler, 2008b). Based on this assumption, in MD method, only the motion of nuclei is calculated explicitly and the effect of electrons on the nuclei are modeled implicitly as force field potentials among nuclei (therefore, the words nuclei and atoms are synonymous in MD) (Buehler, 2008b). MD uses classical mechanics to calculate the dynamic trajectory of atoms, which interact through force field, according to Newton's law of motion $F=ma$, and by updating positions, velocities and accelerations from moment to moment (Buehler, 2008b). Since the potential energy is a function of atomic coordinates, $F=ma$ can be rewritten as:

$$m \frac{d^2 r_i}{dt^2} = -\nabla_{r_i} U(r_i), \quad i = 1 \dots N \quad (3.1)$$

Where U , r , t , m and N are potential energy, atomic coordinates, time, mass and number of particles respectively (Buehler, 2008b). Therefore, MD method finds the position of atoms by solving a system of second order nonlinear differential equations at each moment. From Equation 3.2, it can be concluded that defining the correct potential energy (Force fields) is the most crucial and challenging factor in MD models (Buehler, 2008b). Force fields are

set of mathematical equations and parameters for describing the interactions among atoms in MD simulations. Many different force fields have been utilized in the past to study cellulose nanocrystal (CNCs) including general hydrocarbon force fields such as GROMOS (Oostenbrink et al., 2004), AMBER (Wang et al., 2004), CHARMM (MacKerell et al., 2010), COMPASS (Sun, 1998) and GLYCAM06 (Kirschner et al., 2008). In addition to classical force fields, reactive force fields such as different REAXFF force fields have been used for mechanical and thermal properties of CNCs (Dri et al., 2015). In the following section CHARMM and REAXFF are discussed in more details as they are used in the following chapters for MD simulations.

3.3 CHARMM

The CHARMM force field (Brooks et al., 1983; MacKerell et al., 2010) has been widely used in the past for CNCs for conformational analysis, mechanical properties (Zhao et al., 2013) and interfacial properties (Sinko and Keten, 2015). In the traditional CHARMM model, the mathematical potential function is defined as follow (Buehler, 2008b):

$$\begin{aligned}
 U(\vec{R}) = & \sum_{bonds} k_b (b - b_0)^2 + \sum_{angle} k_\theta (\theta - \theta_0)^2 + \sum_{dihedrals} k_\chi (1 + \cos(n\chi - \delta)) + \sum_{UB} k_{UB} (S - S_0)^2 \\
 & + \sum_{impropers} k_{imp} (\phi - \phi_0)^2 + \sum_{nonbond} \epsilon \left[\left(\frac{R_{\min(i,j)}}{r_{ij}} \right)^{12} - \left(\frac{R_{\min(i,j)}}{r_{ij}} \right)^6 \right] + \frac{q_i q_j}{\epsilon_1 r_{ij}}
 \end{aligned} \tag{3.3}$$

Where k_b , k_θ , k_χ , k_{UB} and k_{imp} are the stiffness for bond, angle, dihedral angle, Urey-Bradley and improper angle respectively. The parameters b , θ , χ , S and ϕ are the bond length, bond angle, dihedral angle, 1-3 cross term and improper angle respectively (Buehler, 2008b). Figure 3.2 shows the schematics for different potential terms in the CHARMM force field.

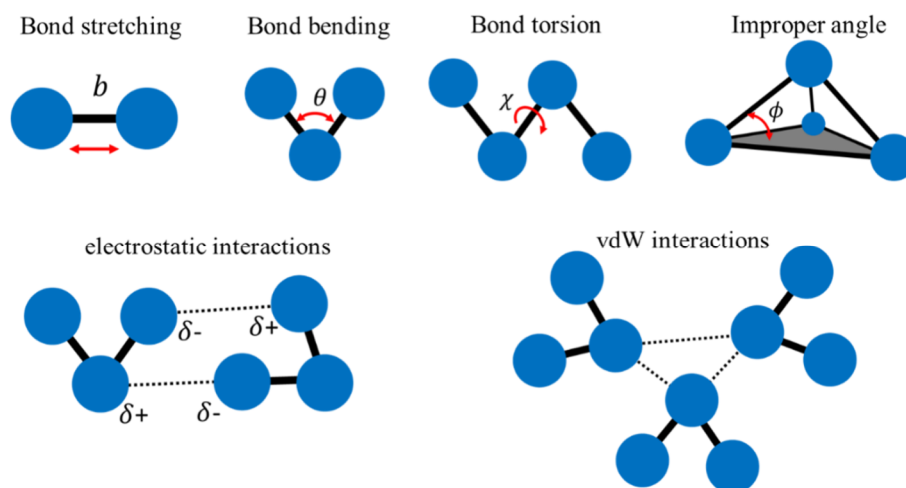


Figure 3.2 Schematics for different potential terms in CHARMM force field.

The last two terms in Equation 3.2, are nonbonded terms corresponding to van der Waals (vdW) and electrostatic interactions which are modeled by Lennard-Jones 6-12 (LJ) potential and Coulomb interaction respectively. For the nonbonded terms, ϵ represents LJ well depth, R_{min} is the distance for minimum LJ value, q is particle charge and ϵ_1 is effective dielectric constant (Buehler, 2008b). Note that the bonds in the CHARMM force field are defined through harmonic term and therefore, bond forming and bond breaking

cannot be modeled. In addition, the atomic charges are fixed throughout the simulation and no charge exchange can be modeled. Finally, in CHARMM force field, there is no explicit potential function for hydrogen bond (h-bond) and they are assumed to be implicitly modeled by LJ and Coulomb interactions (Buehler, 2008b).

3.4 REAXFF

Although classical force field are fast and accurate for elastic properties, they are not able to model bond breaking and new bond formation. To overcome this limitation, reactive force fields (Buehler, 2008b), such as ReaxFF, that describes interactions based on bond order have been introduced (Buehler, 2008b). In addition to quantum mechanical accuracy, ReaxFF force field provides charge exchange between atoms and explicit potential term for h-bonding (Buehler, 2008b; Shishehbor et al., 2018). However, with using more complex potential terms and charge exchange between atoms at each time step, comes 20-30 times higher computational cost than classical force fields (Buehler, 2008b). Although ReaxFF force field was first introduced for general hydrocarbons (Buehler, 2008b), today, it has been extend to variety of materials such as metals and semiconductors. For CNC, different ReaxFF parameters has been employed for conformational, mechanical and thermal properties (ReaxFF is available in LAMMPS package) (Dri et al., 2015). Recently, Dri. et al. investigated the competency of three different ReaxFF force fields, ReaxFF_{glycine} (Rahaman et al., 2011), ReaxFF_{mattsson} (Mattsson et al., 2010) and ReaxFF_{cho} (Chenoweth et al., 2008), for thermal-mechanical properties of CNC and recommended ReaxFF_{cho} for

elastic properties (Dri et al., 2015). In this work, we use $\text{ReaxFF}_{\text{cho}}$ for parameterization and characterization of our continuum-structural model in chapter 4.

3.5 Finite Element Method (FEM)

Finite element method (FEM) is the most prevalent numerical method in engineering and science for their simplicity and versatility. FEM is a systematic framework for solving a partial differential equation (PDE) in a definite domain and under specific boundary conditions (Fish and Belytschko, 2007; Zienkiewicz and Taylor, 2000). The systematic FEM steps for solving a general structural problem are as follow:

- 1- The PDE is transformed to the weak form and new set of boundary conditions is defined.
- 2- The domain is discretized in to finite domains called elements, which are connected together by so-called nodes.
- 3- The solution to the PDE in each element is approximated through trial interpolation functions (shape functions), e.g. Lagrange polynomials (Zienkiewicz and Taylor, 2000).
- 4- The parameter of the shape functions are obtained by satisfying the PDE and boundary conditions.

There are many different element types in FEM framework such as beam, shell and 3D solid (brick) elements for different applications. In this work beam elements are used to replace cellulose chains in the CNCs, therefore, only the beam element is explained below. Further information about FEM and other element types can be found in any elementary FEM books (Fish and Belytschko, 2007; Zienkiewicz and Taylor, 2000).

3.5.1 Beam Element

Beam elements are long structural members for carrying bending, torsion and axial deformation (Problems, 2007). Figure 3.3 shows a 3D beam element with 2 nodes and 6 degree of freedom (3 rotational and 3 translational). The Equilibrium equations for 3D Euler Bernoulli beam element for axial, bending and torsional deformation can be written as follow ((Dri, 2012; Problems, 2007):

$$EA \frac{d^2 u}{dz^2} = 0 \quad (3.4)$$

$$\frac{d^2}{dz^2} \left[EI_{11} \frac{d^2 v}{dz^2} \right] = 0 \quad (3.5)$$

$$\frac{d^2}{dz^2} \left[EI_{22} \frac{d^2 w}{dz^2} \right] = 0 \quad (3.6)$$

$$GJ \frac{d^2 q}{dz^2} = 0 \quad (3.7)$$

Where u , v , w and q are axial displacement, transverse displacement in y direction, transverse displacement in x direction and torsional displacement around z direction respectively. In addition, the behavior of the beam for each deformation can be individually described by EA , EI_{xx} , EI_{yy} and GJ for axial, bending around x , bending around y and torsion around z respectively.

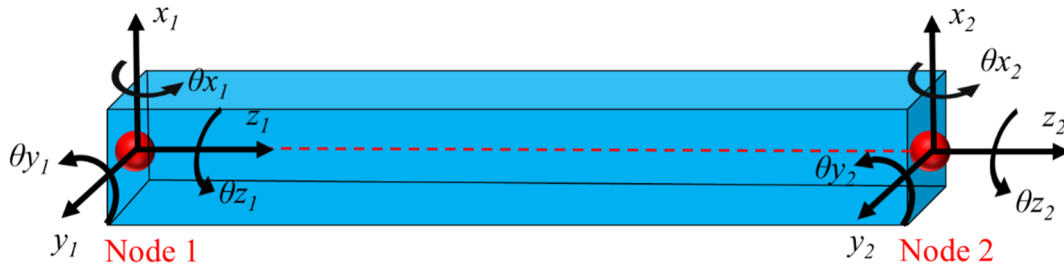


Figure 3.3 A 3D beam element with 2 nodes and 6 degree of freedom per node.

3.6 Coarse-Grained (CG) Modeling

In order to bridge the length and time scale from atomistic to continuum, developing mesoscale models that can transfer the important physics from atomic level to continuum is crucial. In the CG models several atoms are grouped together as one giant atom called bead to reduce the degree of freedom and therefore the computational costs (Buehler, 2008b). In typical coarse-graining approach, the total potential energy between beads consists of three terms (Buehler, 2008b): (1) stretching potential, (2) bending potential and (3) non-bonded potential and the parameters of the model is obtained by performing full atomistic modeling for specific tests. One the main questions regarding to a CG model is how coarse or fine a model should be in order to transfer the necessary physics and chemistry information to the up-scale. often this decision is made based on the properties of the interest on the macroscale and by assuming the structure-property relationships between the coarse and fine models. For coarse graining of a complex bio-macromolecule

such as CNC, understanding what interactions plays the crucial role on the structural and mechanical properties is essential.

CHAPTER 4. A CONTINUUM-BASED STRUCTURAL MODELING APPROACH

(A version of this chapter is published <https://doi.org/10.1016/j.jmps.2017.11.006>)

4.1 Introduction

Modeling approaches devoted to the prediction of the mechanical performance of nanomaterials can be divided into two major groups (i) atomistic, and (ii) continuum mechanics (Yakobson et al., 1996; Arroyo and Belytschko, 2002; Li and Chou, 2003; Arroyo and Belytschko, 2004; Cao and Chen, 2006; Jiang et al., 2006; Buehler, 2008; Sauer and Wriggers, 2009; Scarpa et al., 2009; Arash and Wang, 2014). Although atomistic approaches are a more appropriate in most cases for nano-scale simulations, they are very inefficient for large macromolecules or time span (Jiang et al., 2006; Li and Chou, 2003; Scarpa et al., 2009). Molecular dynamics (MD) solves the equation of motion for a large system of particles. The accuracy of MD simulations highly depends on appropriate choice of the force field (FF) that represents the interaction between the atoms (Matthews et al., 2012; Dri et al., 2015). FFs represent a set of mathematical functions, including their specific parameters, employed to describe the different bonded, e.g. covalent bonds, and non-bonded, e.g. hydrogen bonds and VdW forces, atomistic interactions in order to predict certain material properties. As more computer power has become available over the years, more sophisticated mathematical functions have been developed and employed to improve predictions. For instance, reactive force fields, such as ReaxFF (Van Duin et al., 2001),

which are based on bond length/order relationship, were developed and utilized intensely for various types of materials, mainly due to their ability to simulate bond forming and breaking, which is necessary for many mechanical investigations (Van Duin et al., 2001; T van Duin et al., 2003; Buehler, 2006; Chenoweth et al., 2008; Mattsson et al., 2010; Rahaman et al., 2011). These reactive force fields are also expected to be more accurate than classical non-reactive force fields, and closer to those predictions obtained with First principles density functional theory (QM-DFT) (Van Duin et al., 2001; Mattsson et al., 2010; Rahaman et al., 2011; Chenoweth et al., 2008; van Duin et al., 2003; Buehler, 2006). In particular, ReaxFF has an explicit hydrogen bond (*h*-bond) term that allows us to individually study its effect on the mechanical properties. Indeed, both QM-DFT and MD have been used to predict the mechanical behavior of CNCs. Recently, (Dri et al., 2013; Dri et al., 2014) employed QM-DFT with a semi-empirical correction for (VdW) interactions to reveal that the elastic properties of crystalline cellulose exhibits extreme anisotropy due to different type of dominant interactions, e.g. covalent, VdW and *h*-bond in different planes, for a wide range of temperatures. However, even for simple elastic properties, the competing contribution between bonded and non-bonded interactions remains to be studied in detail. MD has been undoubtedly the most predominant predictive tool for CNCs in the last few years (Kroon-Batenburg and Kroon, 1997; Neyertz et al., 2000; Eichhorn and Davies, 2006; Tanaka and Iwata, 2006; Bergenstrale et al., 2007). In particular, ReaxFF parameters have already been studied for CNCs (Wu et al., 2014; Dri et al., 2015) and compared with ab initio calculations for both conformational and mechanical analysis (Wu et al., 2014). In this paper, we employ the ReaxFF parameters

proposed by (Chenoweth et al., 2008) due to its superior performance on Young's modulus and lattice parameters of CNC among other ReaxFF parameters (Dri et al., 2015).

In contrast, continuum mechanics approaches are suitable to model large sized systems or time scale (Li and Chou, 2003; Buehler, 2008). However, turning a complex atomistic model into a simplified continuum or structural representation requires understanding of the governing mechanisms and physics at atomistic scale, which can be attained with atomistic modeling such as MD. In particular, continuum and structural mechanics have been used to model carbon nanotube and graphene in the past years following finite element frameworks (Yakobson et al., 1996; Arroyo and Belytschko, 2002; Li and Chou, 2003; Arroyo and Belytschko, 2004; Cao and Chen, 2006; Jiang et al., 2006; Scarpa et al., 2009; Lin et al., 2011; Arash and Wang, 2014). In these studies, either each individual covalent bond is modeled as a beam element (Li and Chou, 2003; Scarpa et al., 2009) or a group of atoms is simplified following a shell element formulation (Yakobson et al., 1996; Cao and Chen, 2006). However, the most important challenge for continuum models is to capture the non-local nature of interactions at nano-scale, e.g. VdW forces. For instance, non-local continuum theories were applied to the case of beam, plate and shell in the past (Arash and Wang, 2014). In some studies nonlinear springs based on Lennard-Jones (LJ) model were employed between each individual atoms to model VdW forces (Li and Chou, 2003). Deriving Constitutive cohesive equations for VdW forces based on LJ potential were also proposed by (Jiang et al., 2006). A finite element model (FEM) for nano-scale contact problems based on potential was proposed by (Sauer and Wriggers, 2009).

4.2 Continuum-Based Structural Model

The FF potentials typically used in MD and MM to account for the interaction between atoms are categorized into bonded and non-bonded terms (Tanaka and Iwata, 2006). In the proposed continuum-based structural model (or simply *continuum model*, CM), we follow a similar approach, and we assume that the bonded (i.e., covalent bonds) and non-bonded interaction (*h*-bonds and VdW forces) can also be decoupled. Previous works have shown that *h*-bonding and VdW interactions are the primary non-bonded interactions in CNC (Nishiyama et al., 2002; Kong and Eichhorn, 2005; Lindman et al., 2010; Sinko and Keten, 2015). While most atomistic models of CNC using classical FF describe the *h*-bonds as electrostatic interactions (Sinko and Keten, 2015), ReaxFF allows us to consider the *h*-bonding explicitly. Therefore, although other non-bonded terms are present in a FF (e.g. electrostatic term), their effects will be implicitly considered as a part of the VdW forces or covalent bond, for intra-chain and inter-chain interaction respectively. As such, the model consists on three main dominant interactions: the elastic behavior of the individual chain, the interaction of the chains on an *h*-bonded plane, and the interaction between *h*-bonded planes. The individual chains are considered to behave linearly elastic under infinitesimal strains. Additionally, due to their small thickness, the chains are assumed to undergo axial, torsional and bending deformation. As such, they are modeled as elastic beams. In a finite element framework, each chain is discretized with 3D Euler-Bernoulli (Fish and Belytschko, 2007) beam elements passing through the center of mass of the chain. Further analysis will validate these assumptions. A schematics of a beam element replacing two cellulose rings along a chain is shown in Figure 4.1a, b in blue. The beams main elastic

characteristics, which include tension stiffness, EA , bending stiffness, EI and torsional stiffness, JG , are obtained from atomistic simulation of a single isolated CNC chain. The elastic properties of each chain include the contribution of the covalent bonds, intra-chain h -bond and VdW forces between atoms inside a chain. While the schematic representation in Figure 4.1a, b depicts a beam element representing two glucose rings, the number of rings being represented by each element may be varied. A mesh sensitivity analysis addressing this point was carried out and included in Appendix A4. The h -bond and VdW interaction between chains lying on the h -bonded plane is modeled with special springs elements, intra-plane element, distributed along the chain direction as shown in Figure 4.1 with green color. In addition, inter-plane elements are developed to connect the first neighbor chains for inter-plane interactions, only VdW interactions, as shown in Figure 4.1 with red colors.

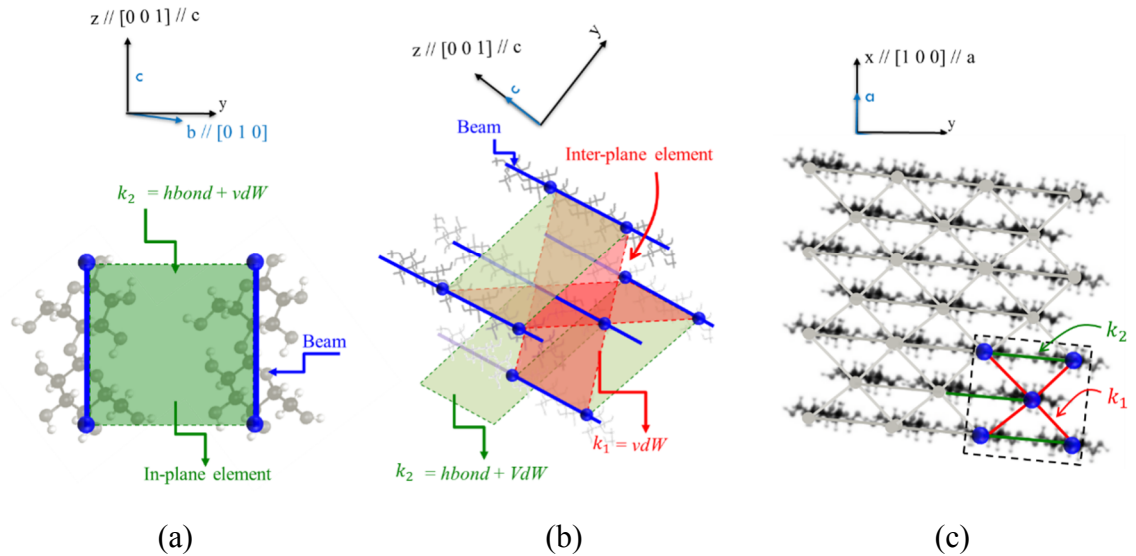


Figure 4.1 Schematics of the transition from atomistic to continuum by replacing chains with beams, in-plane non-bonded interactions (h-bond and VdW) with in-plane surface and inter-plane non-bonded interactions with Inter-plane surface. (a) Representation of beams and in-plane surface replacing chains and in-plane non-bonded interactions (h-bond and VdW). The small blue spheres represent the beam element nodes (b) 3D representation of continuum model for beam, in-plane and inter-plane surfaces. (c). The cross-section of the 3x3 CNC with intra-plane and inter-plane surfaces shown in green and red colors with k_2 and k_1 as their stiffness respectively.

Van der Waals forces are typically modeled by the Lennard-Jones (LJ) potential in MD simulations, when the distance between any two atoms is less than cutoff distance. While previous works have considered these types of non-local interactions in continuum models (Sauer and Wriggers, 2009; Arash and Wang, 2014), in this work we consider that only the nearest neighbor chains interact through VdW forces as shown in Figure 4.1. Considering the unit cell dimension in $[0\ 1\ 0]$ and $[1\ 0\ 0]$ directions, $b=8.201\ \text{\AA}$ and $a=7.784\ \text{\AA}$, respectively, the second nearest neighbor distance in $[0\ 1\ 0]$ direction, $12\ \text{\AA}$, is much larger than LJ equilibrium distance, σ , for C, O and H atoms, $\cong 6\sigma$, therefore there is almost no

VdW interaction between second neighbor in [0 1 0] direction (less than 0.01% of the well depth). For [1 0 0] direction the second nearest neighbor distance is 7.784 Å, which is still large enough, $\cong 4\sigma$, to be neglected (less than 0.1% of the well depth). We should also mention that the primary electrostatic interactions for CNC is hydrogen bonding (Nishiyama et al., 2002; Kong and Eichhorn, 2005; Lindman et al., 2010; Sinko and Keten, 2015), which has short-range effect and is modeled explicitly as *h*-bond. For systems such as ionic solids, where long-range interactions are important, the first nearest neighbor assumption will need be evaluated and replaced with a more sophisticated model (Marshall and Dayal, 2013). The overall effect of VdW forces between two nearest chains is applied on the beam elements passing through the center of mass of the chains (Figure 4.1). The constitutive equation for VdW element is similar to the *h*-bond element except that these elements connect the neighbor chains at different planes.

The finite element formulation is obtained from the principle of virtual work, which can be expressed as follows:

$$\int_V (b_i - \rho \ddot{u}_i) \delta u_i dV + \int_{\partial V} t_i \delta u_i d\Gamma = \int_V S_{ij} \delta \varepsilon_{ij} dV + \int_{\Gamma} R_{ij} T_{ij} (\delta u_i^+ - \delta u_i^-) d\Gamma \quad (4.1)$$

Where b is body forces on volume V , ρ is density, \ddot{u} is acceleration, t is boundary tractions on ∂V , u is displacement, S is second Piola-Kirchoff stress tensor ε is Green-Lagrange strain tensor, R local to global transformation matrix and u^+/u^- are displacement jumps between donor and acceptor when T is their traction forces in *h*-bond element. After

discretization, and in the absence of body force, Equation 4.2 can be solved with a time integration solver as follows.

$$M\ddot{u} = F_{ext} - F_{int} \quad (4.3)$$

Where M , F_{ext} and F_{int} are lump mass matrix, external and internal force vectors respectively. The explicit method is adopted to handle potential instabilities. For simplicity, the constitutive relations for traction-separation of h -bond and VdW forces are initially based on linear elastic response and are defined as:

$$T_i^h = K^h \delta_{ij} \Delta_j^h \quad (4.4)$$

$$T_i^v = K^v \delta_{ij} \Delta_j^v \quad (4.5)$$

Where T_i^h and T_i^v are traction forces, K^h and K^v are stiffness and Δ_j^h and Δ_j^v displacement jumps for h -bond and VdW elements respectively and δ_{ij} is Kronecker delta function.

Although the actual response of VdW and h -bond potentials are nonlinear, here we use instantaneous stiffness for the structure at equilibrium and limit our simulations to small deformations. Extension to nonlinear relationships based on LJ potentials can easily be implemented under the same framework and will be presented in future work.

4.3 Determination of The Main Parameters

4.3.1 Cellulose Chain Mechanical Properties

We carried out ancillary molecular mechanics (MM) simulations on a single cellulose chain to obtain the main mechanical properties needed for the continuum model. As the deformation of cellulose chains inside the CNC is mostly restricted by their interaction with neighboring chains, MD simulations of unconstrained single chains may not be a good option. In MM simulations, energy minimization is used to find a stable structure with minimum total potential energy. In particular, we extract the axial, bending, torsion and shear properties through specific tests such as simple tension, bending and torsion thought experiments. These MM simulations are done on single chains with different lengths using LAMMPS (Plimpton, 2007) with a ReaxFF force field and Hessian-free truncated Newton (hftn) algorithm for energy minimization (Plimpton, 2007). For each mechanical tests appropriate displacement is applied to all atoms in the chain and after energy-minimization the corresponding stiffness is obtained by relating total potential energy to stored strain energy in mechanics of solids (Li and Chou, 2003).

$$\frac{U_A}{L} = 0.5EA\epsilon^2, \quad \frac{U_M}{L} = 0.5EI\kappa^2, \quad \frac{U_T}{L} = 0.5GJ\kappa^2 \quad (4.6)$$

Where U_A , U_M and U_T are potential energy for tension, bending and torsion respectively and EA , EI and GJ are stiffness for tension, bending and torsion respectively, δ is

displacement, κ is curvature and L is the length of the chain. The results of these simulations are shown in Figure 4.2a, b and c. Assuming small strains problem, EA , EI and GJ can be obtained by parabolic data fitting of $U_A/L - \varepsilon$, $U_M/L - \kappa$ and $U_T/L - \kappa$ curves, respectively. According to the results, the parabolic equation for tension is $U_A/L = 15.5(nN) \varepsilon^2 - 0.0186(nN) \varepsilon + 1E - 4(nN)$, for bending is $U_M/L = -2.5(nN.nm^2) \kappa^2 + 0.8355(nN.nm) \kappa + 1E - 4(nN)$ and for torsion is $U_T/L = 0.8334(nN.nm^2) \kappa^2 + 0.0856(nN.nm) \kappa - 8E - 5(nN)$. Based on the obtained parabolic equations and Equation 4.7, the average stiffness values used in our continuum model are as follow:

$$EA = 31 \pm 2 nN, EI = 5.0 \pm 2 nN.nm^2, GJ = 1.5 \pm 0.5 nN.nm^2 \quad (4.8)$$

Where EA , EI and GJ are tension, bending and torsion stiffness of a single chain. As it can be inferred from the MM analysis suggest that the bending and torsional stiffness for single chain can be negligible in comparison with the axial stiffness.

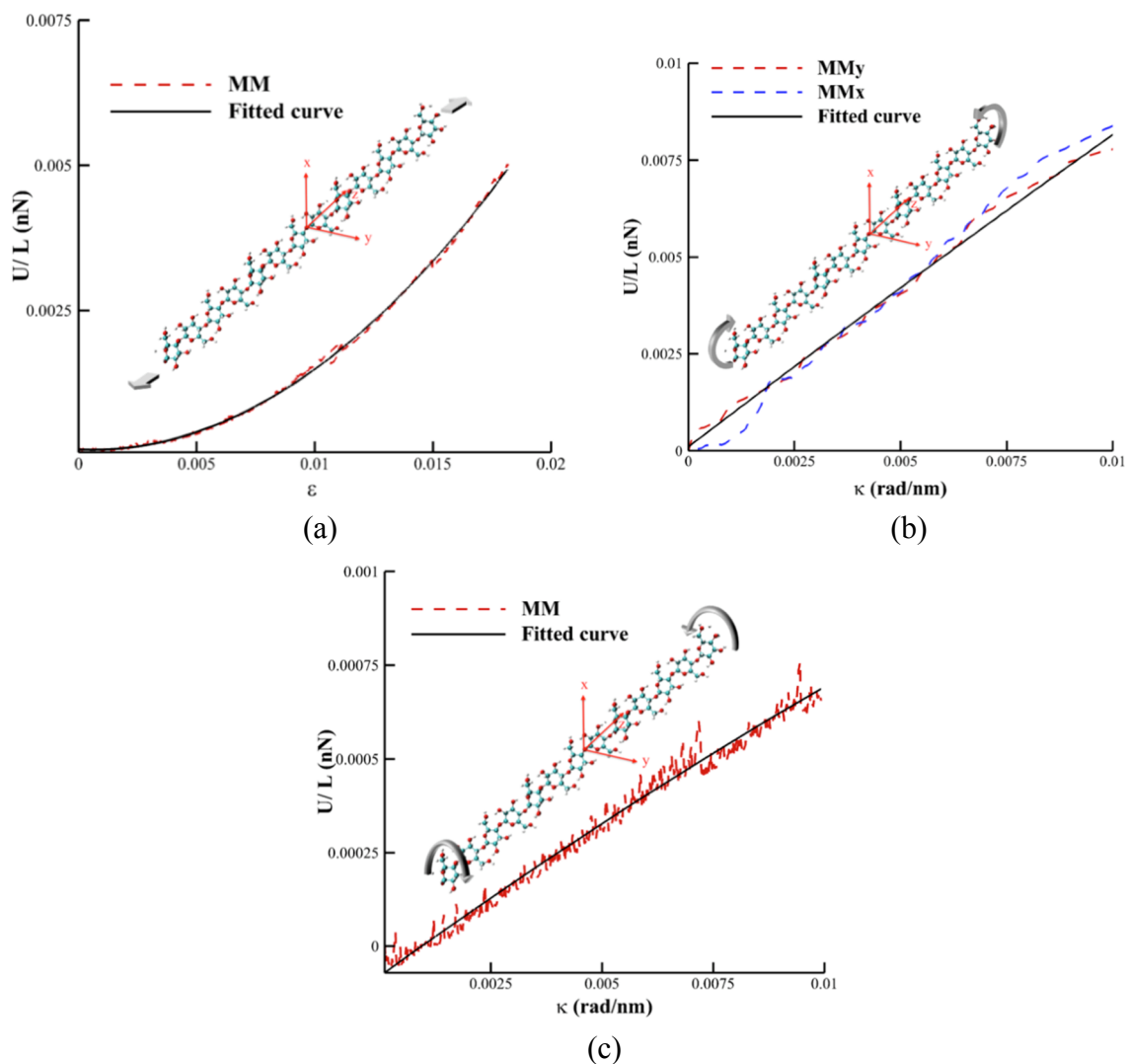


Figure 4.2 Finding the mechanical properties of a single chain from MM (a) simple tension test on a single chain (b) Applying torsion displacement to a single chain (c) Applying two bending displacement around x and y axis on a single chain.

4.3.2 *H*-Bond Properties

As previously discussed, ReaxFF has an explicit *h*-bond term that allows us to individually study its effect on the mechanical properties. To obtain *h*-bond properties for our continuum model the potential energy contribution for each *h*-bond in ReaxFF (Van Duin et al., 2001), which is defined as below, is employed.

$$U_{H-Bond} = P_{hb1} \times (1 - e^{-P_{hb2} \times BO}) \times e^{-P_{hb3} \times (\frac{R_0}{R} + \frac{R}{R_0} - 2)} \times \sin^4\left(\frac{\theta}{2}\right) \quad (4.9)$$

Parameters P_{hb1} , P_{hb2} , P_{hb3} and R_0 are exclusive parameterization used in each ReaxFF force field whereas BO, Bond Order, R, distance between donor and acceptor, and θ , h -bond angle, depend upon the geometry configuration.

The second derivative of the potential energy with respect to the interatomic distance between donor and acceptor (R) provides the stiffness of the h -bond, which is the main parameter for h -bond element in our continuum model.

$$K_{R-HBond} = P_{hb1} \times (1 - e^{-P_{hb2} \times BO}) \times \sin^4\left(\frac{\theta}{2}\right) \times [P_{hb3}^2 \times \left(-\frac{R_0}{R^2} + \frac{1}{R_0}\right)^2 - P_{hb3} \left(\frac{2R_0}{R^3}\right)] \times e^{-P_{hb3} \times (\frac{R_0}{R} + \frac{R}{R_0} - 2)} \quad (4.10)$$

Note that, since the variation of h -bond angle is small for infinitesimal deformations and the value for $K_{\theta-Hbond}$ is much smaller than $K_{R-Hbond}$, only derivation with respect to R is explicitly considered in the model. Figure 4.3 represents the stiffness values for h -bond obtained based on Equation 4.11. However, the h -bond stiffness in our model (Figure 4.1) is defined as a set of distributed forces over the element length. To overcome this problem, we approximate the contribution of the h -bonds with an average stiffness value. There are two main inter-chain h -bonds per each cellulose ring with the values of 4.5 and 1.5

Kcal/mole-Å² as shown in Figure 4.3b. Therefore, by dividing the value of overall local stiffness of *h*-bond, 6 Kcal/mole-Å², by the length of a ring, 5.19 Å, the average stiffness value is obtained as 1.156 Kcal/mole-Å³ (8 nN/nm^2).

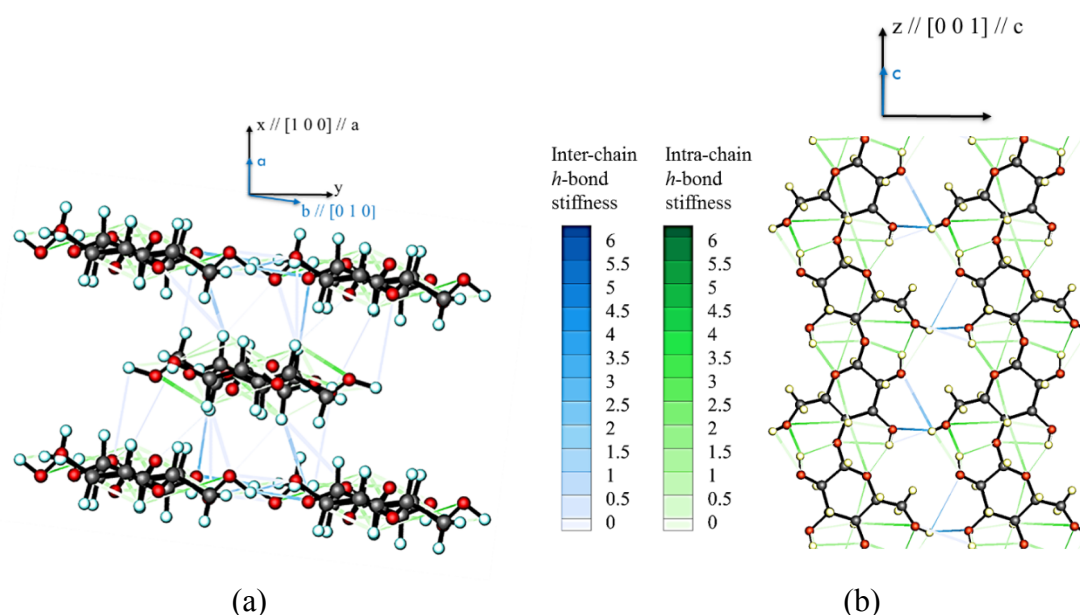


Figure 4.3 h-bond stiffness (represented as blue and green contour for inter-chain and intra-chain h-bonds respectively) for the unit cell of CNC structure. Stiffness values are in Kcal/mole-Å². (a) Reduced view along the a-axis (b) View along the c-axis (perpendicular to the page).

4.3.3 Stiffness of Vdw Element

To be able to find the stiffness of VdW element in normal and shear direction, MD analysis at 1 K has been done on two chains with different length (Figure 4.4). Note that the equilibrium distance of two chains in crystalline cellulose is different from the equilibrium distance of two isolated chains due to the presence of other chains in a crystal. Therefore, at the beginning, two chains are placed at the equilibrium distance of two chains in a crystal,

8.201 Å and 5.57 Å for center to center distance of in-plane and inter-plane chains respectively, and the position of the leftmost oxygen atoms in the left chain and rightmost oxygen atoms in the right chain are fixed during equilibrium. To ensure that only the VdW interactions are contributing in our calculations, the *h*-bond cut off distance is set to zero. Moving a chain in the normal and tangential direction while keeping the other chain fixed (at the leftmost oxygen atoms) and calculating the total force-displacement relationship, the VdW behavior and consequently stiffness in normal/tangential direction is obtained. The analysis was done for both intra-plane and inter-plane VdW interactions (shown in red and green colors respectively in Figure 4.1) to increase the accuracy of the model. It is worth to mention that here MD simulation is used over MM in order to have control on distance of two chains and to overcome local minimum potential energy barrier during separation.

Figure 4.4 represents the MD results for the normal (Figure 4.4b, d) and tangential (Figure 4.4a, c) directions for both intra-plane (Figure 4.4a, b) and inter-plane (Figure 4.4c, d) chains. The analysis was done for chains with different degree of polymerization (DP represents the number of monomeric units in a cellulose chain) 12, 24 and 48 to understand the effect of chain length on the results. Although the force-displacement relationship in both normal and tangential directions is nonlinear, our results in Figure 4.4a and c suggest that force-displacement behavior can be assumed linear for infinitesimal deformations (i.e., 5% strain) around the equilibrium point. For the VdW stiffness in the normal direction, the stiffness at equilibrium distance of two chains in the crystal (not the equilibrium distance

of two isolated chains) has been used to reduce the error associated with the nonlinearity of VdW forces in the normal direction (dashed black line in Figure 4.4).

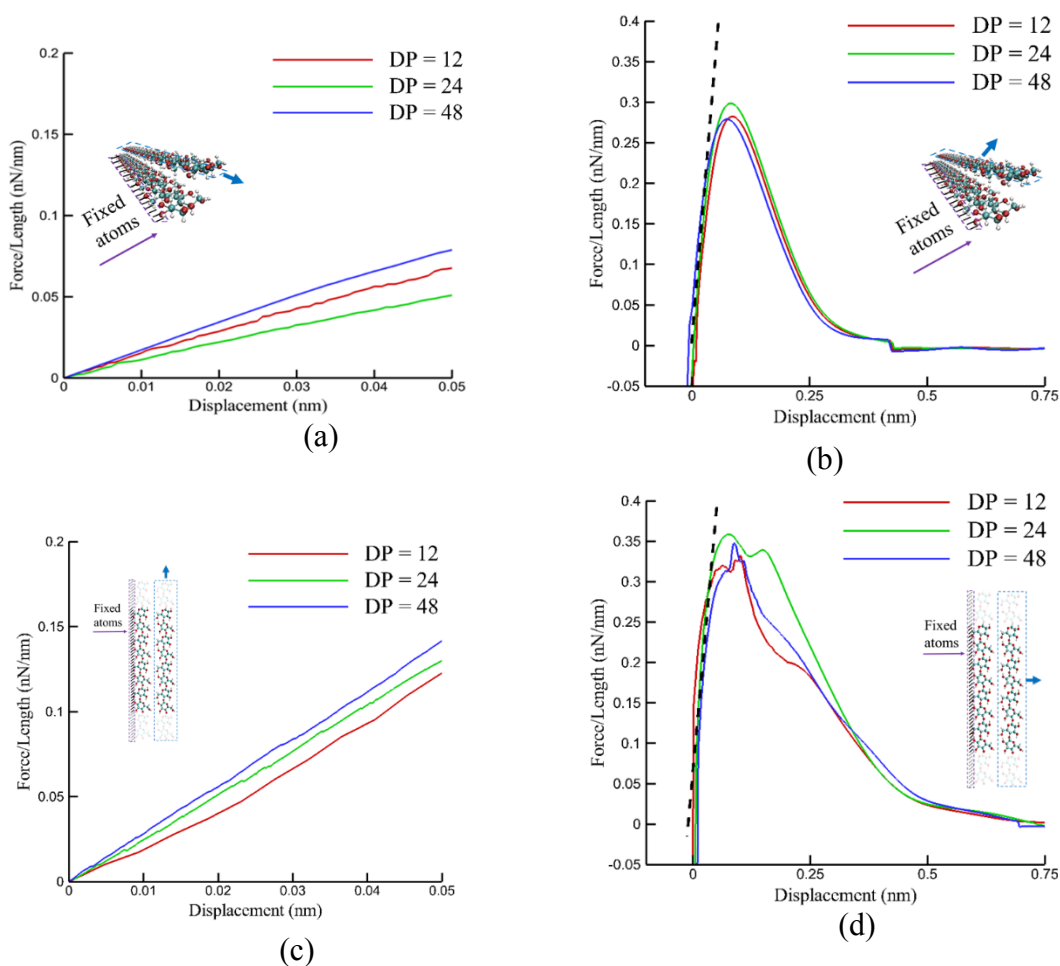


Figure 4.4 Force per length-displacement curves for VdW forces between two Chains with different lengths. (a) Tangential force-displacement response for inter-plane VdW forces (b) Normal force-displacement response for inter-plane VdW forces (c) Tangential force-displacement response for in-plane VdW forces (d) Normal force-displacement response for in-plane VdW forces.

The non-bonded stiffness values used in our continuum model for inter- and intra-plane element are given by the following expressions:

$$K_{1n} = 7.0 \pm 2.0 \frac{nN}{nm^2}, \quad K_{1t} = 1.7 \pm 0.3 \frac{nN}{nm^2} \quad (4.12)$$

$$K_{2n} = 14.0 \pm 2.0 \frac{nN}{nm^2}, \quad K_{2t} = 2.5 \pm 0.5 \frac{nN}{nm^2} \quad (4.13)$$

Where K_{1n} and K_{1t} are the inter-plane non-bonded stiffness in normal and tangential direction, respectively; while K_{2n} and K_{2t} are the in-plane non-bonded stiffness in normal and tangential direction, respectively. Note that K_{2n} in Equation 4.14 also includes $8nN/nm^2$ for the h -bond stiffness.

CHAPTER 5. ANALYTICAL MODEL FOR ELASTIC PROPERTIES OF CNC

(A version of this chapter is published <https://doi.org/10.1016/j.jmps.2017.11.006>)

5.1 Tensile Stiffness

We present a simple analytical model to understand the effect of inter-chain h -bond and to support the comparison between the CM and MD models. Figure 5.1a and Figure 5.1b represent simple spring model for inter-chain h -bond for the center and origin chains respectively (See Figure 2.1). Covalent and intra-chain h -bonds in each chain are modeled together as one elastic bar, green lines in Figure 5.1, and inter-chain h -bonds are replaced with springs, which are shown in Figure 5.1 as blue springs. Based on the orientation of inter-chain h -bonds in center planes, both chains and h -bonds contribute to the axial stiffness. However, only the chains contribute to the total stiffness in the origin planes due to the fact that the h -bonds are perpendicular to longitudinal axis. While value for stiffness for the chains can be obtained directly from the MD results presented in chapter 4, the stiffness of each spring can be assumed to be αk , where α is a dimensionless coefficient and k the stiffness of each chain. As such, the total stiffness, K_{t1} , and h -bonds stiffness, K_{h1} , of the one dimensional (1D) representation of the center plane shown in Figure 5.1a are obtained as follows:

$$\frac{1}{k_{t1}} = \frac{1}{3 \times 5k} + \frac{1}{2\alpha k + 3 \times 5k} + \frac{1}{3 \times 5k} + \frac{1}{2\alpha k + 3 \times 5k} + \frac{1}{3 \times 5k} \quad (5.1)$$

$$K_{t1} = \frac{75k + 10\alpha k}{25 + 2\alpha} \quad (5.2)$$

$$K_{h1} = 0.5 \times \left(\frac{75k + 10\alpha k}{25 + 2\alpha} - 3k \right) = \frac{2\alpha k}{25 + 2\alpha} \quad (5.3)$$

The total stiffness of the $m \times n$ crystalline cellulose can be obtained by taking into account the total number of chains, $(m + 1)(n + 1) + mn$, and *ID* representations, $m(n - 1)$, in the crystal.

$$K_t = K_h + K_c = m(n-1)K_{h1} + [(m+1)(n+1) + mn]k \quad (5.4)$$

Where K_h and K_c are the total contribution of inter-chain *h*-bond and chains in total stiffness respectively. To better show the inter-chain *h*-bond contribution, ΔS , is defined as the normalized inter-chain tensile stiffness over total tensile stiffness.

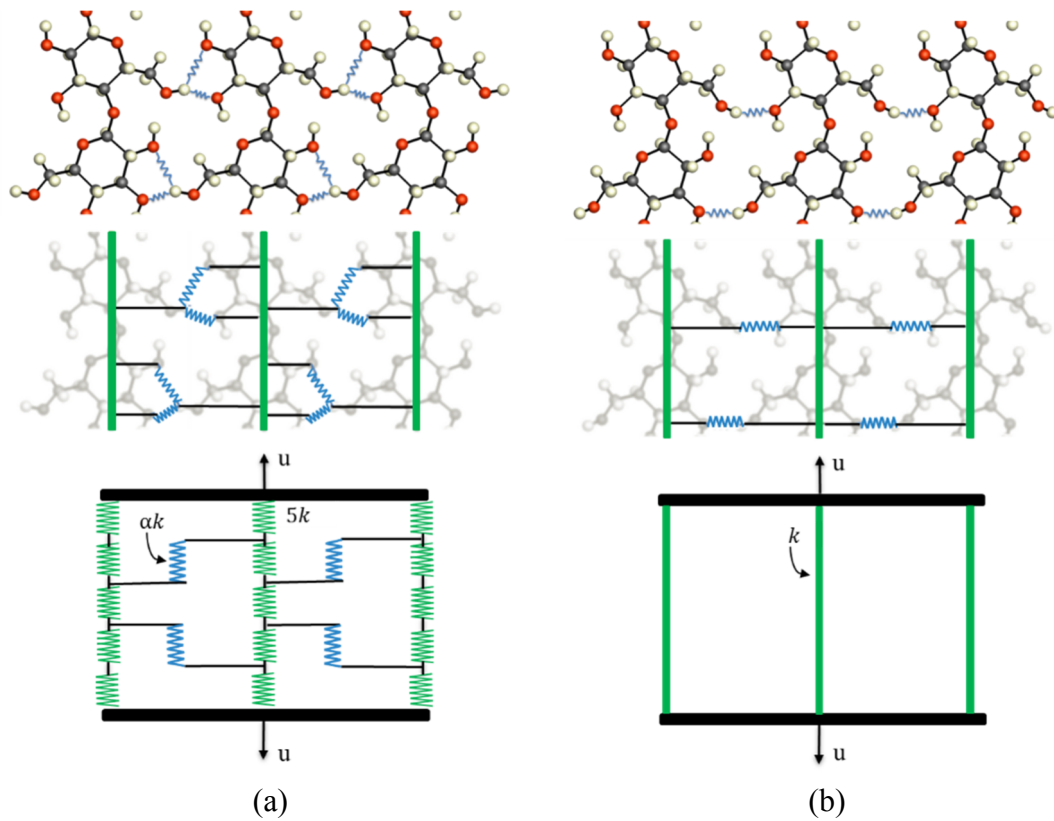


Figure 5.1 Schematic representation of the conversion from an atomistic model to a 1D spring model for (a) center plane and (b) origin plane (See Figure 2.1). In the top figure inter-chain h -bonds replaced by linear springs. In middle figure cellulose chains replaced by bar members. In bottom figure 1D model in axial direction is obtained.

$$\Delta S = \left(\frac{K_t}{K_c} - 1\right) \times 100 = \left(\frac{K_h}{K_c}\right) \times 100 \quad (5.5)$$

The variation of ΔS as a function of number of chains in a crystal and for different values of α is shown in Figure 5.2. Based on our MD simulation, Figure 5.2, the value of α is approximately 0.1, which translates into a total contribution of inter-chain h -bond to the total stiffness of less than 5% for any number of chains. Neglecting the term of the h -

bonds, and assuming that only the individual chain stiffness, K_c , contributes to the total stiffness, the elastic modulus of CNC in the chain direction can be directly estimated by dividing the total force carried by the chains by the CNC cross section area as follows:

$$E_z = \frac{\sigma_z}{\varepsilon_z} = \frac{F_z}{A_t \varepsilon_z} = \frac{[(m+1)(n+1) + mn]EA}{(ma \times nb)} \quad (5.6)$$

Where A_t is the cross section Area, F_z is the total force in the chain direction, which is obtained by the product of total stiffness, K_c , and displacement. The expression in Equation 5.7 is obtained by replacing k in Equation 5.8, by EA/L , and cross section area by $(ma \times nb)$. Assuming that the stiffness of an individual chain, EA , only depends on its length and not on the size of crystal (e.g., m and n parameters), E_z can be e rewritten as:

$$E_z = s \cdot \frac{EA}{ab} \quad (5.9)$$

Where $s = [(m+1)(n+1) + mn]/mn$ is a size dependent parameter. For instance, for a 3×3 case, with $a=0.8201 \text{ nm}$, $b=0.7784 \text{ nm}$ and $EA = 31 \pm 2 \text{ nN}$, we obtain $E_z = 134 \pm 8 \text{ GPa}$. In addition, the size dependence of E_z can be analyzed by plotting s as a function of m , as seen in Figure 5.2b. The size parameter, s , varies from 5 for a value of $m = 1$ and $E_z = 250 \text{ GPa}$, to an asymptotic value of 2 for large CNC size and $E_z = 100 \text{ GPa}$. The typical size associated with a typical CNC size is indicated in Figure 5.2b with green rectangle

suggesting a range of E_z between 115 and 135 GPa. This range of values agrees with what has been reported in the literature previously.

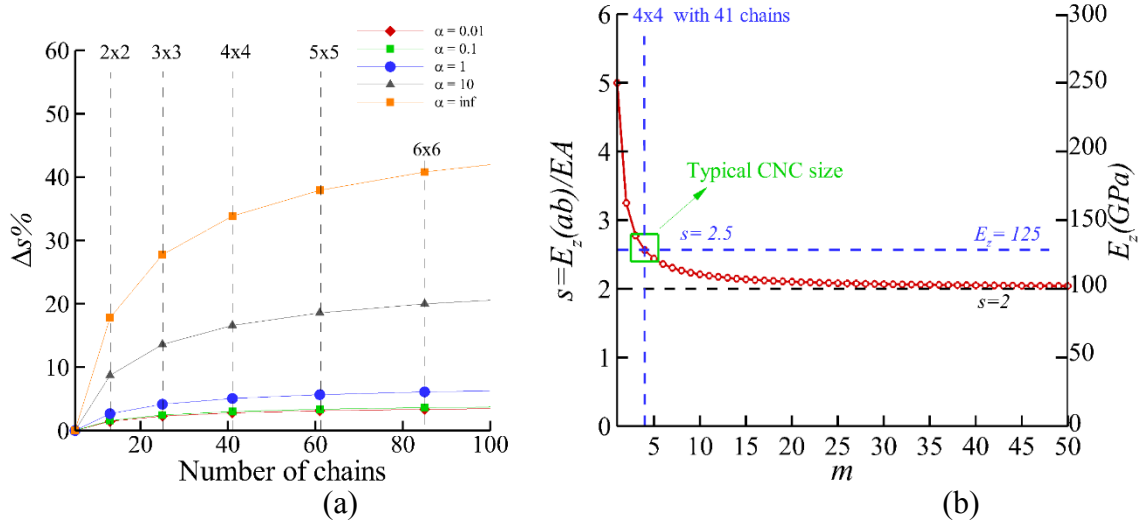


Figure 5.2 (a) Normalized stiffness (ΔS) as function of α and number of chains (b) Variation of s parameter and elastic modulus with respect to size of CNC (m).

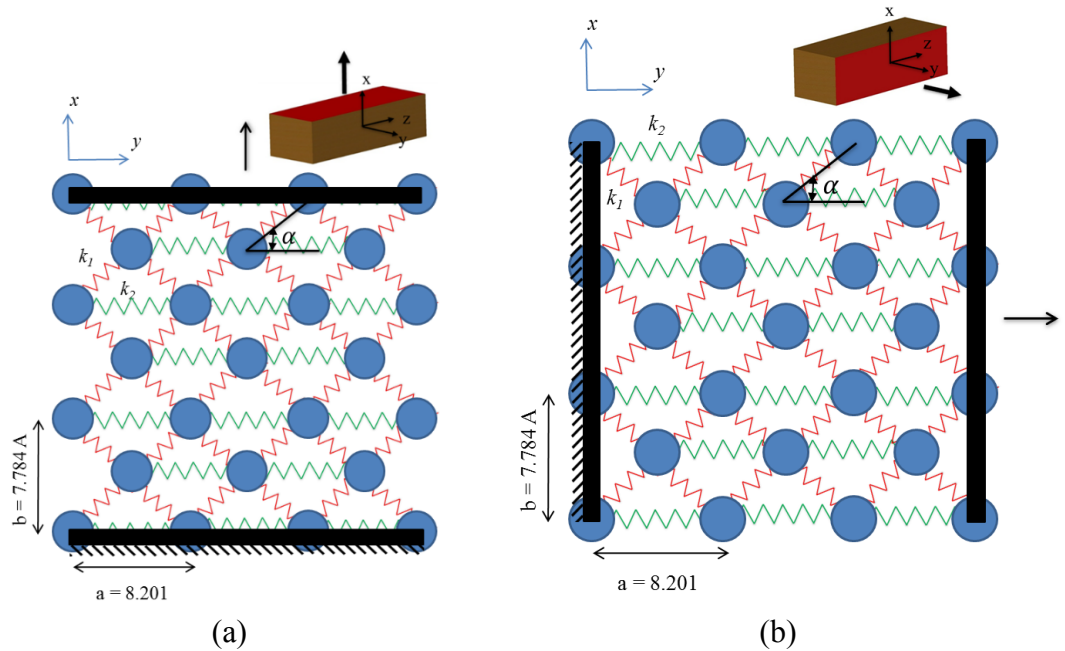


Figure 5.3 2D representation of the 3x3 CNC for tensile loading. Chains are shown with blue circles, stiffness in h-bond direction with green spring and stiffness in VdW direction with red spring. The boundaries for applying and fixing displacement are shown in black rectangle. (a) Applying tensile displacement on top chains in the x direction, VdW direction, while the bottom chains are fixed. (b) Applying tensile displacement on right chains in the y direction, h-bond direction, while the left chains are fixed.

The elastic modulus in the VdW (x -direction) and h -bond (y -direction) directions can also be obtained using a simple spring and mass model as the one shown in the Figure 5.3. The chains in Figure 5.3 are shown with blue circles, the red springs represent inter-chain stiffness and the green springs represent the in-plane stiffness in the h -bond direction, which is the sum of h -bond and VdW stiffness. Here we use the principle of virtual work by balancing the internal and external energy to obtain the elasticity moduli in each direction. The internal energy in the x direction, U , can be written as

$$U = 0.5 \times (K_{1n} L \sin^2 \alpha) \left(\frac{\delta}{2n}\right)^2 \times n \times m \times 4 = 0.5 F \delta \quad (5.10)$$

$$\sigma_x = \frac{F}{WL}, \quad \varepsilon_x = \frac{\delta}{h}, \quad E_x = \frac{\sigma_x}{\varepsilon_x} \quad (5.11)$$

Where F is the external force, δ is the external displacement and $\left(\frac{\delta}{2n}\right)$ is the deformation of each red spring in the x direction. By replacing F from Equation 5.12, $W = m \times a$, $h = n \times b$ into Equation 5.13 the elastic modulus can be expressed as:

$$E_x = (K_{1n} \sin^2 \alpha) \frac{b}{a} \quad (5.14)$$

By using the same approach for tensile test in the y direction, the elastic modulus in the y direction can be obtained as follows

$$U = 0.5 \times (K_{1n} L \cos^2 \alpha) \left(\frac{\delta}{2m}\right)^2 \times n \times m \times 4 + 0.5 \times (K_{2n} L) \left(\frac{\delta}{n}\right)^2 \times [n \times (m+1) + (n-1) \times m] = 0.5 F \delta \quad (5.15)$$

$$\sigma_y = \frac{F}{hL}, \quad \varepsilon_y = \frac{\delta}{W}, \quad E_y = \frac{\sigma_y}{\varepsilon_y} \quad (5.16)$$

In addition to the red springs, k_1 , green springs, k_2 , also contribute to the internal energy, which is shown as the second term in Equation 5.17. By replacing F from Equation 5.18,

$W = m \times a$, $h = n \times b$ into Equation 5.19 the elastic modulus in the y direction can be expressed as

$$E_y = (k_{1n} \cos^2 \alpha) \frac{a}{b} + \left[\frac{m+1}{m} + \frac{n-1}{n} \right] k_{2n} \frac{a}{b} \quad (5.20)$$

5.2 Shear Stiffness

The effect of bonded and non-bonded interactions under shear conditions could also be described by a simple analytic model. Figure 5.4 depicts a simple representation of CNC with the inter-plane and in-plane springs, shown in red and green color respectively. Three simple shear tests are considered: (1) shear on the yz -plane and parallel to y -direction called $shear_{xy}$, Figure 5.4a (2) shear on the yz -plane and parallel to z -direction called $shear_{xz}$, Figure 5.4b, and (3) shear on the xz -plane and parallel to z -direction called $shear_{yz}$ (Figure 5.4c). A model for in plane shear stiffness, $shear_{xy}$, is shown in Figure 5.4a. For these cases, the force-displacement relationship can be obtained using energy approach by equating internal and external energy as shown below.

$$U = 0.5 \times (k_{1n} L \cos^2 \alpha) \left(\frac{\delta}{2n} \right)^2 \times n \times m \times 4 = 0.5 F \delta \quad (5.21)$$

$$\tau_x = \frac{F}{WL}, \quad \gamma_x = \frac{\delta}{h}, \quad G_x = \frac{\tau_x}{\gamma_x} \quad (5.22)$$

Where U is the internal energy, F is the external force, δ is the external displacement and $\left(\frac{\delta}{2n} \right)$ is the deformation of each red spring in the x direction. By replacing F from Equation

5.23 and substituting $W = m \times a$, $h = n \times b$ into Equation 5.24 the elastic shear modulus becomes:

$$G_{xy} = (k_{1n} \cos^2 \alpha) \frac{b}{a} \quad (5.25)$$

For the second case, $shear_{xz}$, this relationship is defined based on k_1 which is the stiffness per length for inter-plane VdW forces and L , which is the length of the 3x3 crystal.

$$U = 0.5 \times (k_{1t} L) \left(\frac{\delta}{2m} \right)^2 \times n \times m \times 4 = 0.5 F \delta \quad (5.26)$$

In Equation 5.27 $\left(\frac{\delta}{2m} \right)$ is the displacement of each spring and $n \times m \times 4$ are the total number of springs. While for the $shear_{xz}$ case only inter-layer VdW forces are involved in shear, both inter-plane and in-plane stiffness contribute to shear for the $shear_{yz}$ case. Finally, for the third case, $shear_{yz}$, the force-displacement relationship can be obtained as follow:

$$U = 0.5 \times (k_{1t} L) \left(\frac{\delta}{2n} \right)^2 \times n \times m \times 4 + 0.5 \times (k_{2t} L) \left(\frac{\delta}{n} \right)^2 \times [n \times (m+1) + (n-1) \times m] = 0.5 F \delta \quad (5.28)$$

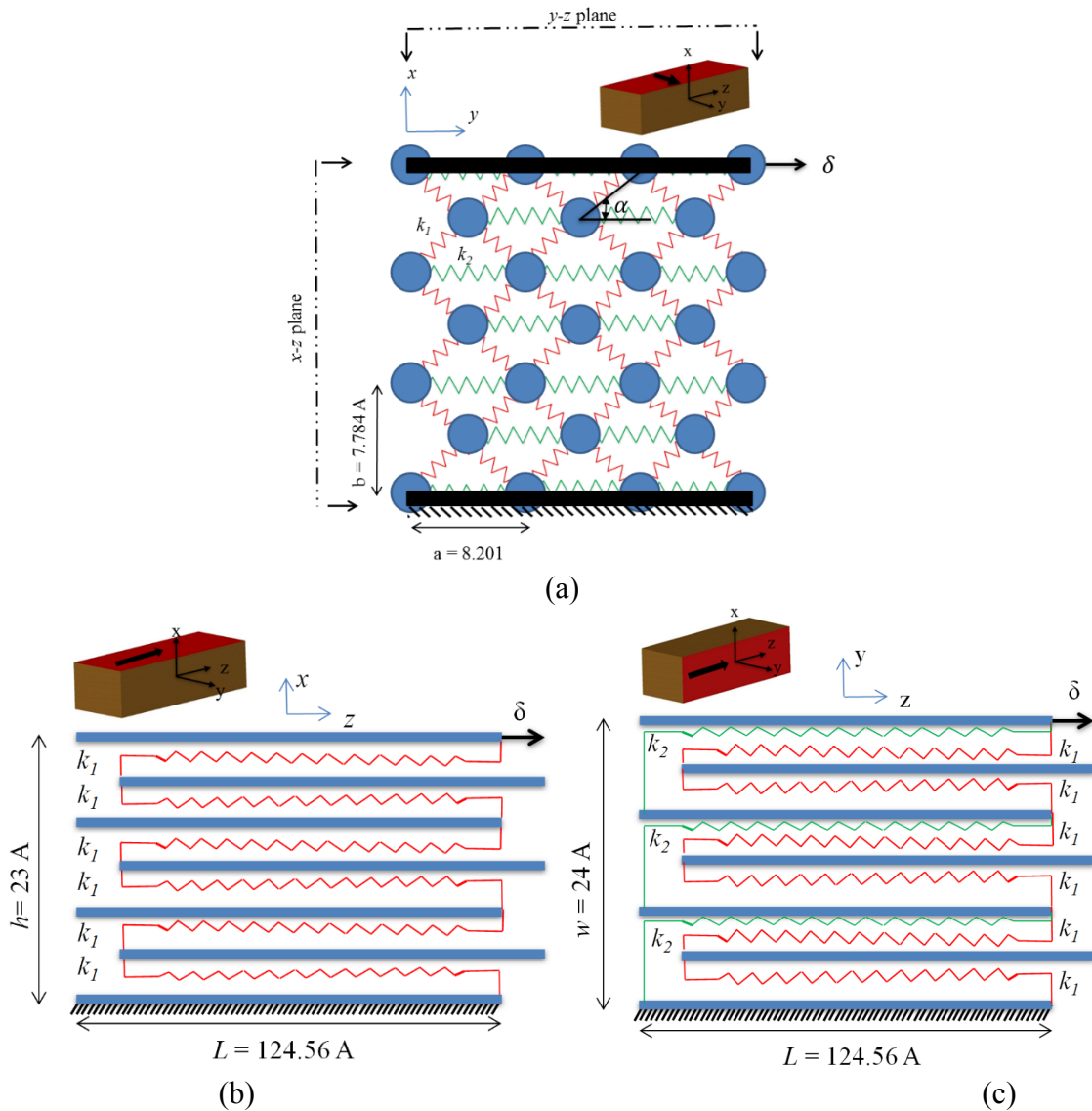


Figure 5.4 Simplified representation of the cellulose crystal to evaluate the elastic shear behavior: (a) Each cellulose chain is shown with blue circle, the inter-plane stiffness is represented by red springs and the in-plane stiffness by green springs in 3x3 crystal (b) shear_{xz} model with red spring representing the inter-plane VdW forces (c) Shear_{yz} model where red springs represent inter-plane stiffness and green springs show the in-plane stiffness.

Where k_1 and k_2 are the inter-plane and in-plane stiffness per length respectively. The shear modulus of CNC can also be obtained from these analyses as follow and using Equation 5.29 and Equation 5.30:

$$G_{xz} = \frac{Fh}{Lw\delta} = \frac{k_{1t}b}{a} \quad (5.31)$$

$$G_{yz} = \frac{Fw}{Lh\delta} = \left[k_{1t} + \left(\frac{m+1}{m} + \frac{n-1}{n} \right) k_{2t} \right] \frac{a}{b} \quad (5.32)$$

5.3 Bending Stiffness

We also developed a simple analytical model for a CNC under bending assuming that the bending stiffness is only governed by the stiffness of the individual chains and ignoring the non-bonded interactions to show the contribution of chain stiffness on bending stiffness. Figure 5.5 represents the cross section of a 3×3 crystalline cellulose under bending replacing chains with blue circles. Although the cross section of CNC after equilibrium is not a perfect rectangular shape, we assume a rectangular shape for simplicity. Figure 5.5b shows the applied bending moment, M , rotation angle, θ , height of the cross section, h , and resulting tension, compression forces applied to the chains.

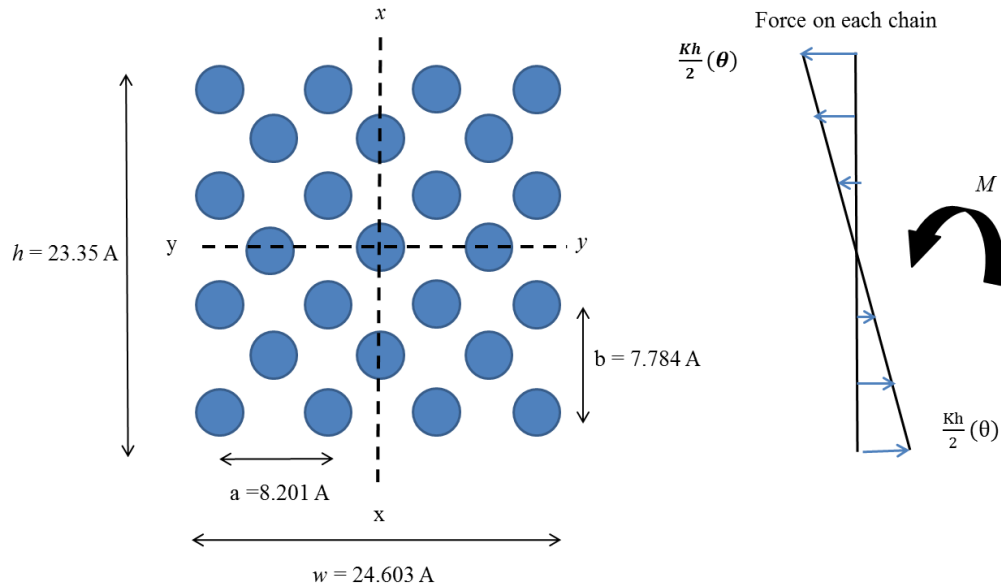


Figure 5.5 Each cellulose chain is shown with blue circle in 3x3 crystal. Tension, compression forces induced at cross section due to bending of crystal.

The relationship between moment and bending radius per length at any cross section can be expressed as

$$M = 4\left(\frac{kh^2}{2}\theta\right) + 3\left(\frac{2kh^2}{9}\theta\right) + 4\left(\frac{kh^2}{18}\theta\right), \quad k = \frac{EA}{L} \quad (5.33)$$

$$M = \frac{26h^2EA}{9}\left(\frac{\theta}{L}\right) \quad (5.34)$$

Where θ is bending angle, EA is stiffness of each chain, h is the height of the cross section and L is the length of each chain. By replacing EA from 5.35, and considering $W = m \times a$, $h = n \times b$ and $m = n = 3$, the moment-curvature relationship from Equation 5.36 can be rewritten as:

$$M = \frac{26h^2}{9} \left(\frac{E_z wh}{N} \right) \left(\frac{\theta}{L} \right) = \frac{26}{25 \times 9} E_z wh^3 \left(\frac{\theta}{L} \right) \quad (5.37)$$

Equation 5.38 can be further reduced considering the second moment of inertia of solids,

$$I = \frac{1}{12} wh^3, \text{ and curvature } \kappa = \frac{\theta}{L}$$

$$M \equiv f \cdot E_z I \kappa \quad (5.39)$$

where for this particular case $f = 4/3$. This general expression is similar to that obtained for isotropic solids (e.g., $M = EI\kappa$) expect that $f = 1$. If we follow the same procedure for a crystal size of $m \times n$, the general relationship is obtained as follow:

$$M = \left[\sum_{i=0}^{\frac{n}{2}} 0.5(m+1) \left(\frac{n-2i}{n} \right)^2 + \sum_{i=1}^{\frac{(n+1)}{2}} 0.5m \left(\frac{n-2i+1}{n} \right)^2 \right] EA h^2 \left(\frac{\theta}{L} \right) \quad (5.40)$$

By replacing EA from Equation 5.41 and the second moment of inertia of solids, $I = \frac{1}{12} wh^3$, in Equation 5.42 the following expression is obtained.

$$M = 12 \times \left[\sum_{i=0}^{\frac{n}{2}} 0.5(m+1) \left(\frac{n-2i}{n} \right)^2 + \sum_{i=1}^{\frac{(n+1)}{2}} 0.5m \left(\frac{n-2i+1}{n} \right)^2 \right] \frac{E_z I}{(m+1)(n+1) + mn} \kappa \quad (5.43)$$

Leading to an expression similar to Equation 5.44, except that the new coefficient f can be obtained by dividing Equation 5.45 by EIk . The values for coefficient for a square shape ($n = m$) with different values of m are plotted in Figure 5.6. The coefficient value merges to 1, similar to solids, as the dimension increases and has the highest value of 2.4 for $m=n=1$. The value of f for typical CNC size is 1.2-1.4 with average of 1.28 for $m=4$ with 41 chains.

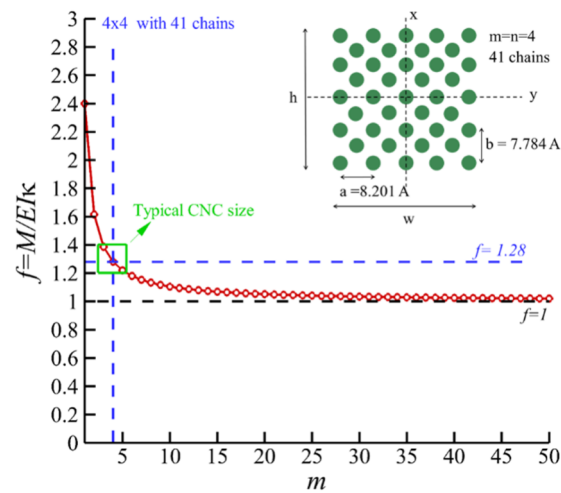


Figure 5.6 Bending stiffness multiplier, f , for different size of CNC is plotted. The value of f for typical CNC size is 1.2-1.4 with average of 1.28 for $m=4$ with 41 chains.

CHAPTER 6. THE EFFECT OF BONDED AND NON-BONDED INTERACTIONS ON THE MECHANICAL PROPERTIES

(A version of this chapter is published <https://doi.org/10.1016/j.jmps.2017.11.006>)

6.1 Methodology

The proposed continuum-based structural model (denoted as CM), along with the MD simulations, is employed to study the effect of bonded and non-bonded interactions of CNCs in tension, shear, bending and torsion. The fact that bonded and non-bonded interactions are separated in the continuum model allows us to understand the contribution of each term on the overall response by direct comparisons with MD at 1 K. Although both MD at 1 K and MM are essentially molecular statics, overcoming potential barriers under different loading conditions is only possible with MD simulations. Using MD simulations at 1 K has also been used by many authors before (Cao and Chen, 2006; Chang and Hou, 2006; Chang, 2013) to eliminate the effect of thermal fluctuations on the mechanical properties. In addition, DFT calculations shows that temperature (0-500 K) has little effect on the mechanical properties of the CNC (Zavattieri, 2014). Since the mechanical tests in MD are performed after minimization and equilibration, the equilibrated structure of CNC has been used for obtaining the geometrical properties of the continuum model such as the center of mass for each chain and average position of donors and acceptors. In all these cases, MD analysis is performed on a 3×3 square CNC with DP = 24 using ReaxFF with time step 0.5 fs. First, the system is minimized using the hftn algorithm and then

equilibrated for 1 ns while the temperature is controlled by the Nosé-Hoover thermostat at 0 Kelvin in a NVT ensemble. After equilibration, deformation at different rates associated to tension, shear, bending or torsion is applied on the boundaries as schematized in Figure 6.1 for each case respectively. In our CM analysis, a beam element represents two glucose molecules (two rings); however, our mesh sensitivity analysis (Appendix A4) shows that larger element size can also be employed.

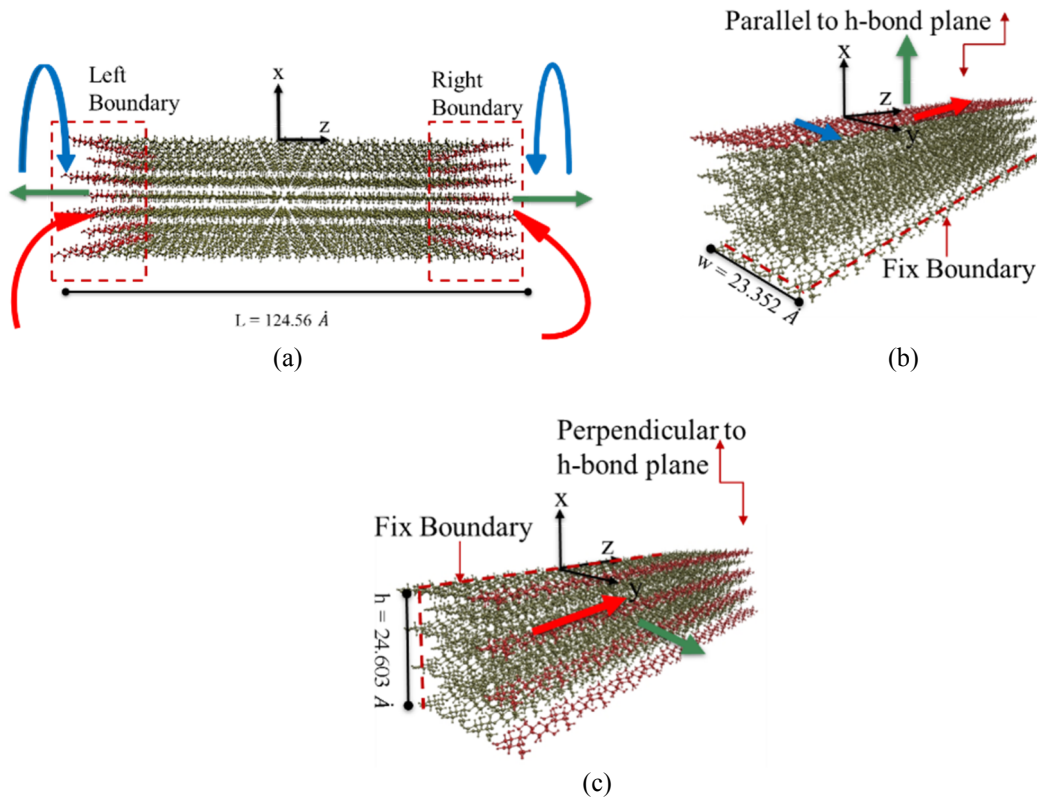


Figure 6.1 Details of the MD model and boundary conditions for a 3×3 square CNC. (a) Tension, bending and torsion displacements are applied on right and left boundaries. The green, red and blue arrows show the direction of tensile, bending and torsion displacement. (b) Displacement for $shear_{xz}$ is applied parallel to h-bond plane on top surface, red arrow, while the opposite surface is kept fixed. Blue arrow shows the displacement direction for $shear_{xy}$ and the direction of tension displacement for $tension_{xx}$ is shown with green arrow. (c) Displacement for $shear_{yz}$ is applied perpendicular to h-bond plane on right surface, red arrow, while the opposite surface is kept fixed. Green arrow shows the displacement direction for tension test in y -direction.

6.2 Tensile Tests

First, three simple tension tests in x , y and z directions are performed where dominant stiffness factor in the x direction is the presence of VdW forces, K_{1n} , in the y direction are VdW forces and h -bonds, K_{2n} , and in the z direction is mainly governed by the covalent

bond (EA). For each test, the displacement is applied at the corresponding atoms lying on the selected boundaries. For tension in the z direction, the displacement is applied on the two cellulose rings of each chain on right side of the crystal (right boundary) while the left boundary is kept fixed as shown in Figure 6.1a. For tension in the x and y direction, the atoms lying on the top and right boundaries shown in Figure 6.1b and Figure 6.1c, respectively, are displaced while their opposite surface are kept fixed. We employ different strain rates (i.e., 5.0×10^{-5} and 2.0×10^{-4} , 1.0×10^{-4} ps $^{-1}$) to ensure that quasi-static equilibrium is satisfied. Finally, the total tensile forces in x , y and z directions are obtained by summation of forces in the x , y and z directions (f_x , f_y and f_z , respectively) over corresponding boundary atoms as shown in Figure 6.1. We consider that the equilibrium condition is satisfied if the difference between the absolute value of the total force on the moving and the fixed boundaries is less or equal than 0.1%.

The stress-strain curves for the tension tests in x , y and z directions are shown in Figure 6.2a, Figure 6.2b and Figure 6.2c, respectively. The elastic modulus for tension in the x direction, E_x , predicted by MD is 6.0-7.0 GPa while results from our model varies from 3.2-5.35 GPa as shown in Fig. 7a. The relationship between E_x and our model parameters are as follow (see analytical derivation in Chapter 3)

$$E_x = (K_{1n} \sin^2 \alpha) \frac{b}{a} \quad (6.1)$$

Where α , b , a are geometric parameters shown in Figure 5.3 and K_{1n} is the inter-plane normal stiffness explained above in section 3.2. For a perfect crystalline shape the values for a , b and α are 0.8201 nm, 0.7784 nm and 43.5° respectively which suggests a range of 2.5-4.5 GPa for E_x . This lower values of E_x with respect to the CM results may be due to the fact that after equilibrium the geometrical values, α , b , a , are different. For example the average value of E_x from Equation 6.2 is 3.5 GPa while our CM model predicts 4.22 GPa due to the change in geometric parameters ($a= 0.8$ nm, $b = 0.85$ nm and $\alpha = 50^\circ$) after equilibration. Comparison of the results with MD indicates 33% of error for average value of E_x in our CM model. One reason for underestimating the value of K_{1n} is the absence of any h -bond force in the x direction, while in MD there are few weak h -bond contributing to E_x as shown in Figure 6.2. In contrast, considering the contribution of the h -bond stiffness in the x direction (which is equivalent to approximately 3 nN/nm²) to the K_{1n} , the average value from the CM model for E_x becomes 6.0 GPa which is more consistent with the MD results (6.0-7.0 GPa). Consequently, the range of E_x according to Equation 6.3 becomes to 3.5-6.5 GPa.

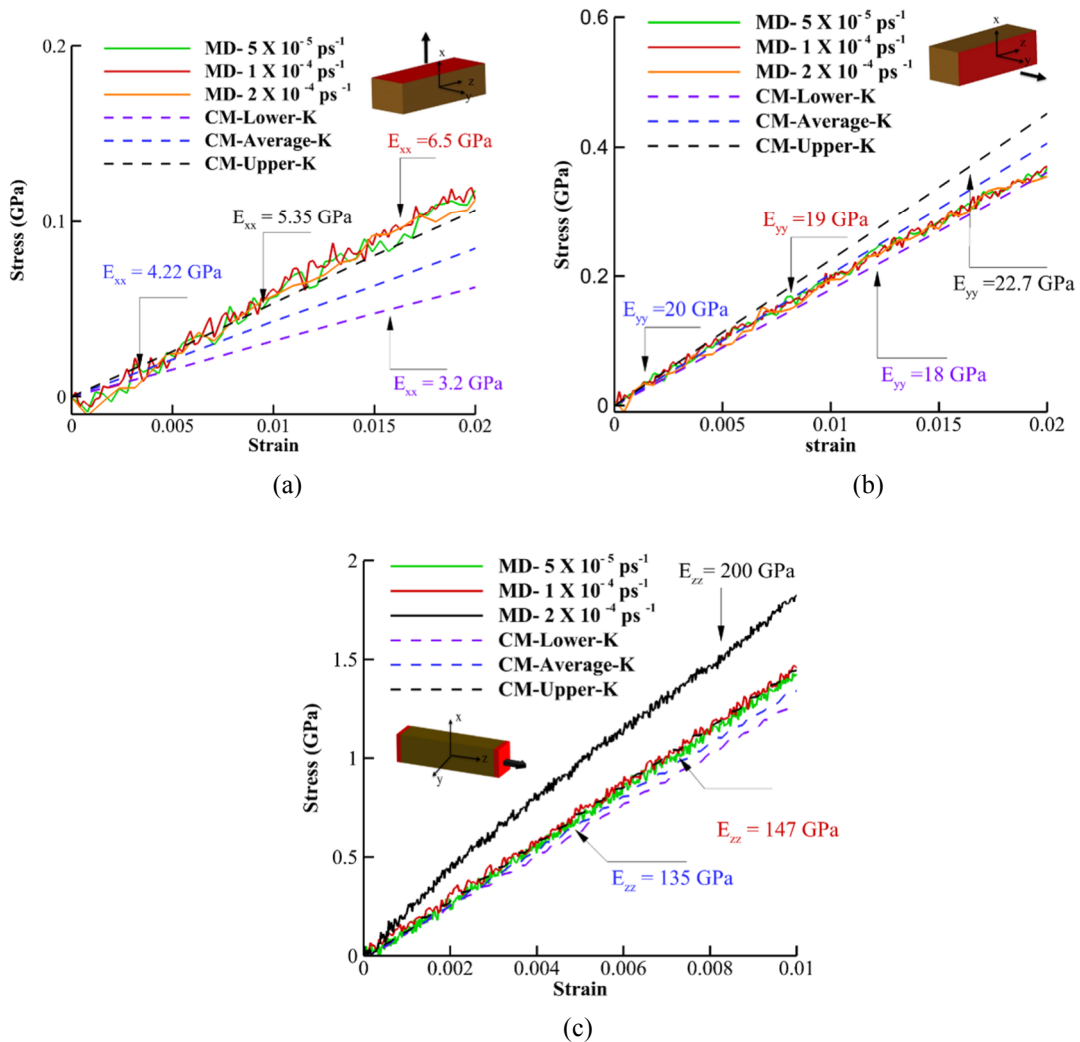


Figure 6.2 Stress-strain curves for tension test. Comparing Continuum Model (CM) with molecular dynamics (MD) with different rates. (a) x direction (b) y direction and (c) z direction

The stress-strain curves to calculate for E_y are shown in Figure 6.2b. The values from CM vary from 18 to 22.7 GPa which is consistent with the 17-22 GPa obtained by MD. The analytical solution for E_y based on our model parameters and the simple spring and mass model presented in chapter 5 is

$$E_y = [(K_{1n} \cos^2 \alpha) + (\frac{m+1}{m} + \frac{n-1}{n})K_{2n}] \frac{a}{b} \quad (6.4)$$

Where α , b , a are the geometric parameters shown in Figure 5.3b. K_{1n} and K_{2n} are the inter-plane and in-plane normal stiffness discussed in section 3.2. The parameters m and n are the number of repeated unit cell in the CNC structure (e.g. here m and n are both equal to 3). For a perfect CNC structure, Equation 6.2 predicts $E_y = 26\text{-}36$ GPa, which indicates that the potential imperfection introduced by equilibration could reduce elastic modulus in the y direction by 30%. In addition, from Equation 6.2 and knowing the value for h -bond stiffness, we infer that the contribution of h -bond in E_y is around 50% and the other half is provided by VdW forces.

For the stiffness in the z direction, Figure 6.2c, we observed strain rate dependent elasticity for 2.0×10^{-4} ps⁻¹ strain rate and higher where equilibrium is no longer satisfied. Due to the fact that bonded and non-bonded interactions are separated in the continuum model, their contribution in the total stiffness can readily be studied by turning on/off non-bonded elements. Interestingly, the same stress-strain response is obtained when we turn off the non-bonded elements, indicating that the stiffness is mainly driven by the covalent bond and intra-chain h -bonds. There is a negligible difference between continuum and MD curves ($\sim 8\%$ in the elastic modulus). A simple analytical model for CNC with a h -bonding network A (Nishiyama et al., 2002), is presented in Appendix A-1 to evaluate the effect of

inter-chain h -bond on the total stiffness of CNCs. The results indicate that the contribution of the inter-chain h -bond in the axial stiffness for a 3×3 CNC is approximately 3%, and less than 5% contribution for a large $m \times n$ crystal. Therefore, we conclude the remaining 5% of difference in elasticity is coming from the estimation of chain stiffness. The analytical expression for E_z based on the simple model presented in Appendix A1 is given by

$$E_z = \frac{[(m+1)(n+1) + mn]EA}{(ma \times nb)} \quad (6.5)$$

Considering $m=n=3$ then E_z as 126-142 GPa which has a good agreement with the CM, 123-147 GPa, and MD, 141-153 GPa, results presented in Figure 6.2c. In addition, from Equation 6.6, and assuming that chain stiffness, EA , is constant for different values of m and n ; the variation of elastic modulus, E_z , with respect to the size of CNC can be plotted as shown in Figure 5.2b. The values of E_z varies from 250 GPa to 100 GPa $m=1$ and large value of m respectively. The typical size associated with a typical CNC size is indicated in Figure 5.2b with green rectangle suggesting a range of 115-135 GPa for E_z .

6.3 Shear Tests

To further study the mechanical behavior of the CNC, we load it in shear along three different directions and at different strain rates (i.e., 2.0×10^{-4} , 5×10^{-4} and $2.0 \times$

10^{-3} ps^{-1}). For a simple shear test, the displacement is applied on one surface while the opposite surface is kept fixed while equilibrium condition is satisfied. The total shear stress is then obtained as the summation of all the corresponding individual forces on the surface of interest divided by its area. In the $shear_{xy}$ test, the displacement is applied on top surface in the y direction and parallel to h -bond plane as shown with blue arrow in Figure 6.1. The stress-strain curves of CM and MD simulations for $shear_{xy}$ are shown in Figure 6.3. The value for the shear modulus from MD simulation is $G_{xy} = 1.9\text{-}2.9 \text{ GPa}$, while the CM provides a range of $G_{xy} = 1.2\text{-}2.2 \text{ GPa}$.

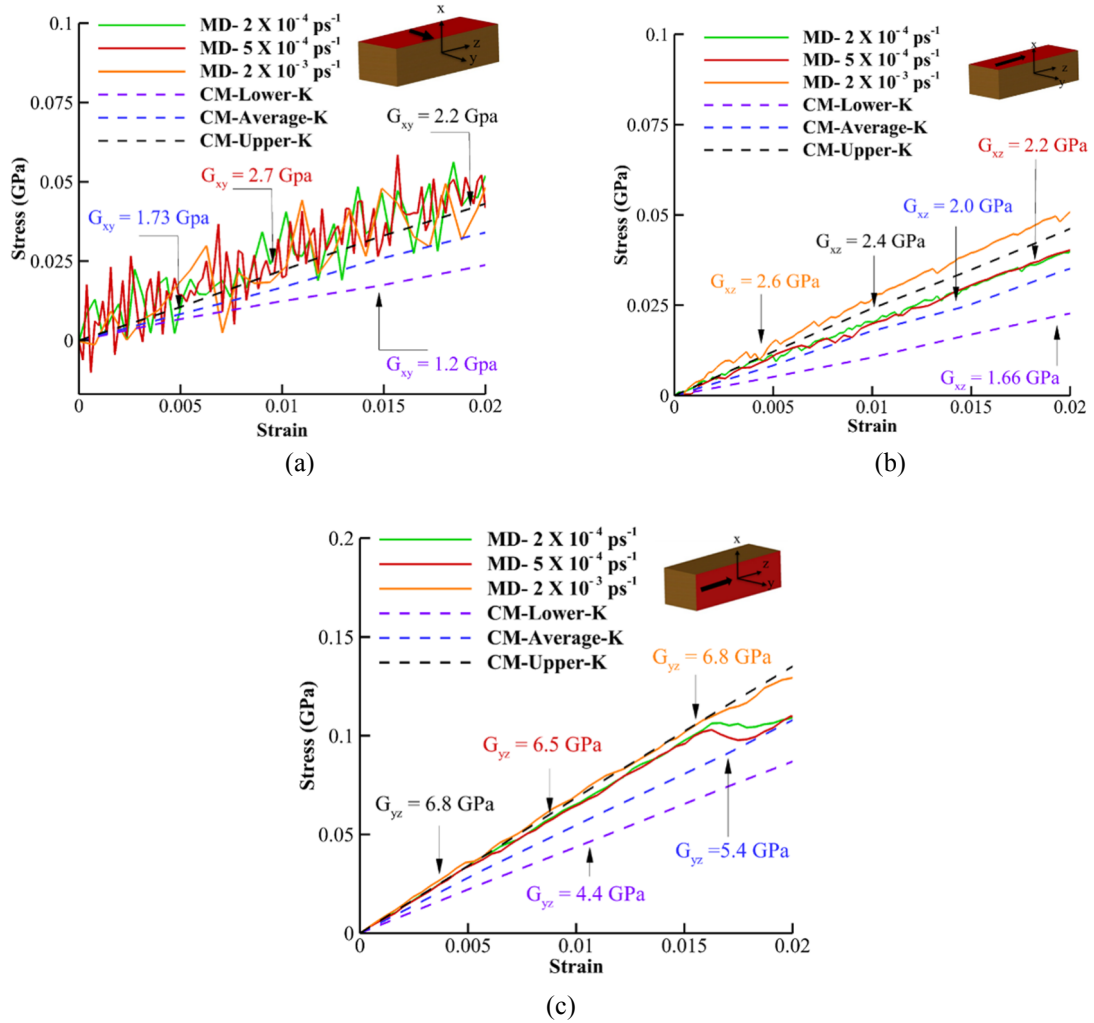


Figure 6.3 Stress-strain curves for shear tests from MD with different rates and CM with upper and lower bound obtained from upper and lower bound of stiffness respectively. (a) Stress-strain curves for $shear_{xy}$ (b) $shear_{xz}$ and (c) $shear_{yz}$

To understand what parameters in our CM model affects the G_{xy} , a simple analytical solution from a spring-mass model for $shear_{xy}$ is employed (Appendix A-2) as follow

$$G_{xy} = (K_{1n} \cos^2 \alpha) \frac{b}{a} \quad (6.7)$$

Similar to the case with tension in the x direction, K_{1n} is responsible for the elastic modulus and should be corrected by adding h -bond stiffness in the x direction. After adding h -bond stiffness, CM new range of values is 1.8-3.2 GPa, which is consistent with MD results.

From Equation 6.8 the theoretical value of G_{xy} for a perfect CNC structure is 3.75-5.75 GPa with a , b and α equal to 0.8201 nm, 0.7784 nm and 43.5° respectively. Further analysis shows that 30% of G_{xy} is provided by the h -bond stiffness and 70% by the VdW interaction. For G_{xz} test, displacement is applied on top surface and in the z direction, parallel to h -bond plane as shown with red arrow in Figure 6.1b. The stress-strain curves for G_{xz} obtained from the MD and CM simulations are shown in Figure 6.3b, which indicate that the corresponding shear modulus, G_{xz} , is 2.0-2.6 GPa from the MD simulation, while the CM simulations exhibit a range of 1.6-2.4 GPa. A simple spring-mass model helps elucidate the shear mechanisms in CNC (chapter 5). Accordingly,

$$G_{xz} = \frac{K_{1t}b}{a} \quad (6.9)$$

This analytical expression yields G_{xz} 1.3-1.9 GPa, which is close to CM and MD results. This indicates that G_{xz} is not too much affected by the geometrical change due to the equilibration. The third shear test is G_{yz} , where the displacement is applied on the right surface in the z direction, perpendicular to h -bond planes, as shown with red arrow in Figure 6.1c. The stress-strain curves for G_{yz} are plotted in Figure 6.3c for MD and CM. The value for shear modulus, G_{yz} , from MD is 6.5-6.8 GPa, while CM predicts a range of

$G_{yz} = 4.4-6.8$ GPa. The analytical model for G_{yz} gives us the relationship between G_{yz} and our model parameters as follow (chapter 5):

$$G_{yz} = [K_{1t} + (\frac{m+1}{m} + \frac{n-1}{n})K_{2t}] \frac{a}{b} \quad (6.10)$$

Where b , a are geometric parameters shown in Figure 5.4. K_{1t} and K_{2t} are the inter-plane and in-plane shear stiffness explained in chapter 4. From Equation 6.11 the shear modulus, G_{yz} , for the perfect CNC structure is predicted as 5.6-8.4 GPa, which indicates that the change in the CNC structure during equilibration has little effect on the G_{yz} .

6.4 Bending and Torsion Tests

Two bending tests are also performed to understand the mechanical performance of CNC under bending in the x and y direction. For both tests, the moment is applied at the end of the CNC by applying rotational displacements at different rates (i.e., 5.0×10^{-4} , 2.5×10^{-3} and 5.0×10^{-3} rad/ps) on the first two rings of each chain on the right and left hand side of the crystal (see red arrows in Figure 6.1a). In such a way, the boundary atoms move similar to boundaries in a pure bending test. For pure bending around the y direction, parallel to the h -bond plane, the bending moment is calculated as

$$M_y = \sum_1^{nbc} (z \times f_x - x \times f_z) \quad (6.12)$$

Where M_y is the bending moment in y direction, nb is the number of atoms at boundary, z and x are the distance of each boundary atoms from the z and x axes, respectively (the origin of the system of coordinates is located at the centroid of the CNC). Finally f_x and f_z are total forces on each boundary atoms in x and z direction, respectively. To understand the effect of covalent bond on the bending stiffness, we analyze the CM model with and without non-bonded stiffness. Moment-curvature plots for pure bending around y -axis obtained from MD and CM simulations are shown Fig. 9a. The bending stiffness around the y axis calculated with MD is $EI_{yy} = 550\text{-}800 \text{ nN}\cdot\text{nm}^2/\text{rad}$ and from CM is $EI_{yy} = 742 \text{ nN}\cdot\text{nm}^2/\text{rad}$ on average with upper bound and lower bound of 710 and 774 $\text{nN}\cdot\text{nm}^2/\text{rad}$ respectively. The parameters involved in our model for EI_{yy} are EA (chain stiffness) and K_{1t} (inter-plane shear stiffness, which is also the main parameter for G_{xz}). As expected, during bending deformation around the y axis, the chains on top and bottom of y axis experience compression and tension, respectively. As such, the high axial stiffness of the individual cellulose chains significantly contributes to overall bending stiffness. From this perspective, a simple spring-mass model can be developed based on the single cellulose chain stiffness, EA , (see Appendix A3):

$$M = \frac{26h^2 EA}{9} \left(\frac{\theta}{L} \right) \quad (6.13)$$

Where θ is the bending angle, EA is stiffness of each chain, h is the height of the cross section and L is the length of each chain. By replacing the values for EA and h in Equation 6.14 , the bending stiffness, $EI_{yy} = 487 \text{ nN}\cdot\text{nm}^2/\text{rad}$. This value is lower than the value $572 \text{ nN}\cdot\text{nm}^2/\text{rad}$, pink dash line in Figure 6.4a, obtained from CM with no non-bonded stiffness. We surmise that this difference is coming from considering a perfect CNC structure (i.e., with exact dimensions as previously reported in the literature), while the CM model employs the position of the chain based on the ones predicted by MD after equilibration. For instance, the value of $h = 2.55 \text{ nm}$ in the CM model is 7% larger than the actual value used in the analytical equation $h = 2.335 \text{ nm}$. If we use $h = 2.55 \text{ nm}$ in the analytical equation, then a value of $EI_{yy} = 582 \text{ nN}\cdot\text{nm}^2/\text{rad}$, which is similar to those obtained with CM. Comparing the results for CM with average value of non-bonded stiffness and the case with no non-bonded stiffness , we conclude that 23% of the value for average EI_{yy} in the CM model is due to non-bonded stiffness, K_{1t} , and 77% from the EA (intra-chain h -bond and covalent bond). In addition, comparing the results from MD with CM-EA (only chains stiffness (EA) contribute with no non-bonded contribution) shows that non-bonded interactions represent less than 20% of the overall value of EI_{yy} . can be further reduced considering the second moment of inertia of solids, $I = \frac{1}{12}wh^3$, and curvature $\kappa = \frac{\theta}{L}$ to

$$M \equiv f \cdot E_z I \kappa \quad (6.15)$$

where for this particular case $f = 4/3$. This general expression is similar to that obtained for isotropic solids (e.g., $M = EI\kappa$) expect that $f = 1$. The values for f for a square shape ($n = m$) with different values of m are plotted in Figure 5.6. The f value merges to 1, similar to solids, as the dimension increases and has the highest value of 2.4 for $m = n = 1$. The value of f for typical CNC size is 1.2-1.4 with average of 1.28 for $m = 4$ with 41 chains.

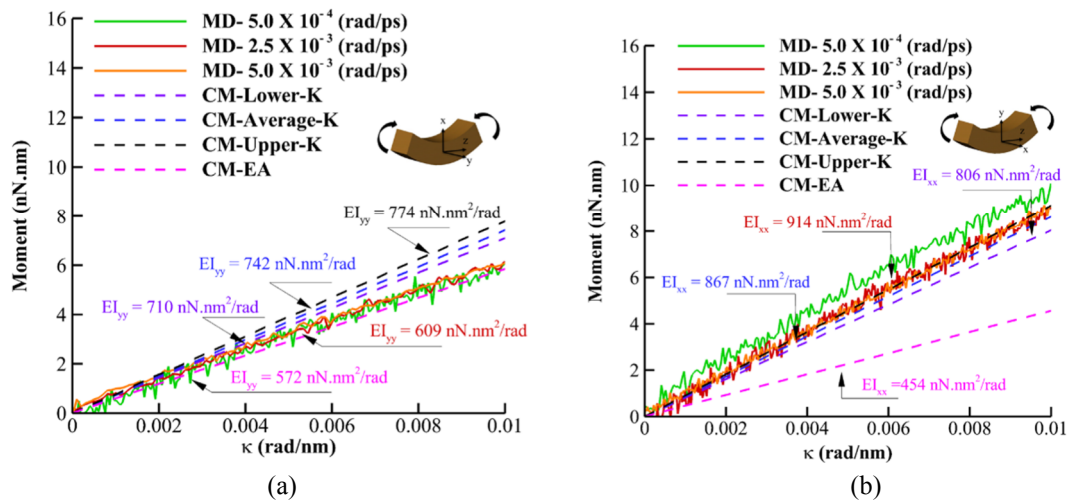


Figure 6.4 Moment-curvature plots for bending of CNC obtained from MD and CM simulations with different rates and different stiffness respectively. (a) pure bending around y-axis, which is parallel to the h-bond plane. (b) Pure bending around x axis which is perpendicular to the h-bond plane.

Similarly, we analyze bending around the x axis, perpendicular to the h -bond plane. In this case, the bending moment is calculated as

$$M_x = \sum_1^{nbc} (z \times f_y - y \times f_z) \quad (6.16)$$

Where M_x is the bending moment in x direction, nbc is the number of atoms at boundary, z and y are the distance of each boundary atoms from z and y axes, respectively (the origin is the centroid of the CNC). Figure 6.4b exhibits the moment-curvature plots for pure bending around the x axis. MD predicts $EI_{xx} = 800\text{-}1000$ nN.nm²/rad, while CM values are $EI_{xx} = 806\text{-}916$ nN.nm²/rad. Equation 6.17 can also be used to estimate EI_{xx} , by changing h to w , when there are no non-bonded interactions involved. In such case, the estimated value for from Eq. 18 is $EI_{xx} = 435$ nN.nm²/rad, which agrees very well with the value reported by CM with non-bonded stiffness (i.e., $EI_{xx} = 454$ nN.nm²/rad). The parameters involved in our model for EI_{xx} are EA and K_{2t} (in-plane shear stiffness which is also the main parameter for G_{yz}). By comparing the results obtained with CM with average stiffness and CM with no stiffness, it can be concluded that 52% contribution to EI_{xx} is provided by EA (coming from intra-chain h-bond and covalent bond) and the rest is from K_{2t} (non-bonded interactions). Also by comparing the CM results with MD, we can conclude that, in the case of EI_{xx} , bonded and non-bonded interactions have equal contribution to bending stiffness as opposed to the EI_{yy} case, where EA is almost the only contribution to the overall bending stiffness.

A final test is to subject a CNC to a torsion loading. In this case the angular displacements are directly applied to the left and right boundaries, as shown with blue arrows in Figure 6.1a, at different rates including (i.e., 1.0×10^{-5} , 1×10^{-4} and 5.0×10^{-4} rad/ps). The torque is then obtained as follows:

$$T = \sum_1^{nbc} (xf_y - yf_x) \quad (6.18)$$

Where T is the torque, nbc is the number of atoms at the boundary, x and y are the distance of each boundary atoms from x and y axis, respectively, with respect to the origin, which is located at the center of mass. f_x and f_y are total forces on each boundary atoms in x and y directions, respectively. The total torque, T , versus twist deformation per unit length, κ , for MD and CM are shown in Figure 6.5a. The estimated value for GJ from MD is 10-50 nN.nm²/rad, while CM suggests negligible torsional stiffness (0-10 nN.nm²/rad). We realized that the only parameter in our CM that has influence on GJ is EI_c (bending stiffness of the chain). However, the value of the torque obtained with the CM model always fluctuate. The main reason for this fluctuation may be the small value of GJ in CNC. In fact, Figure 6.5b clearly shows that the bending stiffness, EI_{yy} , is larger than the torsional stiffness, GJ . The fact that GJ is one order of magnitude smaller than EI_{yy} suggests that CNCs could twist easily even under small loads which could also explain the tendency of CNCs to naturally twist without external loads (Hanley et al., 1997; Lotz and Cheng, 2005; Hadden et al., 2013; Zhao et al., 2013).

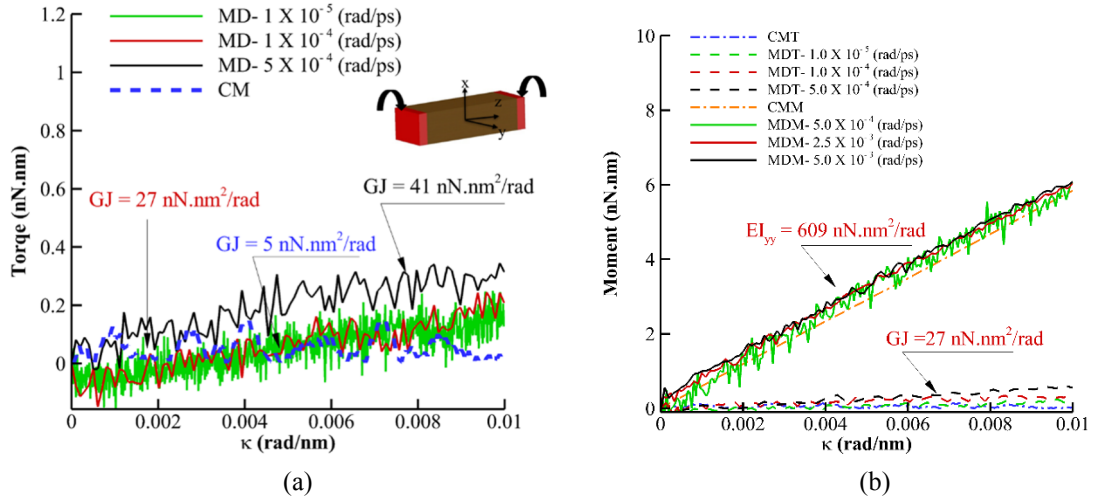


Figure 6.5 (a) Torque-twist angle per length curves for torsion test with different torsion frequencies for MD and continuum. (b) Same results in bending scale.

6.5 Comparing MD, CM and Homogenization Models

Table 6.1 summarizes the analytical expressions presented in the Appendix section for the elastic properties of CNC based on the spring constants, EA , K_{1t} , K_{1n} , K_{2t} , K_{2n} and geometric properties. The table also includes the value obtained for the perfect crystal, and the comparison with the MD results. While the differences with respect to the MD results are mainly due to structural change after MD equilibration, these results are very encouraging. This demonstrate that fundamental elements of conventional solid mechanics can be employed to explain the contributions of the different bond types on the overall stiffness of CNCs. In order to illustrate whether the details of the chains and non-bonded interaction are needed, we model a CNC under bending employing FEM and treating the CNC as a homogeneous and orthotropic solid. To increase accuracy, we use the elastic

properties obtained from MD simulations (taken from the fourth column in Table 6.1). This homogenized model (denoted as FEM) is different from the CM model in the sense that it assumes the CNC is only a homogeneous orthotropic solid with no structure inside.

Table 6.1 Elastic properties of CNC based on spring-mass model.

| Elastic property | Formulation | Values for a perfect CNC (GPa) | Values from MD (GPa) |
|------------------|--|--------------------------------|----------------------|
| E_x | $(K_{1n} \sin^2 \alpha) \frac{b}{a}$ | 5 ± 1.5 | 6.5 |
| E_y | $[(K_{1n} \cos^2 \alpha) + (\frac{m+1}{m} + \frac{n-1}{n})K_{2n}] \frac{a}{b}$ | 31 ± 5 | 19 |
| E_z | $\frac{[(m+1)(n+1) + mn]EA}{(ma \times nb)}$ | 134 ± 8 | 147 |
| G_{xy} | $(K_{1n} \cos^2 \alpha) \frac{b}{a}$ | 4.75 ± 1 | 2.7 |
| G_{xz} | $K_{1t} \frac{b}{a}$ | 1.6 ± 0.3 | 2.0 |
| G_{yz} | $[K_{1t} + (\frac{m+1}{m} + \frac{n-1}{n})K_{2t}] \frac{a}{b}$ | 7 ± 1.4 | 6.5 |

Figure 6.6 compares the values EI_{xx} and EI_{yy} obtained from MD, CM with average stiffness and FEM. By comparing the FEM and MD, as it can be observed, the FEM model clearly underestimates the bending stiffness in both directions. Although the value for EI_{yy} predicted by FEM, 434 nN.nm²/rad, is comparable with MD, 609 nN.nm²/rad, the

results for EI_{xx} , $333 \text{ nN}\cdot\text{nm}^2/\text{rad}$, is very different from value obtained from MD simulation ($914 \text{ nN}\cdot\text{nm}^2/\text{rad}$). In fact, the value of EI_{xx} obtained with the FEM results agrees with the CM model for the case without non-bonded stiffness (i.e, $K_{2l} = 0$), $EI_{xx} = 454 \text{ nN}\cdot\text{nm}^2/\text{rad}$, as seen as a pink dash line in Fig. 10b. In summary, although FEM can model the contribution of EA (chain stiffness) to the EI_{xx} and EI_{yy} through E_z in an orthotropic material, it fails to properly capture the contribution of non-bonded interaction.

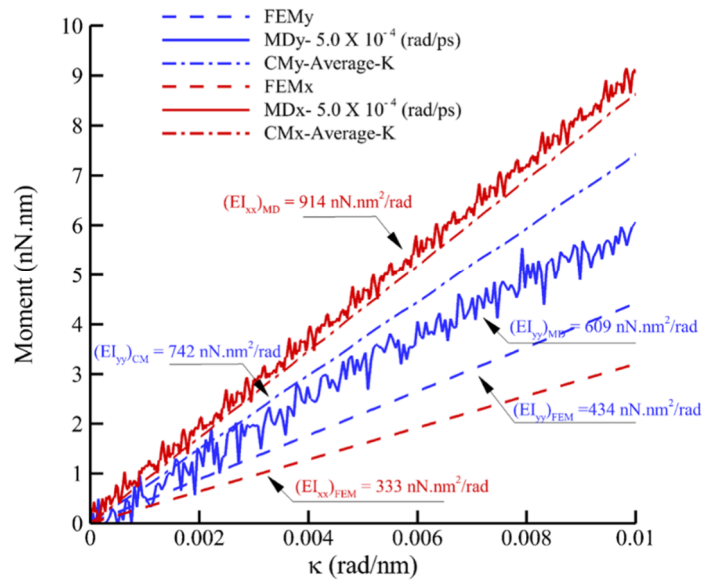


Figure 6.6 Moment-curvature plots for bending of CNC around x and y axis acquired from CM, MD and FEM simulations. The solid curves show MD results, dashed lines are FEM results and dashed-dot lines present CM results. The lines with blue and red color represent bending around y and x axis respectively.

6.6 Summary and conclusion

In this dissertation, a continuum-based structural model was developed to investigate the role of bonded and non-bonded interactions on the mechanical properties of crystalline cellulose for small strains. In particular, bonded and non-bonded interactions were uncoupled in our continuum model and substituted by an equivalent continuum element. Ancillary atomistic simulations were employed for feeding the continuum model parameters and also for verification purposes. We performed a variety of mechanical tests including tension, shear, bending and torsion to understand the deformation mechanism and contribution of each type of bonding on the elastic behavior of CNCs. For most of the cases, analytical expressions for perfect CNC structure were proposed to understand how imperfection in the structure after equilibrium, due to finite size of CNC, would affect the elastic properties. In addition, the deformation mechanism of CNC can be better understood and verified by deriving analytical expressions of the most important elastic properties. The initial assumption that bonded and non-bonded interactions could be decoupled was later validated by our simulations and analytical equations. Our results indicated that individual axial stiffness of the chains (i.e. EA) was the main contributor to the overall mechanical properties of CNC. For instance, we showed that the overall EA of a CNC is practically given by the sum of the EA from the individual chains (chapter 5). This was demonstrated by showing (1) that the inter-chain h-bonding has a minor effect on the total stiffness of CNC (less than 5%) and (2) that our analytical expression for E_z for a CNC, which is only based on the individual chains' EAs , is consistent with the CM and MD results.

Three tension tests along the x (i.e., VdW dominant), y (h -bond dominant), and z (i.e., covalent bond dominant) directions were performed. We first consider the contribution of VdW forces in the x direction, which leads to 35% error in comparison with MD in the prediction of E_x . However, after adding the h -bond stiffness, such error was reduced to only 5%. We showed that the analytical solution for E_x is indeed in the range of the values obtained with MD, showing that imperfections due to equilibration process has little effect on the values. For elastic modulus in the y direction, both CM and MD predict 18-22 GPa, which is below the predicted value by analytical solution for perfect crystal ($E_y=26-36$ GPa). This shows that the imperfection due to equilibration could reduce the elastic modulus in the y direction by 30%. In addition we conclude that the contribution of h -bonds to E_y is approximately 50% and the other half is provided by VdW forces. For tension in the z direction, the results indicate that only covalent bond and intra-chain h -bonds are the main source of stiffness in E_z . On the other hand, inter-chain h -bond or VdW forces contribute to less than 5% to the overall stiffness. The analytical solutions for E_z were shown to agree reasonably well with the MD results, indicating that the imperfections introduced to equilibration in the MD process have a negligible effect on E_z . In addition, the analytical solutions suggests that E_z is size dependent with values of 100-250 GPa for very narrow and wide CNCs respectively and a range of 115-135 GPa for typical CNC size. The analysis of shear deformation showed a similar agreement between CM and MD. For $shear_{xy}$, the results indicate that 30% of G_{xy} is provided by h -bond stiffness and 70% by VdW interaction. However, the analytical solution for G_{xy} in a perfect crystal is 40%

higher than MD results, demonstrating that G_{xy} is sensitive to deviations of the structure from the perfect crystal. For both $shear_{xz}$ and $shear_{yz}$, only VdW interactions contribute to the shear modulus (G_{xz} and G_{yz}). In $shear_{xz}$ only inter-plane VdW stiffness (i.e., Equation 6.19) affects the value for G_{xz} . However, for $shear_{yz}$ both, in-plane and inter-plane shear stiffness (i.e., Equation 6.20), contribute to G_{yz} . This effect leads to higher G_{yz} , 6.5 GPa, in comparison with the G_{xz} (2.0 GPa). Also the comparison of the shear modulus calculated from the analytical solutions (Equation 6.21 and Equation 6.22) with the MD results, suggests that structural imperfections due to equilibration have little effect on G_{xz} and G_{yz} . Analysis of the bending test around the y axis indicates that the non-bonded interactions are very unlikely to contribute to EI_{yy} (e.g., less than 20%). However, the same indicates that more than 80% is mainly provided by EA . By comparing the CM results with MD, for both bending tests, we can conclude that in the case of EI_{xx} , bonded and non-bonded interactions have equal contribution to bending stiffness. This is in contrast with the case of EI_{yy} , where EA is almost the only contributor. As a result, the value for EI_{xx} is 1.5 times more than EI_{yy} . Comparing the CNC with equivalent solid size in bending, $f = M/\kappa E_z I$, indicates that as the cross section of CNCs increase, they behave similar to solids in bending, $f = 1$, but for a typical CNC size the bending behavior is superior to solids ($f = 1.2-1.4$). The results show very small torsional stiffness in CNC, which indicates its tendency to twist even under very small torques (Hanley et al., 1997; Lotz and Cheng, 2005; Hadden et al., 2013; Zhao et al., 2013). Finally we investigated an orthotropic model using FEM for comparison purposes. Our results show that, although

FEM can capture the contribution of EA (chain stiffness) to the EI_{xx} and EI_{yy} , it fails to capture the contribution of the non-bonded interaction. This case is more noticeable in EI_{xx} .

CHAPTER 7. NEW COARSE-GRAINED MODEL FOR ELASTICITY, FRACTURE AND DEBONDING OF CNCs

(A version of this chapter is under review for publication)

7.1 Introduction

Recently, there has been a great interest in to consider nanocellulose as a renewable material due to its potential application in replacing petroleum-based plastics and composites (Dufresne, 2017, 2013; Moon et al., 2011; Potulski et al., 2014). However, manufacturing of nanocellulose-based composites requires understating of their mechanical and chemical properties. Some recent studies include the analysis of the mechanical behavior of individual cellulose nanocrystals (CNC) particle from the experimental and computational point of view. (Chen et al., 2016; Dri et al., 2015, 2013; Lahiji et al., 2010; Sakurada et al., 1962; Tanaka and Iwata, 2006; Wagner et al., 2016; Wu et al., 2014) Different computational methods have been employed for CNC including ab initio calculations based on quantum chemistry,(Dri et al., 2013) molecular dynamics (MD) based on Newtonian physics,^{9,10,13,19} and continuum mechanics which considers discrete particles as continuous matter.(Chen et al., 2016) For instance, extreme elastic anisotropy was observed from ab initio calculations(Dri et al., 2013) suggesting a much higher modulus of elasticity in the chain direction. MD investigation on the strength of CNC with infinite length in three main directions showed higher strength in the chain direction due to covalent bond and smaller values for lateral directions due to hydrogen bond and Van

der Waals (VdW) forces.(Wu et al., 2014) Additionally, the interaction properties of CNC particles with water and other polymers were studied using MD.(Heiner et al., 1998; Jin et al., 2015; Kubicki et al., 2014; Matthews et al., 2006; Rahman et al., 2013; Sinko and Keten, 2015; Zhong et al., 2008) Sinko and Keten studied the shear and tensile failure of the interfaces between CNCs and proposed analytical model to describe their energy landscapes.(Sinko and Keten, 2015) Most of the MD studies considered shorter CNCs and a low number of particles interacting due to computational limitations. In addition, one study showed that the predicted elastic properties of CNC calculated with MD strongly depend on the forcefield.(Dri et al., 2015) A recent study proposed a finite element continuum-based structural modeling approach for the mechanical behavior of CNCs that can capture very well different deformation modes of the particles. However, extension to large deformation still remains challenge. (Shishehbor et al., 2018) There have been a few previous works that have proposed *coarse-grained* (CG) models for CNC to enable the modeling of real size of CNCs (e.g., 100-1000 nm in length), and/or to increase the number of particles involved in a given simulation or simulation time. (Glass et al., 2012; Hynninen et al., 2011; Li et al., 2015; Poma et al., 2017; Qin et al., 2017; Srinivas et al., 2014, 2011; Wohlert and Berglund, 2011) The idea behind CG models is to replace group of atoms with one representative atom called “bead” to decrease the number of degree of freedoms in the system while maintaining the main properties of interest.(Buehler, 2006b; Hsu et al., 2014; Z. Meng et al., 2017; Noid, 2013; Takada, 2012; Tozzini, 2005) One key challenge in CG models is the description of the interactions between the beads, especially because there is no systematic approach for developing CG potentials.(Noid, 2013) Previous CG models

for CNC can be categorized into two main groups: (1) CG models with three beads per glucose ring (ring),(Glass et al., 2012; Hynninen et al., 2011; Wohler and Berglund, 2011) and (2) CG models with one bead per ring.(Fan and Maranas, 2015; Li et al., 2015; Poma et al., 2017; Srinivas et al., 2014, 2011) Three beads per rings CG models are more detailed and able to model directionality of hydrogen bonds,(Fan and Maranas, 2015) however they are not coarse enough to study large systems. In addition, these models do not provide stable CNC structure unless they are constrained.(Glass et al., 2012) As an alternative, the single site models were employed to study transition of CNC from crystalline to amorphous,(Srinivas et al., 2014) and mechanical properties such as elastic modulus, persistent length,(Glass et al., 2012) and conformation of long fibrils.(Fan and Maranas, 2015) However, one major drawbacks for single CG site models is the lack of directionality as the hydroxyl group in the glucose are neglected when replacing it with one bead. Recently, Fan and Maranas proposed solvated single site CG model that solve the directionality problem by including bonded potentials between CG beads and employed the model to study long fibril.(Fan and Maranas, 2015) Up to now, most the CG models developed for CNC have focused in the interaction of a single CNC particle with water,(Fan and Maranas, 2015; Hynninen et al., 2011; Srinivas et al., 2014; Wohler and Berglund, 2011) or other materials,(Li et al., 2015) and mostly focus on the chemical and conformational properties rather than on the mechanical properties, except for few studies.(Glass et al., 2012; Poma et al., 2017; Qin et al., 2017) Recently Qin, et al. proposed a spring-bead model for mechanical and interfacial properties of the CNC; to study mechanical properties of bioinspired brick and mortar structure of CNC.(Qin et al., 2017)

In this work, we propose a CG model focused mainly on mechanical and interfacial properties of CNC. We surmise that this model in particular will enable the modeling of the mechanical response of many CNC particles and still provide enough details about the deformation of the individual CNCs and CNC-CNC interfacial properties.

7.2 CG Model Representation

Since the main purpose of the CG model is to simulate the mechanical properties of groups of CNC particles in a very efficient manner, some structural-chemical details are typically left out.(Noid, 2013; Takada, 2012; Tozzini, 2005) In order to determine the minimum amount of details required to model the interaction between CNCs, we focus our attention in the analysis of the behavior of two CNCs particles sliding on one another under shear loading to obtain a fundamental understanding of this particular interaction (Figure 7.1). Force-displacement curves for shearing of interface along the length of two CNCs from our MD simulation (details of MD simulation is explained in sec. 2.4.2) shows a stick-slip behavior with 1.038 nm frequency (solid black line in Figure 7.1b). This phenomena has also been reported by Sinko and Keten,(Sinko and Keten, 2015) and evaluated in the form of work of adhesion-displacement curves. This is due to the fact that each successive ring in cellulose is rotated 180 degrees (around the longitudinal axis or z axis, Figure 7.1a) relative to the last repeat unit. As such, two glucose chains interact with a frequency of 1.038 nm (2×0.519 nm) under an external applied shear loading alongside the chain direction (Figure 7.1b). Here we compare three different possibilities for representing CG bead in our model. (1) 1 bead per ring where the distance between two consecutive beads

is 0.519 nm. (2) 1 bead per two rings where the distance between two consecutive beads is 1.038 nm and (3) 1 bead per 6 rings (the 6 rings is an arbitrary large number as a representation of a very coarse case study) where the distance between two consecutive beads is 3.114 nm. Figure 7.1b compares normalized force-displacement curve from AA MD simulation (black solid line) with schematic of force-displacement curves for bead-spring model of different bead representations. Since the frequency of force-displacement curves in the CG models is equivalent to the bead-bead distance (0.519, 1.038 and 3.114 nm for case (1), (2) and (3) respectively), as it is shown in Figure 7.1b, only the frequency of the blue dashed line, representing CG model with 1 bead per two rings, is the same as AA frequency. I need to explain energy here. Although it is also possible to have a model with different CG beads for different rings (each bead type represents different ring), such model would increase the number and types of beads and therefore the simulation cost. In this work, based on the above discussion, the CG structure is formed by replacing two rings in CNC with a single bead (Figure 7.2b).

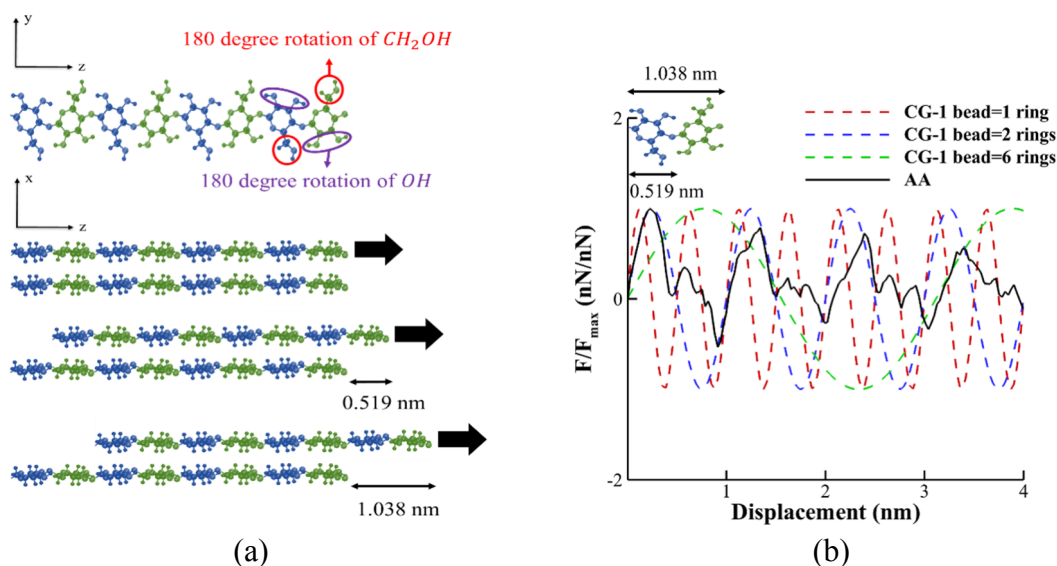


Figure 7.1 Justification of using two glucose units (disaccharide) per CG bead. (a) 180 degree rotation of successive glucose units around z axis (backbone chain) relative to the previous repeat unit are shown with green and blue colors. Slip-stick behavior of moving two cellulose chains with 1.038 nm frequency is due to sliding of same and opposite groups on top of each other. (b) Normalized force-displacement curves from AA MD simulation (black solid line) is compared with different CG bead representations. The frequency of the blue dashed line, representing CG model with 1 bead per two glucose units, is the same as AA frequency.

The methodology to define the interaction between beads is based on the assumption that, the interaction between CNCs is, in general, weaker than the strength and fracture energy of the individual CNC. In other words, unless the two particles are highly aligned and the molecules chains are positioned in a way that the two CNC particles are merged into one supermolecule of CNC; the interaction between two particles will always tend to be weaker. Experiments show that the structure of CNCs is twisted alongside of its length,(Hadden et al., 2013; Hanley et al., 1997; Lotz and Cheng, 2005; Zhao et al., 2013) and the surface of

CNC particle is very likely to be less structured than the core of CNC. For a single CNC particle, the only bonded interaction is covalent bond along the chain direction and the chains inside the crystal are interacting through non-bonded interactions (e.g., h-bond and VdW forces). At the interface of CNC particles, the chains interact through non-bonded h-bond and VdW interactions (similar to chains inside a particle, but weaker as explained above). In order to distinguish between the interface properties of two CNCs and the properties of the individual CNC, all the interactions in a CNC particle, e.g., both bonded and non-bonded, are defined through connected bonds; while the interaction between CNC particles is modeled through non-bonded pairwise interactions. Similar strategy was used in a continuum-based structural modeling approach for mechanics of a single CNC particle, where weak interactions between first neighbor chains were modeled with h-bond and VdW elements (Shishehbor et al., 2018). The bonds for a single CNC particle are shown in Figure 7.2c, d with b1, b2, b3, b4 and b5 representing VdW interaction in $[1\ 1\ 0]$, VdW interaction in $[1\ -1\ 0]$, h-bond and VdW in $[0\ 1\ 0]$, covalent bond in $[0\ 0\ 1]$ direction and VdW interactions between nearest non-bonded neighbors in $[0\ 0\ 1]$ direction respectively. Defining interactions through bonds b1-b5, which connects first neighbor beads, not only provides directionality in mechanical properties, but also enables us to model the interfacial properties of particles with non-bonded pairwise interaction (because all the bead-bead interactions inside the particle and within the cutoff distance are modeled with bonds).

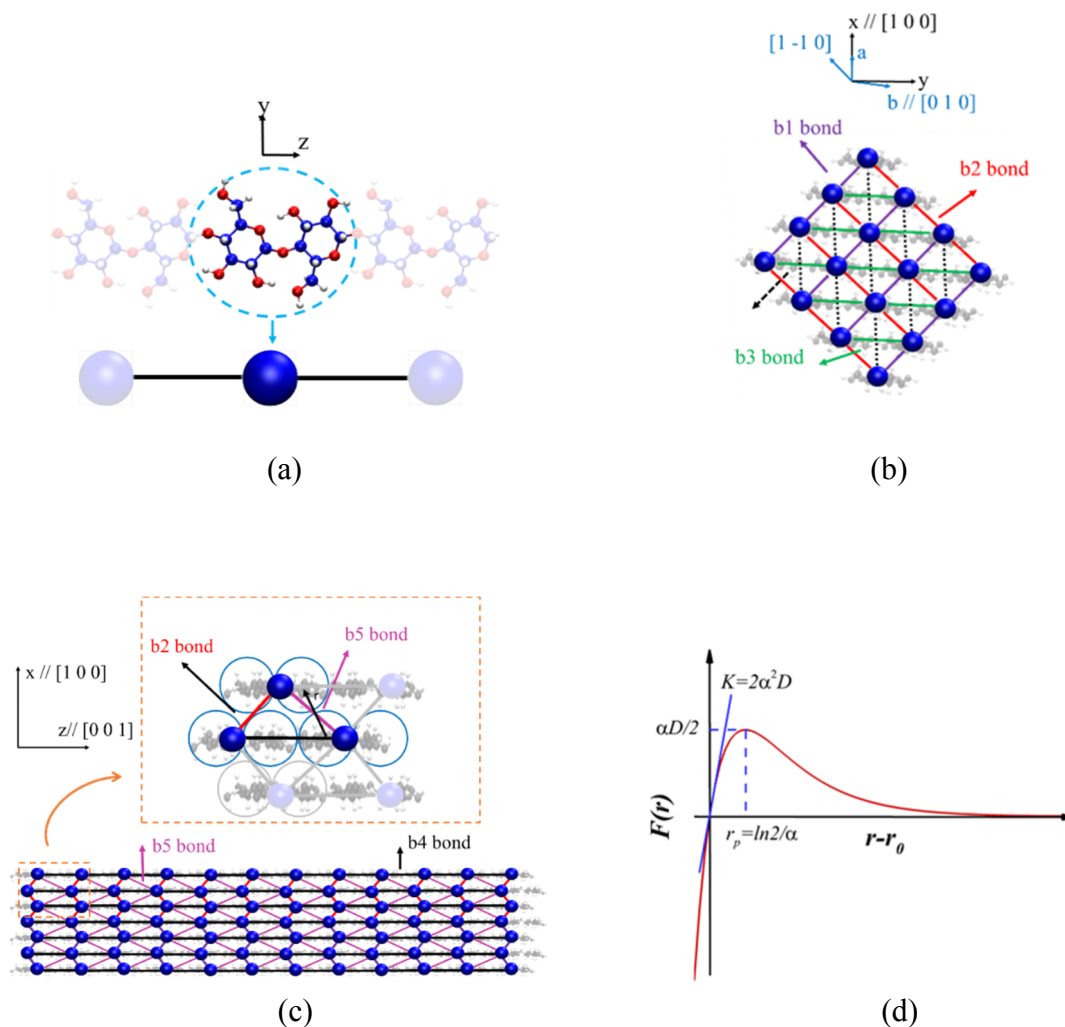


Figure 7.2 The structure of the Coarse-grained model. (a) Force-displacement curve for Morse potential which defines all bonds including covalent and weak bonds. The Instantaneous stiffness, bond strength and bond distance associated with bond strength are shown. (b) Replacing a two glucose units with one bead in a cellulose chain. (c) Cross section of CNC with diamond shape. The beads are shown with blue spheres which are connected with red and green breakable bonds, E_{wb} , to add directionality of Elasticity and strength in all directions (d) The side view of the CNC which shows the beads with blue spheres and the covalent bond which are connecting the beads in the cellulose chain direction with black lines.

Therefore, the beads interactions are defined by bonded and non-bonded interactions as follow:

$$E = E_b + E_{VdW} \quad (7.1)$$

Where E_b is the energy term for expressing the 5 bonds inside a CNC particle, representing covalent bonds, h-bond and VdW interactions inside a particle, and E_{VdW} represents the weak interactions, e.g., h-bond and VdW interaction among CNCs to model the interface. Note that, based on MD results, we assume no bending or torsional energy term contribution to the total energy of the system due to their small effect on the mechanical properties [80]. For the interaction between two CNC particles, VdW interactions (E_{VdW}), we employ Lennard-Jones (LJ) potential function which only needs two parameters for modeling VdW dispersion and has been used in many previous studies before:(Brooks et al., 1983; Fan and Maranas, 2015; Glass et al., 2012; Srinivas et al., 2014, 2011; Wohlert and Berglund, 2011)

$$E_{wv}(r) = 4\epsilon \left[\left(\frac{\sigma}{r} \right)^{12} - \left(\frac{\sigma}{r} \right)^6 \right] \quad (7.2)$$

Where ϵ is the energy of the potential at equilibrium, minimum energy, σ is the distance parameters and r is the distance between two beads. To be able to model both the elasticity and strength of CNC in all directions, the energy terms associated with bond, E_b , must be able to capture both initial and dissociate phases of a stress-strain curve. The simplest

potential for modeling dissociation of a bond is Morse potential, which needs only 3 parameters to be defined:

$$E_b(r) = D[1 - e^{-\alpha(r-r_0)}]^2 \quad (7.3)$$

Where D is the energy depth, α is characterization parameter and r_0 is the bond equilibrium distance. The force and stiffness of the Morse potential can be obtained through the first and the second derivative of E_b with respect to r , respectively. Note that due to bond dissociation, the stiffness of Morse potential is not constant and decreases by increasing the bond distance.

$$F_b(r) = \frac{dE_b}{dr} = 2\alpha D e^{-\alpha(r-r_0)} [1 - e^{-\alpha(r-r_0)}] \quad (7.4)$$

$$K_b(r) = \frac{d^2E_b}{dr^2} = 2\alpha^2 D e^{-\alpha(r-r_0)} [-1 + 2e^{-\alpha(r-r_0)}] \quad (7.5)$$

Figure 7.2c shows the force-distance curve, stiffness and maximum force for Morse potential. The instantaneous stiffness is $K = 2\alpha^2 D$ obtained by setting $r - r_0 = 0$ in Equation 7.6 and the maximum force is $F_{max} = \alpha D / 2$ attained at $r - r_0 = \frac{1}{\alpha} \ln 2$ by setting $K_b = 0$ in Equation 7.7. There are 3 parameters, D , α and r_0 , for Morse potential of each bond (e.g., D^i, α^i, r_0^i for $i=1, \dots, 5$). The parameter r_0 , associated with the initial bond length, is known through the structure of CNC (different values of r_0 associated with different

bonds are obtained from lattice parameters); and D , α are defined to satisfy the mechanical properties of CNC in different directions. The parameter α , is the only parameter that controls the strain at peak of a strain-stress curve, $\epsilon_p = \frac{1}{\alpha} \ln 2 / r_0$, and therefore can be found to satisfy the strain at peak from AA simulation (section 2.3.1). To find the unknown parameters (D^i, α^i) in our CG model, we define a relationship between bonds b1-b5 and by finding the parameters for bond b1, D^1 and α^1 , the parameters for b2-b5 are automatically defined. We assume that the mechanical properties of the bonds b1 and b2 are identical due to nearly symmetrical shape of CNC around x axis as shown in Figure 7.2c and therefore they have the same D and α . Bond b3 is in the h-bond plane and represents h-bond and VdW interaction between two chains. Previous study focused on the continuum-based structural model for elastic properties of CNC,(Shishehbor et al., 2018) suggests that the stiffness of the bond b3 is twice of the b2 counterpart and therefore D^3 is twice of D^2 due to h -bond contribution. Bond b4 represents the covalent bond in AA simulation and we assume it is the main contributor for the stiffness and strength of CNC particle in the chain direction (z axis in Figure 7.2d) as suggested by previous studies.(Shishehbor et al., 2018; Wu et al., 2014) Bond b5 connects the nearest non-bonded neighbors in the chain direction and it is necessary to include this bond for excluding all the bead-bead interactions inside the CNC. The bond energy for b5 and b1 can be estimated from the interaction of rings involved in each bond. As shown in Figure 7.2d, for bond b1, 3 rings with distance r and 1 ring with distance $2r$ are interacting, while for bond b5; 1 rings with distance r , 2 with distance $2r$ and 1 with distance $3r$ are interacting. Therefore, the

relationship between the energy of bond b5 and b1 can be estimated by the sum of all interacting rings using the attraction term of LJ potential (scales with r^{-6}) as follow:

$$\frac{E_{b5}}{E_{b1}} \cong \frac{\frac{1}{r^6} + \frac{2}{(2r)^6} + \frac{1}{(3r)^6}}{\frac{3}{r^6} + \frac{1}{(2r)^6}} \cong 0.34 \quad (7.8)$$

Which indicates that the Energy of bond b5 is approximately $\sim 1/3$ of bond b1 and therefore, D^5 is adopted as $1/3$ of D^1 .

7.3 CG Model Characterization

To determine the associated parameters in our CG model, series of mechanical tests are performed for CG modeling and compared with AA modeling and experimental data. The parameters for bonds b1-b5, are obtained through tensile loading indifferent directions; while the non-bonded parameters are obtained through adhesion energy between two CNC particles. The MD package LAMMPS,(Plimpton, 2007) is used for all the simulations including both AA and CG modeling, employing the CHARMM force field for AA model.(Brooks et al., 1983; MacKerell et al., 2010) The set of potentials used for the CG model are explained in section 2.1. The timestep for MD simulations has to be small enough to capture the vibrational frequency of the smallest atom. For AA simulations, the timestep is 2 fs after constraining the hydrogen atom using shake algorithm.(andersen, 1983) For CG model, a series of equilibration test in NVE ensemble for different timestep have been conducted. This simulations shows that for a timestep larger than 20 fs the

structure is not stable anymore, therefore a timestep of 10 fs which is fast and safe enough for our simulations is chosen. The CNC structure used for CG simulations is shown in Figure 7.2. with 12.45 nm length and 192 beads which represents AA model with 8112 atoms. The cross-section we have chosen for parametrization and verification has 16 chains to reduce computational cost on AA simulations. However, our model can be extend to different cross-section sizes with less than 1% error in elasticity and strength and less than 5% error in surface energy (as shown in appendix A1 for 16, 36 and 64 chains). In all the simulations, the system is first minimized and then equilibrated in the NVT ensemble at $T=300\text{k}$ for 2 ns.

7.3.1 Tensile Loading

In order to model anisotropic behavior of CNC(Dri et al., 2013) (due to different type of interactions e.g., VdW, covalent and *h*-bonding) in our CG model, we perform tensile loading in three perpendicular directions (e.g., [001], [-1 1 0] and [1 1 0]) and compare the stress and strain curves in all three directions. As it is known, classical forcefields like CHARMM are not able to model bond dissociation which means that the analysis is limited to elastic modulus in the covalent bond direction ([001]). However, the strength of CNC in the covalent bond direction can be compared with previous studies from reactive forcefield and experiment.(Saito et al., 2013; Wu et al., 2014) For stretching in the *z* direction, covalent bond direction, the oxygen atoms in the first ring of each chain are fixed while the stretching deformation is applied to the oxygen atoms in the last ring of each chain at the strain rate of $1 \times 10^8 \text{ s}^{-1}$. To prevent the CNC from twisting during the equilibration,

the movement of oxygen atoms in the boundary chains are constrained in the direction perpendicular to the loading direction (xy plane). The elastic modulus of CNC in the covalent direction is 130-150 GPa from AA which is comparable with 145 GPa reported from experiments,(Iwamoto et al., 2009; Moon et al., 2011) and 110-200 GPa from simulations.(Dri et al., 2013; Wu et al., 2013) The suggested value for the strength of CNC from experiment is 2-6 GPa,(Iwamoto et al., 2009; Saito et al., 2013) while for the AA simulation with reactive force field a range of 5-8 GPa.(Wu et al., 2014) We chose a strength of 5.5 GPa which is in the range of both experimental and numerical values.

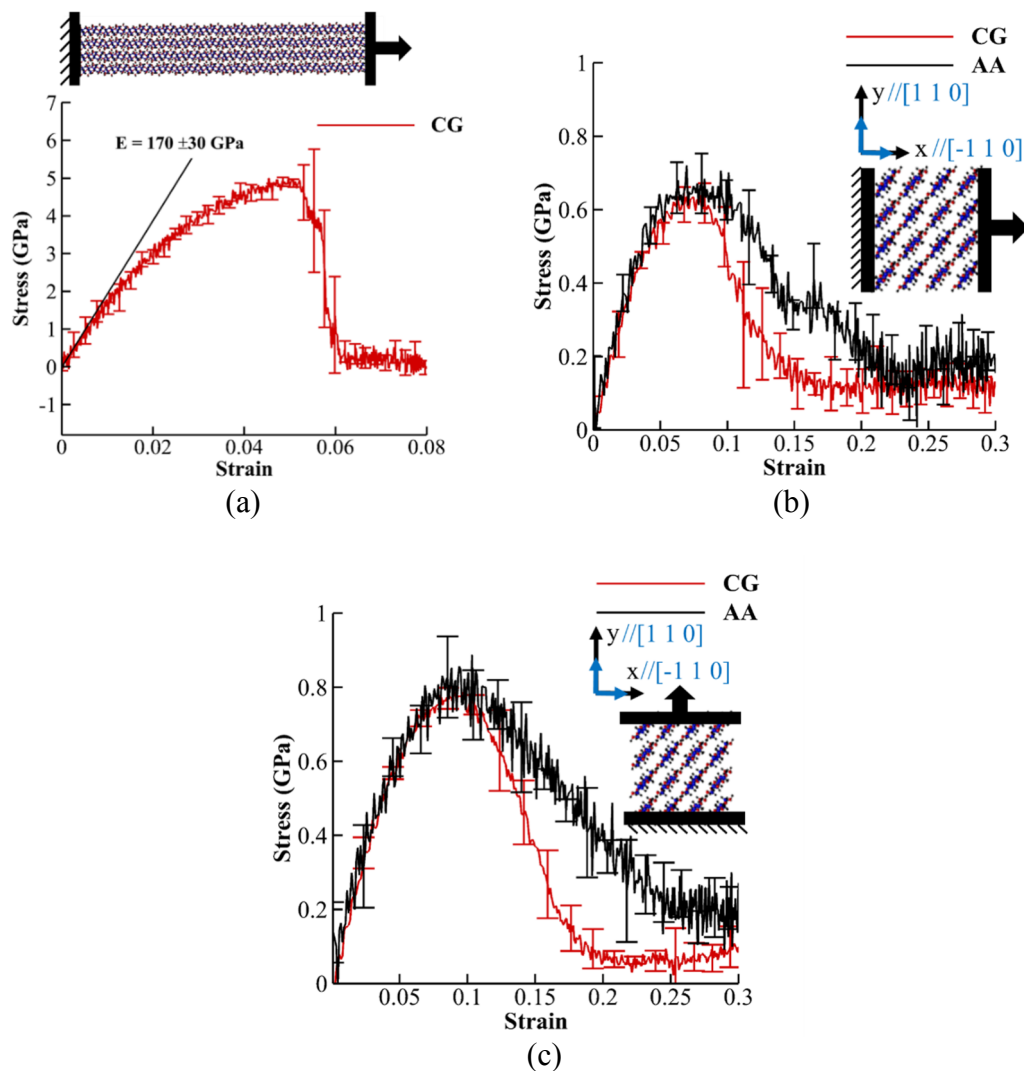


Figure 7.3 Tensile loading in the chain direction for parametrizing covalent bond. (a) tensile loading in the chain direction (b) tensile loading perpendicular to the chain direction for parametrizing weak bonds. (c) tensile loading perpendicular to the chain direction for parametrizing weak bonds.

For stretching in the x direction, the oxygen atoms on the left boundary are kept fixed while the strain is applied on the oxygen on the right boundary at the strain rate of $1 \times 10^{-4} \text{ ps}^{-1}$. The same procedure is performed for the y direction, except, the fixed and loaded oxygen atoms are on bottom and top boundaries respectively. The elasticity modulus obtained from AA simulations for both the x and y directions is 12 GPa which is comparable with the range of 10-25 GPa reported values from experiments, (Wagner et al., 2016) and 5-25 GPa range from different numerical methods such as density functional theory, (Dri et al., 2013) classical forcefield, (Wu et al., 2013) and reactive force field. (Wu et al., 2014) The strength of CNC from AA simulation in the x and y directions are 0.7 and 0.8 GPa respectively, Figure 7.3b and c, which are comparable with the range of 0.5-0.9 GPa from reactive forcefield (Wu et al., 2014). Therefore, both the elasticity and strength of CNC in the transverse direction from AA simulation are in the expected range of values. From AA simulations, the strain at peak for tensile tests in x and y directions are around 0.1 with $r_0 \cong 6.0 \text{ \AA}$ (Figure 7.3 b, c) and for z direction is around 0.06 with $r_0 = 10.38 \text{ \AA}$; therefore the parameter α for b1-b6 can be estimated from the ϵ_p in Morse potential

$$\epsilon_p = \frac{r-r_0}{r_0} = \frac{\frac{1}{\alpha} \ln 2}{r_0} \quad (7.9)$$

From Equation 7.10, and by replacing the strain from AA and r_0 from geometry consideration, the parameter $\alpha = 1.0$ shows a good estimation for the strain at peak of the stress-strain curves (0.11 for x and y and 0.06 for z direction). As explained above, only D^1

and D^4 needs to be defined because D^2 , D^3 and D^5 are related to D^1 ; and bond b4 individually defines the mechanical properties of the CNC along the chain direction. From Equation 7.11 and Equation 7.12, after defining the parameter α , the parameters D can either be obtained from the elastic modulus (based on $K = 2\alpha^2 D$) or the strength (based on $F_{max} = \alpha D/2$). Here we estimate the D parameter from the strength rather than the elastic modulus to be able to fix the point associated with strength and failure strain, α already satisfies ϵ_p , in the stress-strain curve and therefore, knowing that the stress-strain curve before failure is almost linear, (Qin et al., 2017; Wu et al., 2014) we assume that the value for the elastic modulus will be satisfied automatically. The strength of CNC in the lateral direction can be related to the strength of bond b1 (the weakest bond in our model which represents only VDW interactions and is parallel to the loading) as follow (maximum force is shown in Figure 7.2d):

$$D = \frac{2F_{max}}{\alpha} = \frac{2A\sigma_{max}}{\alpha} \cong 10.75 \text{ kcal. mol}^{-1} \quad (7.13)$$

Where $A = 6.0 \times 10.38 \text{ (\AA}^2\text{)}$ is the area associated with bond b1, and the strength, $\sigma_{max} = 0.6/6.95 \cong 0.0863 \text{ kcal. mol}^{-1}\text{\AA}^{-3}$. As mentioned in section 2.2, and based on the relationships between the bonds, the D parameters for bond b2, b3 and b5 are therefore 1, 2 and 0.33 times of the D parameter for bond b1, respectively. Finally, the strength of the CNC in the longitudinal direction (chain direction) is defined by the D parameter in the bond b4 as follow:

$$D = \frac{2F_{max}}{\alpha} = \frac{2A\sigma_{max}}{\alpha} \cong 56.0 \text{ kcal. mol}^{-1} \quad (7.14)$$

Where A is the area associated with bond b4, 6.0×6.5 (\AA^2) and the strength is equal to $5.0/6.95 \cong 0.71942 \text{ kcal. mol}^{-1}\text{\AA}^{-3}$. The fitted stress-strain curve for stretching in the z , x and y directions from our CG model is shown with red line in Figure 7.3a, b and c respectively. For the z direction, CG model shows elastic modulus of 140-200 GPa and strength of 4-5.5 GPa. It is worth to mention that although the elastic modulus in the chain direction from CG is $\cong 1.1-1.4$ of the AA counterpart (140-200 and 130-150 GPa from CG and AA respectively.), it is more aligned with the reported values from ReaxFF (150 GPa),(Shishehbor et al., 2018) and density functional theory (200 GPa).(Dri et al., 2013) For the x and y directions, the CG model not only provides the same elasticity and strength as AA (less than 5% error). After finding all the bond parameters for Morse potential, the LJ parameters for bead-bead interaction are obtained from the adhesion energy between two CNC particles in the next section.

7.3.2 Adhesion Energy

Understanding the adhesion energy between two CNCs is crucial for modeling the interaction between CNC particles. Peng et al, (Peng et al., 2013) evaluated the effect of drying method and column temperature on the surface energy of dried CNCs using inverse gas chromatography and reported a range of 45-70 mJ/m². In AA MD simulations of CNC, the adhesion energy is modeled by electrostatic (including the h-bonding) and VdW

interactions between two CNC particles.(Kong and Eichhorn, 2005; Sinko and Keten, 2015) However, in the proposed CG model, the beads do not possess any electrical charges and only VdW interactions among beads contribute to adhesion energy. Having beads with no electrical charges, significantly reduces the computational time,(Demille and Molinero, 2009) and has been employed before for CG modeling of CNC,(Fan and Maranas, 2015; Glass et al., 2012; Poma et al., 2017; Srinivas et al., 2014, 2011; Wohlert and Berglund, 2011) and other nanomaterials.(Abberton et al., 2013; Arash et al., 2015; Hsu et al., 2014; Ruiz et al., 2015; Xia et al., 2016; Yazdandoost et al., 2017; Zhang et al., 2018) Here the VdW parameters in our CG model can be fitted by comparing CG and AA modeling of the interfacial energy changes as a function of separation of two CNCs where the particles are interacting in the transverse and longitudinal directions ($[1 -1 0]$ and $[0 0 1]$ planes respectively as shown in Figure 7.4). To be able to compare the surface energy obtained from our simulations with experimental results, CNCs are free to twist during the equilibration. For pulling and separating the particles in the prescribed direction and obtain the changes in interfacial energy as a function of separation for both AA and CG models, steer molecular dynamics (SMD) method is used.(Park et al., 2003; Sinko and Keten, 2015) To find the free energy differences from the averaged SMD simulation, multiple initial conformations for SMD simulation is required,(Park et al., 2003; Sinko and Keten, 2015) which is acquired by taking configuration of the system every 100 ps after equilibration. For all the SMD simulations, the pulling is performed by attaching a spring with high stiffness of $500 \text{ Kcal/mol\AA}^2$ to the center of mass of the tethering particle and moving it under constant velocity of 0.0002 \AA/fs (5 m/s). For SMD in the $[0 0 1]$ surface, the CNC

particle on the right side (cartoon in Figure 7.4a) is tethered, all atoms in the right particle are constrained to move only in the pulling direction, while the oxygen atoms in the left boundary of the left particle is fixed. The potential of mean force (PMF), integral of force-displacement curve, is obtained by averaging 10 SMD simulations with different initial configuration. The same procedure is done for $[-1 \ 1 \ 0]$ direction with only changing the pulling direction, contained atoms and the fixed boundary. For the CG model, the initial values for LJ parameters (i.e., ϵ , σ and cutoff distance) are estimated from the AA surface energy curves (Figure 7.4a, b). From the AA SMD simulation, Figure 7.4.a, b, the surface energy for lateral interaction ($[-1 \ 1 \ 0]$) is 60 (mJ/m²) or 863 (Kcal/molÅ²); and by assuming the first neighbor interaction between beads, the ϵ can be approximated by dividing the surface energy over the total number of interactions on the surface ($\epsilon = 863/192 \cong 4.5 \text{ kcal. mol}^{-1}$). The equilibrium distance, σ , should be a value between 10.38 Å and 6.0 Å for fulfilling the both longitudinal and lateral equilibrium distance (We should note that here the average value of $\sigma = 8 \text{ Å}$ is taken). Finally, Figure 7.4a, b demonstrate that after 5 Å separation distance, two CNC particles are not interacting anymore; therefore a cut off distance of (8+5=13 Å) is selected for bead-bead interactions.

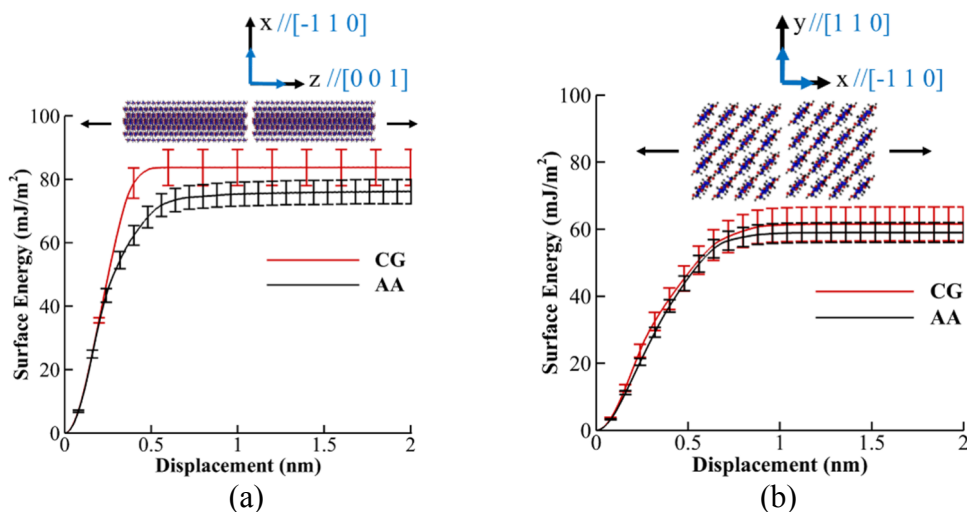


Figure 7.4 Comparison of the surface energy for AA and CG models obtained from averaging 10 SMD simulations. (a) Front Surface ([0 0 1]). (b) Side Surface ([1 1 0]).

Finally, to compare CG with AA, the same AA SMD procedure is repeated for the CG model with the initial estimated parameters. Figure 7.4 displays the PMF curves for the AA and CG model for [0 0 1] and [1 1 0] directions with, $\sigma = 8 \text{ \AA}$, $\epsilon = 5 \text{ kcal.mol}^{-1}$ and the cutoff distance of 13 \AA . Note that, to find the best fit to the AA results, different values of ϵ (e.g., 4, 4.5, 5, 5.5 kcal.mol^{-1} which are close to the initial estimated value $\cong 4.5 \text{ kcal.mol}^{-1}$) was tested and finally $\epsilon = 5 \text{ kcal.mol}^{-1}$ was adopted and shown in Figure 7.4. Table 7.1 shows all the final values for the parameters in bonded and non-bonded interactions in our CG model after modifying the initial values for the best fit (Figure 7.3 and Figure 7.4).

Table 7.1 Force field parameters for CG model of Cellulose I β

| Interaction | Function | | |
|--------------------|--|-------------------|---------------------------|
| Bonded | $E_b(r) = D[1 - e^{-\alpha(r-r_0)}]^2$ | | |
| Type | Parameters | | |
| | $D(kcal.mol^{-1})$ | $r_0(\text{\AA})$ | $\alpha(\text{\AA}^{-1})$ |
| b1 | 11.0 | 5.98 | 1.0 |
| b2 | 11.0 | 6.56 | 1.0 |
| b3 | 22.0 | 8.2 | 1.0 |
| b4 | 60.0 | 10.38 | 0.95 |
| b5 | 4.0 | 9.5 | 1.0 |
| Non-bonded | $E_{vw}(r) = 4\epsilon[(\frac{\sigma}{r})^{12} - (\frac{\sigma}{r})^6]$ | | |
| Type | Parameters | | |
| Bead-Bead | $\epsilon = 5.0 kcal.mol^{-1}, \sigma = 8.0 \text{\AA}, r_{cut} = 13 \text{\AA}$ | | |

7.4 Evaluating The CG Parameters For Different Width of CNC

In this section, the mechanical and interaction properties of CNC are examined for different cross-section size to make sure the model is still valid for larger cross-sections, especially for the CNC with 36 chains which is used more often in literatures.^{19,68} Figure 7.5a compares the stress-strain curves for CG with 16, 36 and 64 chains in the longitudinal direction respectively. The results shows less than 1% error in failure strain and less than 0.1% error in elastic modulus and strength as we change the cross-section. The stress-strain curves for two lateral directions are shown in Figure 7.5b and Figure 7.5c for different cross-sections. The error for elastic modulus, strength and failure strain are 1%, 5% and 30% respectively.

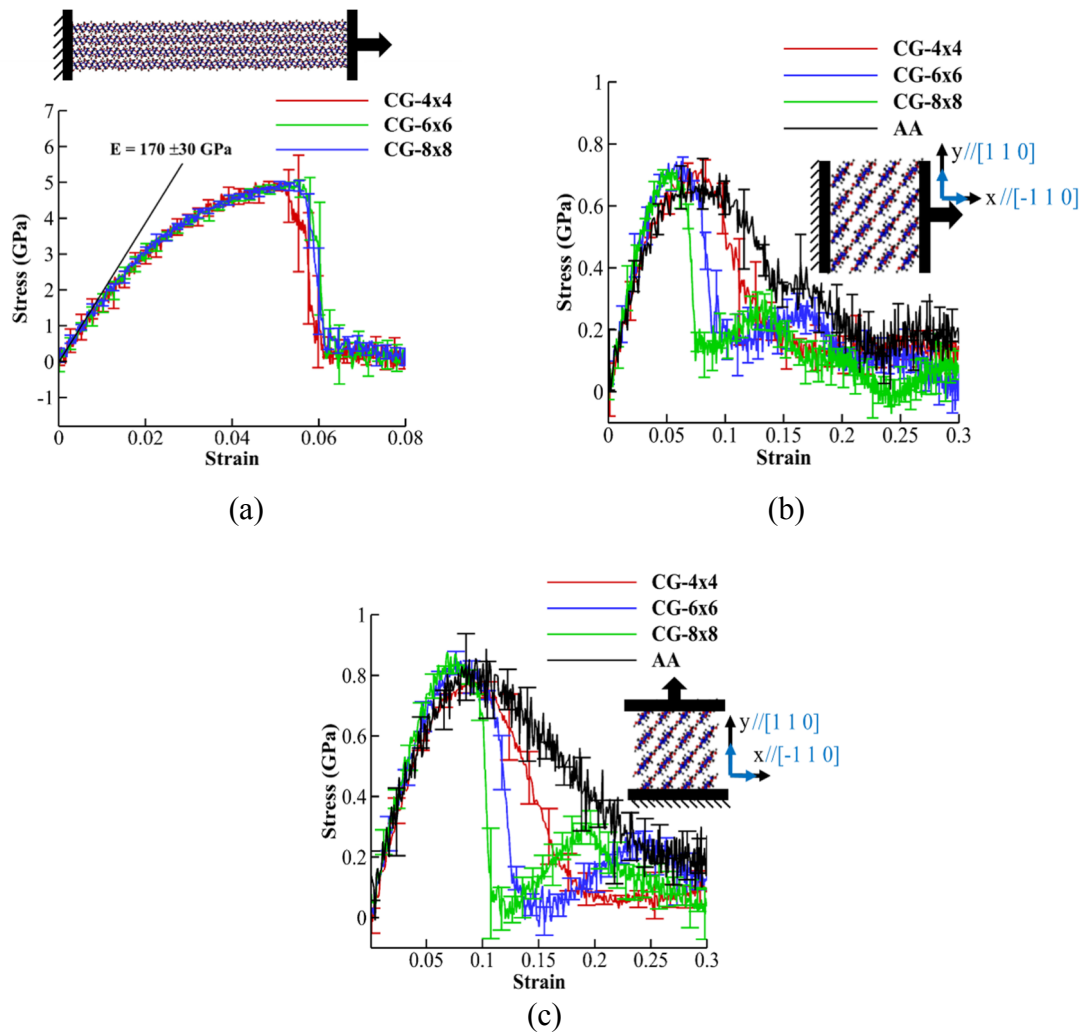


Figure 7.5 Stress-strain curves for CG model with different width and AA with 16 chains. (a) tensile loading in the chain direction (b) tensile loading in the $[-1 1 0]$ direction. (c) tensile loading in the $[1 1 0]$ direction

Note that for different width of CNC, the CG model shows size effect due to strain localization. To better show the size effect and compare the behavior of the post-peak, the stress-displacement curves of the post-peak are plotted in Figure 7.6a and Figure 7.6b for tensile test in the x and y respectively.

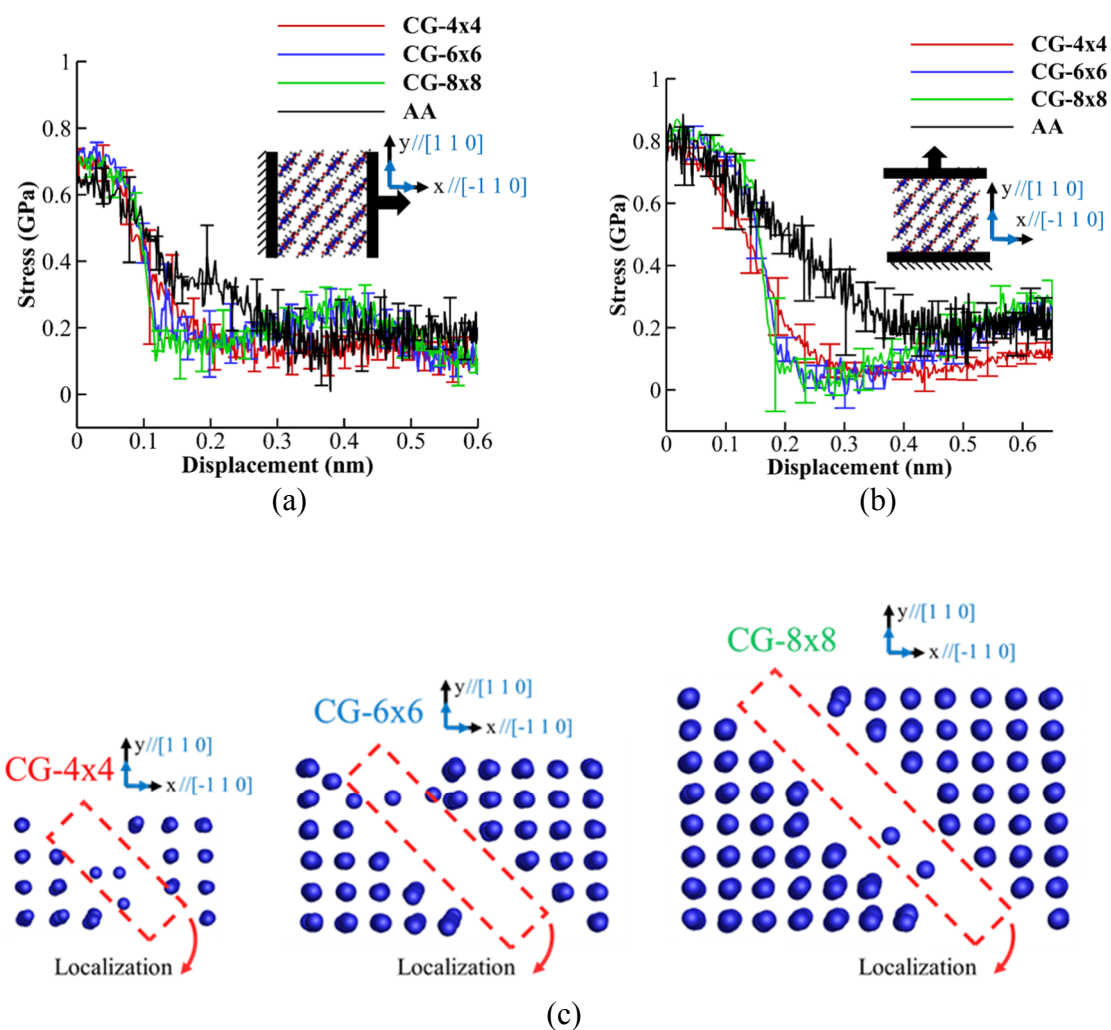


Figure 7.6 Stress-displacement curves for CG models with different with AA with 16 chains. (a) tensile loading in the $[-1\ 1\ 0]$ direction. (b) tensile loading in the $[1\ 1\ 0]$ direction (c) Strain localization of CG model with different size for tensile test in the $[-1\ 1\ 0]$ direction.

Figure 7.7a and Figure 7.7b compares the surface energy-displacement curves for CG with 16, 36 and 64 chains in the longitudinal ($[0\ 0\ 1]$) and lateral ($[-1\ 1\ 0]$) directions respectively. The results shows a good agreement among all CG models with different cross section size

(or number of chains) and with AA results (7%, 5% and 2% error for CG with 16, 36 and 64 chains respectively).

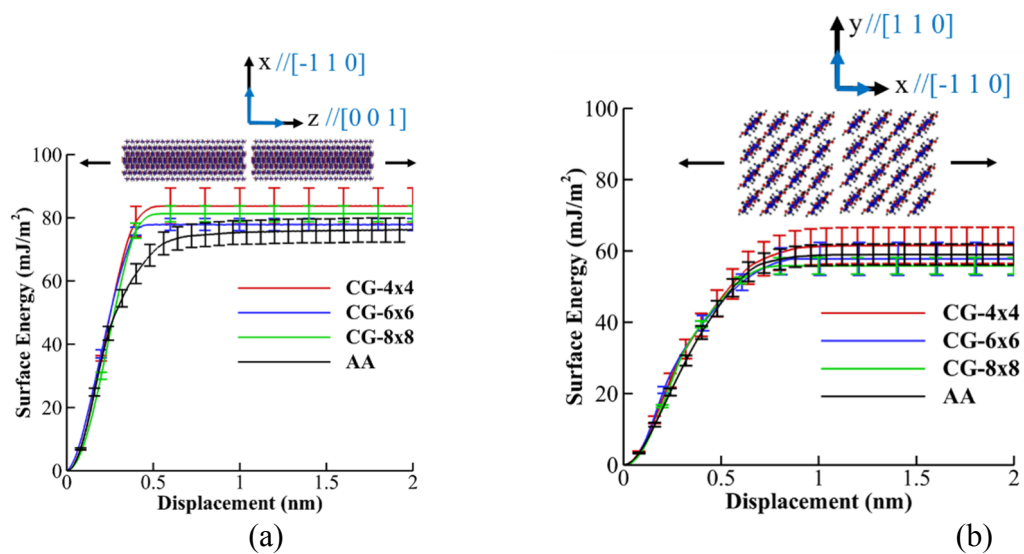


Figure 7.7 AA and CG adhesion energy Comparison. (a) Front Surface [0 0 1] and (b) Side Surface [-1 1 0].

CHAPTER 8. VALIDATION TESTS FOR THE CG MODEL

(A version of this chapter is under review for publication)

Our CG model was developed based on specific mechanical loading and adhesion energy to obtain associated parameters. Before applying the CG model to more complex case studies, we evaluate the model using some specific cases for validation purposes. Two bending tests in different directions are performed and compared with AA results to test the properties of the individual CNC. To test the interaction between CNCs, shear test between two CNCs and tensile test of a small staggered structure are evaluated. In all case studies, the system is minimized using the Hessian-free truncated Newton (hftn) algorithm, temperature is controlled by the Nosé-Hoover,(Leach, 2001) thermostat at 300 Kelvin and system is equilibrated for 2 ns in a NVT ensemble.

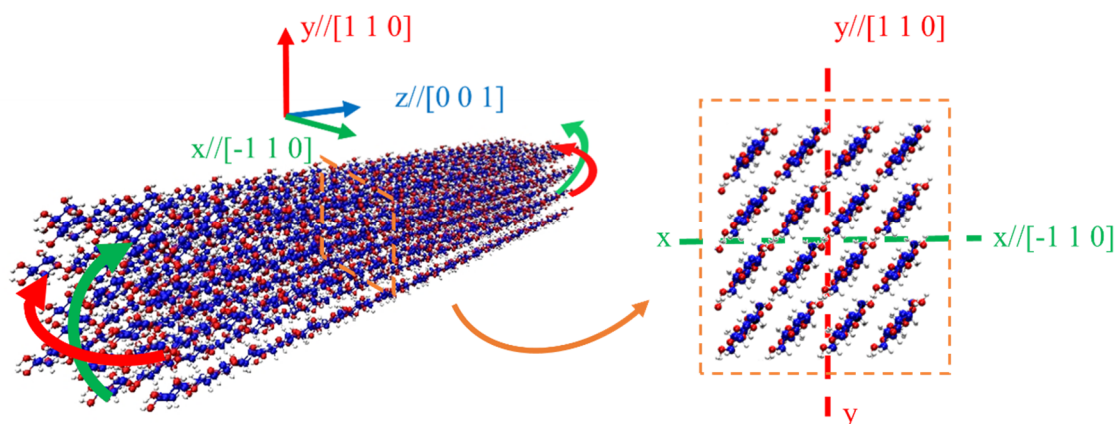
8.1 Bending of CNC

Here we also examine the bending of CNC using our CG model and compare it with AA results obtained from CHARMM. A previous AA MD and analytical study done to study the mechanical properties of CNC showed that the bending stiffness of CNCs is mainly related to the elastic modulus in the chain direction.(Shishehbor et al., 2018) As discussed in Sec. 3.1, the elastic modulus in the chain direction from CG is $\cong 1.1-1.4$ of the AA counterpart and therefore, we expect the bending stiffness from CG to be $\cong 1.1-1.4$ of the AA one. We should also mention that, in bending tests, AA simulations could only model

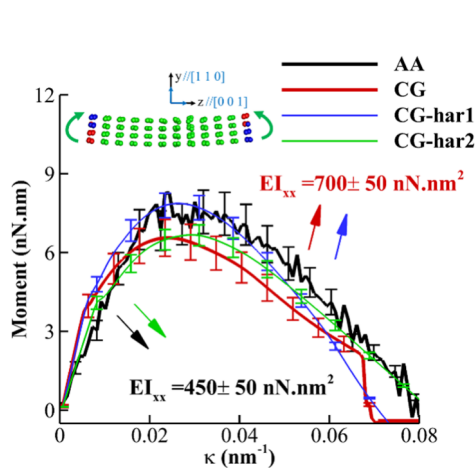
bending failure due to buckling (covalent bonds do not break in classical forcefields like CHARMM), while the CG model can also model covalent bond dissociation and failure. For all case studies, to prevent the CNC from twisting in AA model, the movement of the boundary atoms are contained in xy plane during the equilibration. The method we use to apply deformation and calculate moment-curvature is explained in details in (Shishehbor et al., 2018). Two bending tests around x and y direction which represent $[-1 \ 1 \ 0]$ and $[1 \ 1 \ 0]$ directions respectively are performed for both AA and CG models as shown in Figure 8.1a. The moment-curvature plots for bending around x and y axis are plotted in Figure 8.1b and Figure 8.1c respectively. The bending stiffness, EI , around x axis is 650-750 $\text{nN}\cdot\text{nm}^2$ and 400-500 $\text{nN}\cdot\text{nm}^2$ for CG and AA respectively (Figure 8.1b). For bending around y axis, EI is 500-600 $\text{nN}\cdot\text{nm}^2$ and 350-450 $\text{nN}\cdot\text{nm}^2$ for CG and AA respectively (Figure 8.1c). The EI values from CG are $\cong 1.1-1.4$ of the AA, as discussed above, and in the range of previous studies 500-900 $\text{nN}\cdot\text{nm}$ (Chen et al., 2016; Shishehbor et al., 2018). The maximum bending moment for both directions are around 7-9 $\text{nN}\cdot\text{nm}$ at an applied bending curvature of $\kappa = 0.025-0.035 \text{ nm}^{-1}$ for AA model. For CG model, the maximum bending moment is 6-8 $\text{nN}\cdot\text{nm}$ (14% error with respect to AA) at $\kappa = 0.02-0.03 \text{ nm}^{-1}$ (20% error with respect to AA). As mentioned above, the CG model can model covalent bond dissociation (as opposed to the AA model), therefore, lower values of bending strength and curvature at peak in CG model was predictable. In order to clarify the effect of covalent bond dissociation on the results, we also performed the bending tests using harmonic potential for covalent bond (same as AA, where covalent bond cannot break). The harmonic potential for defining elastic covalent bond is defined as:

$$E_h(r) = K_h(r - r_0)^2 \quad (8.1)$$

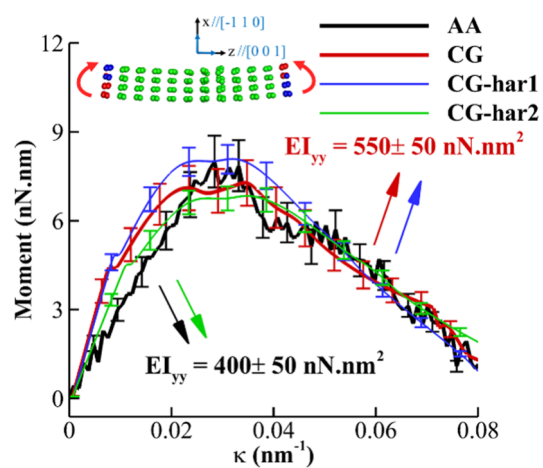
Where E_h is the energy term, K_h is stiffness of the bond and r_0 is the bond equilibrium distance. The parameters of the harmonic potential can be adopted to the parameters of bond b4 (Table 7.1) by replacing $r_0 = 10.38 \text{ \AA}$ and $K_h = K = 2\alpha^2 D \cong 108 \text{ Kcal/mol\AA}^2$. The results for bending around x and y axis from our CG model using harmonic potential for covalent bond are shown with blue line (CG-har1) in Figure 8.1b and Figure 8.1c respectively. The results shows increase in the bending strength (15% and 1% error with respect to CG and AA respectively) as expected. This indicates that bending failure is governed by buckling rather than covalent bond breaking in our bending tests. We have also performed bending tests with $K_h = 108/1.4 \cong 77 \text{ Kcal/mol\AA}^2$ for the CG case study (CG-har2 in Figure 8.1b and Figure 8.1c) with $E_z=130 \text{ GPa}$ (same as AA). The results (green line in Figure 8.1b and Figure 8.1c) demonstrates very similar trend as AA (same EI and 12% error in bending strength).



(a)



(b)



(c)

Figure 8.1 Comparing the Moment-curvature curve for bending around x and y axis and torsion of CNC from AA and CG modeling. (a) Cross-section of the CNC and the x and y axis have been shown. (b) Moment-curvature curve for bending around x axis. (c) Moment-curvature curve for bending around y axis.

8.2 Shear Between CNC Particles

The VdW parameters for our CG model have been characterized based on the normal separation between two CNC particles (as described in chapter 7, Figure 7.4a, b). Here the

separation of two CNC particles in the shear direction is performed as a validation test for the proposed CG model (as shown in schematic of Figure 8.2a). The effect of twisted/untwisted CNC on the performance is compared for two different setups: (1) AA-twisted where there is no constraints on the particles and the initial distance between two particles is large enough (more than cutoff distance) to allow them to twist first and then moved to form an interface. (2) AA-untwisted where the particles are prevented to twist, for that we place them with a initial distance between particles (5 \AA) and we allow the movement of boundary atoms (fixed atoms on the left side of the bottom CNC as shown in schematic of Figure 8.2a) only in the xz plane (they cannot move in the y direction) during the equilibration. For the shear test between two CNC particles, the CNC particle on top is tethered at the center by SMD while the boundary atoms on the bottom particle are fixed (as shown in the schematic of Figure 8.2a). Figure 8.2a displays the force-displacement curves for shear tests of the twisted and untwisted CNC particles using the AA and compared with CG models with different interfacial properties (i.e., $\epsilon/\epsilon_c = 1$ and $\epsilon/\epsilon_c = 2$).

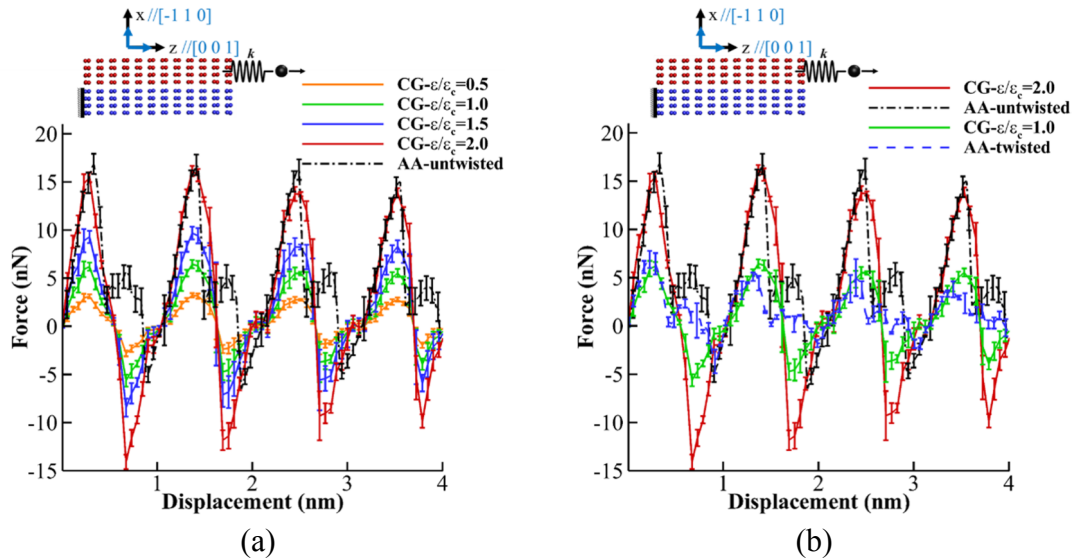


Figure 8.2 Force-displacement curves for shear tests from AA and CG modeling are shown in red and black color respectively (a) Shear test. (b) Small staggered structure.

Table 8.1 represents the maximum force (F_u), shear strength (τ_u) and shear modulus (G) of CG model with different values of ϵ/ϵ_c and AA model (twisted and untwisted) obtained from Figure 8.2a, b. We used stress-force and stress-strain relationships ($\tau_u = F_u/A$ and $G = \tau/\gamma$) to obtain τ_u and G from Figure 8.2a, b, respectively, where A is the shear area ($2.5\text{nm} \times 12.5\text{nm}$) and $\gamma = d/h$ is shear strain (d is displacement and $h = 0.85\text{nm}$ is the distance between two CNCs). The results shows that AA-twisted has a good agreements in terms of G (13%) and τ_u (12%) with CG model when $\epsilon/\epsilon_c = 1$ as shown in Figure 8.2b. In addition, AA-untwisted and CG model with $\epsilon/\epsilon_c = 2$ are matched in terms of G (7%) and τ_u (7%). Comparing the values of G for different ϵ/ϵ_c (Tab. 2) and G for individual CNC from previous studies, (Qin et al., 2017; Shishehbor et al., 2018; Sinko and Keten, 2015) indicates

that the value of G for shear between two CNCs is equal to G for individual CNC ($G=2.1\pm 0.42$ GPa) when $\epsilon/\epsilon_c = 2$.

Table 8.1 Mechanical Properties from shear test

| (ϵ/ϵ_c) | $F_u(\text{nN})$ | $\tau_u(\text{GPa})$ | $G(\text{GPa})$ |
|-------------------------|------------------|----------------------|-----------------|
| CG | | | |
| 0.5 | 3.1 ± 0.3 | 0.10 ± 0.010 | 0.42 ± 0.06 |
| 1.0 | 5.8 ± 0.5 | 0.18 ± 0.016 | 0.83 ± 0.10 |
| 1.5 | 9.5 ± 0.8 | 0.30 ± 0.025 | 1.25 ± 0.18 |
| 2.0 | 15.3 ± 0.7 | 0.49 ± 0.022 | 2.1 ± 0.42 |
| AA | | | |
| twisted | 6.7 ± 0.75 | 0.22 ± 0.024 | 1.04 ± 0.10 |
| untwisted | 16.5 ± 1.0 | 0.53 ± 0.03 | 1.71 ± 0.26 |

8.3 Tensile test of a small staggered structure

The small staggered structure is a more complex case study because not only there are more particles involved, but also a combination of mechanical properties of individual CNC, surface tension on (0 0 1) plane and shear among multiple particles are involved. For the tensile test the boundary atoms on the right hand side are being pulled by SMD while the boundary atoms on the left hand side are fixed (as shown in the cartoon of Figure 8.3a, b). In order to evaluate the effect of twisted/untwisted CNC on the results, two different setups similar to the shear test (as explained in sec. 2.4.2) are used. The comparison of the force-displacement curves from AA-untwisted and CG with different interfacial properties (i.e., $\epsilon/\epsilon_c = 0.5$, $\epsilon/\epsilon_c = 1$, $\epsilon/\epsilon_c = 1.5$ and $\epsilon/\epsilon_c = 2.0$) shows that for the AA-untwisted, CG model fits the best with $\epsilon/\epsilon_c = 2.0$. The force-displacement curves from AA model for tensile test of staggered structure with twisted and untwisted CNC particles are shown in

Figure 8.3b and compared with CG models with different interfacial properties (i.e., $\epsilon/\epsilon_c = 1$ and $\epsilon/\epsilon_c = 2$).

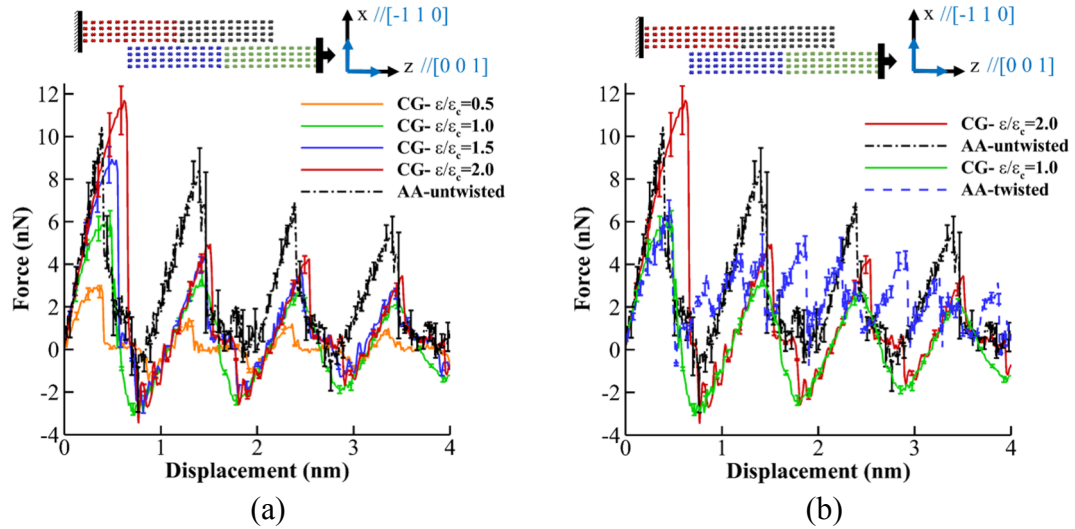


Figure 8.3 Force-displacement curves for tensile test of Small staggered structure from AA and CG modeling (a) Small staggered structure. (b) Small staggered structure.

Table 8.2 represents F_u , tensile strength (σ_u) and Young's modulus (E) of CG model with different values of ϵ/ϵ_c and AA model (twisted and untwisted) obtained from Figure 8.3a, b. We used stress-force and stress-strain relationships ($\sigma_u = F_u/A$ and $E = \sigma/\epsilon$) to obtain σ_u and E from Figure 8.3a, b. respectively, where A is the normal area ($2.4\text{nm} \times 2.5\text{nm}$) and $\epsilon = d/L$ is tensile strain (d is displacement and $L \cong 2 \times 12.5 \cong 25.0\text{ nm}$ is the initial length of two CNCs). The results indicate that AA-twisted have good agreements in terms of E ($\cong 5\%$ error) and σ_u ($\cong 15\%$ error) with CG model when $\epsilon/\epsilon_c = 1$ (Figure 8.3b). In addition, the CG model with $\epsilon/\epsilon_c = 2.0$ shows to be good fit in terms of E ($\cong 2\%$ error) and σ_u ($\cong 10\%$ error) for AA-untwisted as shown in Figure 8.3b. Although the frequency of the AA-

untwisted and CG model is the same, for the AA-twisted there is less definite frequency because of more complex microstructure.

Table 8.2 Mechanical Properties of staggered structure

| (ϵ/ϵ_c) | $F_u(\text{nN})$ | $\sigma_u(\text{GPa})$ | $E(\text{GPa})$ |
|-------------------------|------------------|------------------------|-----------------|
| CG | | | |
| 0.5 | 2.95 ± 0.3 | 0.45 ± 0.04 | 33.8 ± 5.4 |
| 1.0 | 6.0 ± 0.5 | 0.92 ± 0.07 | 59.0 ± 7.2 |
| 1.5 | 9.0 ± 1.0 | 1.38 ± 0.15 | 71.8 ± 8.6 |
| 2.0 | 11.5 ± 1.5 | 1.76 ± 0.23 | 69 ± 11.5 |
| AA | | | |
| twisted | 6.73 ± 1.0 | 1.03 ± 0.15 | 43.0 ± 7.1 |
| untwisted | 10.5 ± 1.5 | 1.6 ± 0.23 | 72 ± 15 |

8.4 Complementary Mechanical Tests

As discussed in chapter 7, the mechanical properties of the individual CNC are described through bonds b1-b5, as shown in Figure 7.2, and the mechanical performance of CG was compared with AA in section 7.3 (as shown in Figure 7.3). In addition in section. 8.2, the effect of interfacial properties of the CG model on the shear behavior between two CNCs, as shown in Figure 8.2, and the tensile test of the small staggered structure, Figure 8.3, was evaluated respectively. In this section we compare the mechanical behavior of two CNC particles with different interface properties, from our CG model, with mechanical properties of individual CNC, from AA and CG simulations, to find out the relationship between the mechanical behavior of two CNCs, separated by the interface, and one

individual CNC for different interfacial properties. This helps to evaluate how strong an interface property between two CNCs should be in order to observe failure in an individual CNC rather than the interface. Two different tensile tests are performed in $[-1\ 1\ 0]$ and $[0\ 0\ 1]$ directions when two CNC particles are interacting through $(-1\ 1\ 0)$ interface as shown in the cartoon of Figure 8.4a and Figure 8.4b respectively.

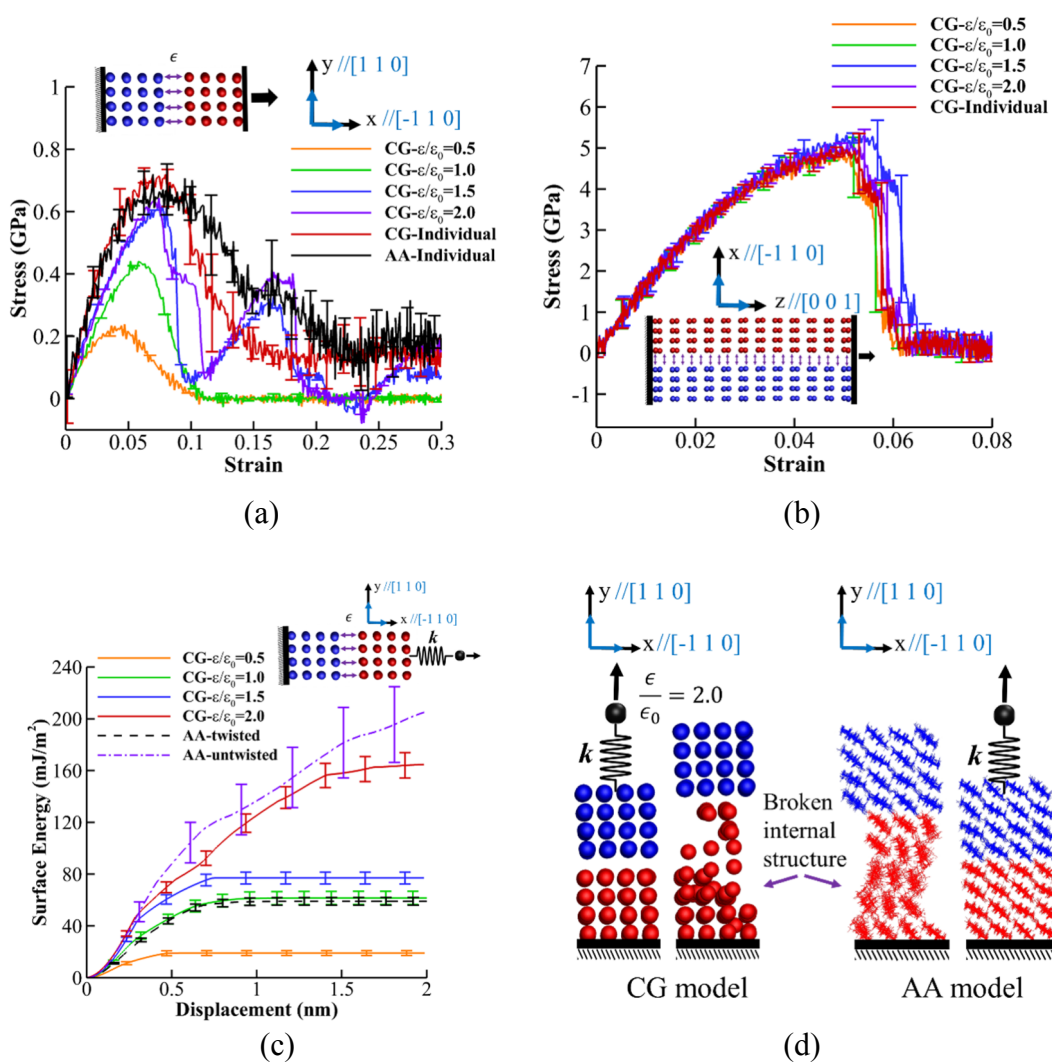


Figure 8.4 Comparing the CG parameters for twisted and untwisted interfaces. (a) Stress-strain curves for lateral tensile test (b) Stress-strain curves for longitudinal tensile test.

8.5 Assembly of Small CNC Bundle

Although our CG model was developed according to mechanical and interfacial properties; and did not consider any conformational analysis for interaction of CNC particles, here we examine the validity of our model for the conformation of a CNC bundle. To do so, a 2x2 bundle of short CNC particles with 12.5 nm length is first equilibrated for 2 ns and then the position of atoms are sampled every 10 ps for the next 3 ns duration. To compare the CG and AA models, the twist of the whole CNC bundle, the twist of the individual CNC particle inside the bundle and the radial distribution function, $g(r)$, are compared. Fig. A2a displays the twist per length, κ (*degree/nm*), of a 2x2 CNC bundle for 3 ns from AA and CG simulations. The cartoon in the Fig.A2a shows the definition of twisting angle, θ , as the angle between normal vectors obtained from cross product $AC \times AB$ and $CD \times CA$, where A, B, C and D are middle beads (in order to exclude twist of individual particle) in the cross-section of two diagonal CNC particles (the green and orange particles). The results indicate a comparable κ value of 0.6 and 0.4 (*degree/nm*) for AA and CG models respectively. In addition to the twist of a bundle, the κ for individual CNC particle in a bundle, obtained from AA and CG, is compared in Figure 8.5b. The definition of twisting angle, θ , is similar to the twist of a bundle; except that the A, B, C and D beads are in the corner of one particle, as opposed to the middle of two particles, as shown in the cartoon

in Figure 8.5b. The κ of individual CNC in a bundle for both CG and AA is around 0.6 (degree/nm). Comparing the κ of the bundle, 0.6 and 0.4 for CG and AA respectively, and the individual particle, 0.6 for both CG and AA, shows that the conformation of the CG model is more homogenous (forming a super molecule) than the AA simulation (Figure 8.5d). The reason could be the fact that the structure of the AA model is more complex (different atoms and interaction at the surface) than the CG model; which makes it more difficult for AA model to form a super-molecule as homogenous as CG model. Finally, the radial distribution function, $g(r)$, for 30 Å distance from CG and AA simulations is compared in Figure 8.5c. To calculate the $g(r)$, the bead and the average position of α -carbon for two consecutive glucose units are considered for the CG and the AA model respectively. As shown in Figure 8.5c, the $g(r)$ curve from CG is similar to the AA target, especially the CG model can accurately model the pair distances where peaks and valleys occur. However, the structure of the CG model shows more twist than the AA one (The twist per length, κ , is 0.6 and 0.4 (degree/nm) for CG and AA respectively).

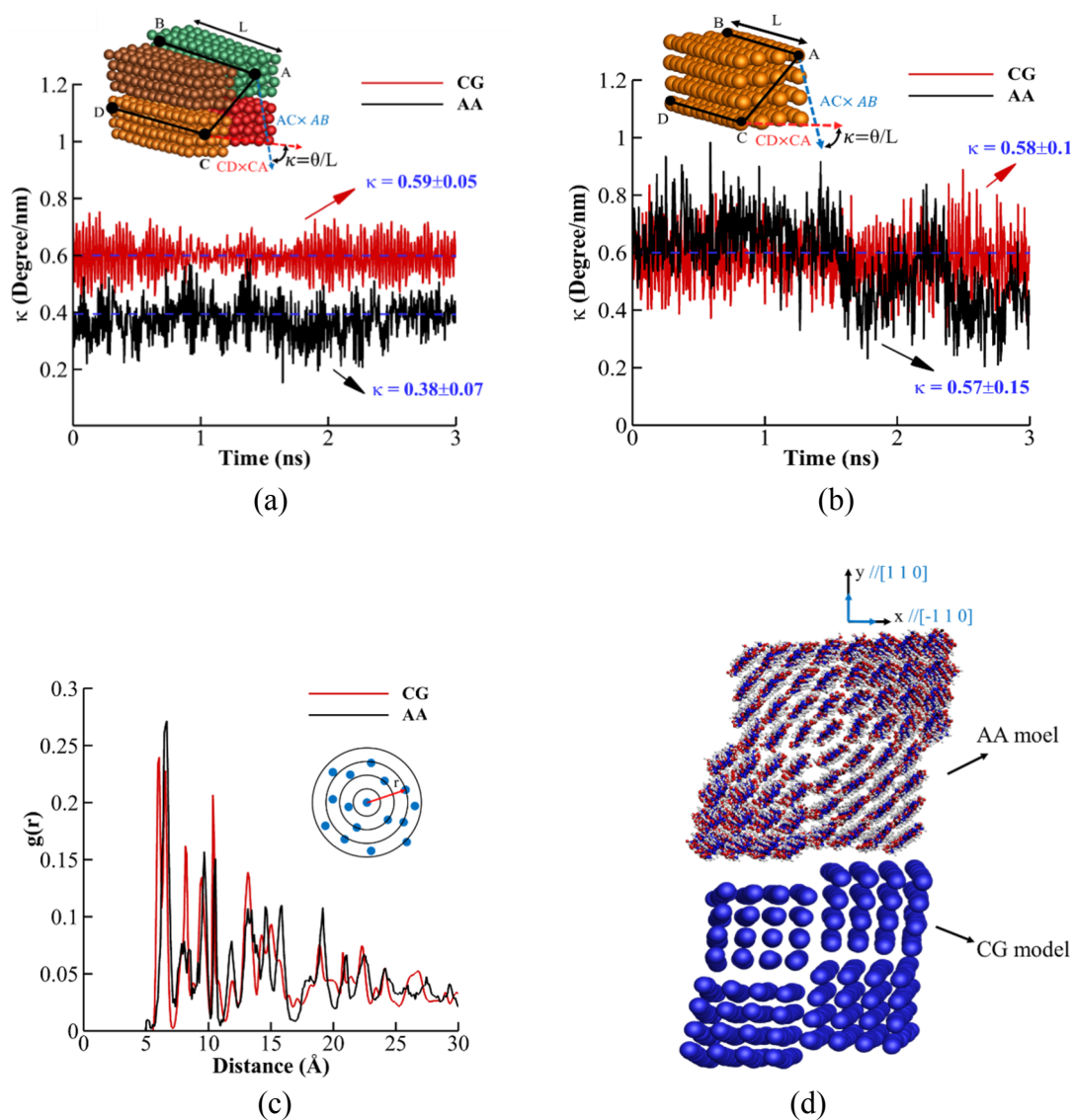


Figure 8.5 Conformational analysis of a 2x2 bundle of CNC by AA and CG modeling (a) curvature-time curves shows the change of twist per length for a bundle. (b) curvature-time curves shows the change of twist per length for an individual CNC inside a bundle. (c) Radial Pair distribution function for 30 Å. (d) The twisted structure of the bundle from AA and CG models are shown.

CHAPTER 9. THE EFFECT OF INTERFACE ON THE MECHANICAL PROPERTIES

(A version of this chapter is under review for publication)

CNCs can naturally assemble into different microstructural arrangement such as brick-and-mortar (staggered) and helicoidal structure.(Natarajan and Gilman, 2018; Qin et al., 2017) Understanding the structure-property relationship for different microstructural arrangement of CNCs could paves the way for designing better CNC based materials. Staggered arrangement of fibers observed in many biological materials such as nacre, bone, teeth and abalone shell, have been shown to increase stiffness, strength and toughness regardless of their brittle mineral constituent.(Barthelat, 2014; Barthelat et al., 2013; Espinosa et al., 2009; Gao, 2006; Li et al., 2004) There are many factors involved in the overall performance of a staggered structure such as (1) interfacial properties (2) mechanical properties of the fiber and (3) the overlap length of fibers.(Qin et al., 2017) For a staggered structure, it has been shown by many researchers that 50% overlap length maximizes the mechanical properties such as elasticity and strength.(Qin et al., 2017; Wei et al., 2012) Recently, a bead-spring model for CNC was used to show the effect of overlap length and interfacial properties on the strength, elasticity and toughness of staggered structure of CNC.(Qin et al., 2017) They show that increasing the overlap length (at 75 nm) leads to fracture of covalent bond and brittle failure of staggered CNC film.(Qin et al., 2017) In addition, by increasing the interfacial properties, brittle failure occurs at smaller overlap length.(Qin et al., 2017) Helicoidal arrangement of fiber layers (Bouligand),

observed in many biological materials such as crustacean shells,(Raabe et al., 2005) bone,(Rho et al., 1998) and mantis shrimp dactyle club,(Weaver et al., 2012) provides isotropic materials with high mechanical performance such as strength and toughness through different toughening mechanism.(Launey et al., 2010; Weaver et al., 2012; Yaraghi et al., 2016) As suggested by studies, in Bouligand structure, the cracks are forced to follow helicoidal paths and therefore, maximizes energy dissipation through allowing multiple crack growth from various nucleation locations without coalescing.(Natarajan and Gilman, 2018; Suksangpanya et al., 2017) Although many successful attempts for fabrication of Bouligand composites at microscale have been reported,(Cheng et al., 2011; Grunenfelder et al., 2014; Yang et al., 2017) at nanoscale, manufacturing process remains challenging.(Natarajan and Gilman, 2018) The fact that CNCs can naturally assembled into bouligand structure in addition to their excellent mechanical properties, have made them promising nanoparticle for bioinspired Bouligand composite.(Natarajan and Gilman, 2018) In this section, we apply the developed CG model to study the mechanical properties of the CNC assemblies. In particular, we are interested in analyzing the effect of surface energy on the (1) fracture of a bundle of CNC through bending test. (2) tensile test of a staggered structure of CNC and (3) tensile test of a staggered Bouligand structure of CNC are studied. In all the CG simulations, CNC particles with diagonal shape, 36 chains, 4.5 nm width, and 100 nm length have been employed (representing CG model of Figure 7.2a). In all case studies, the system is minimized using the hftn algorithm, temperature is controlled by the Nosé-Hoover thermostat at 300 Kelvin and system is equilibrated for 5 ns in a NVT ensemble.

9.1 Fracture of A CNC Bundle

In this section, the bending load is applied to a 4x4 bundle of CNC particles through cylindrical indenter. Each CNC particle has 100 nm length, 4 nm width and 36 chains (length and width of wood CNCs). The size of the bundle, 4x4, is selected based on our observation of a negligible twisting (0.02 degree/nm) for cross sections equal and larger than 4x4 CNCs. After 10 ns equilibration of the structure, the load is applied in the y direction through the cylindrical indenter with 16 nm radius, which is placed in the middle of the bundle in z direction and moving with constant velocity of 1 m/s (schematic in Figure 9.1a). The indenter is moved in the y direction until it entirely passes through the thickness of the bundle; and the boundary atoms on two side of the beam are fixed (clamped) in order to prevent the bundle from slipping. The same simulation steps are repeated for different surface energy, by changing the ϵ , and the force-displacement curves are plotted as shown in Figure 9.1a. This is done to understand the effect of surface energy on the mechanical properties. Comparing the force-displacement curves for different values of ϵ/ϵ_c shows two different trends, (1) bending failure for $\epsilon/\epsilon_c = 0.5$ and $\epsilon/\epsilon_c = 1.0$ and (2) shear failure for $\epsilon/\epsilon_c = 1.5$ and $\epsilon/\epsilon_c = 2.0$. For example for $\epsilon/\epsilon_c = 1$ (green line), from point a to b $\cong 3.0$ nm, the loading is in the elastic region and after that the plastic deformation occurs by breaking the covalent bonds in the top CNC (point b to c in Figure 9.1a). From point c to point d, the rest of the CNCs exhibit resistance to bending and therefore the increase in force is observed. At point d, the maximum load is reached by breaking all the covalent

bonds in the middle of the beam. After point e, the indenter is passing through the thickness and the small increase in load is due to resistance of covalent bonds at the boundary to further bending. For the elastic region (point a to b in Figure 9.1a). The results indicate that the effect of surface energy on elasticity maximizes as we approach to $\epsilon/\epsilon_c = 1$, and there is no significant change in elasticity by increasing the surface energy after certain value. In addition to elastic modulus, by changing the surface energy, we observed fracture at different places of the bundle. For example, for $\epsilon/\epsilon_c = 0.5$ (red curve in Figure 9.1a), failure starts in the middle of bundle by breaking top two CNCs and afterwards, the beam undergoes big deflection which leads to failure of last two CNCs at the boundaries (Figure 9.1b). Further increase in the bending, after rupture (point e), leads to shearing and sliding of CNCs which is seen as sawtooth curve (Figure 9.1a). For $\epsilon/\epsilon_c = 1.0$ (green curve in Figure 9.1a), failure starts in the middle of bundle by breaking top two CNCs and continues in the same place until rupture (Figure 9.1c). For $\epsilon/\epsilon_c = 1.5$ and $\epsilon/\epsilon_c = 2.0$, (blue and black curves in Figure 9.1a respectively), plastic deformation and rupture occurs at the boundaries as opposed to the middle and therefore less bending deformation is observed.

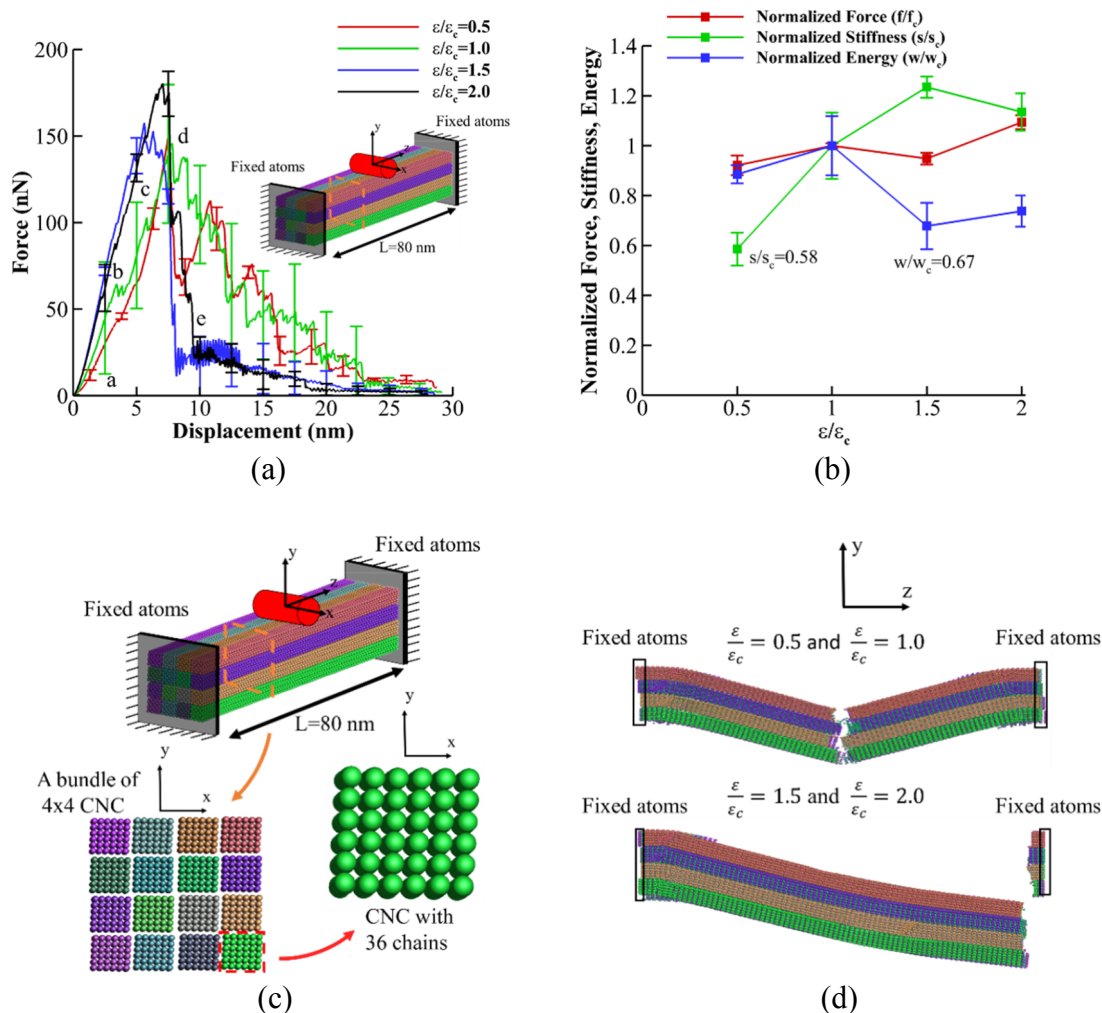


Figure 9.1 Nano-indentation of a bundle of CNC (4x4) with 100 nm length (a) Force-displacement curve for different interface properties. (b) Comparing the normalized maximum force, stiffness and fracture energy for different interface properties. The values are normalized with respect to their values at $\epsilon_c = 5.0$. (c) Different fracture mechanism for different interfacial strength.

9.2 Mechanical Properties of A Staggered Structure

Here we use CNCs with 100 nm length and 50% overlap length to study the effect of interfacial properties (twisted and untwisted interfaces) on the performance of the

staggered structure under tensile test. The properties of the interface in our CG model are changed through changing VdW depth parameter, e.g., ϵ_c and the stress-strain curves obtained from tensile test are shown in Figure 9.2a. The normalized strength, elastic modulus and toughness with respect to their values at $\epsilon_c = 5.0$ ($\epsilon/\epsilon_c = 1.0$) are plotted as a function of interfacial properties in Figure 9.2b. The results, as shown in Figure 9.2b, indicates that increasing the ϵ/ϵ_c increases the strength (from 0.9 GPa to 1.7 GPa) and elastic modulus (from 140 GPa to 200 GPa). Although toughness initially increases from 22 Mj/m^3 at $\epsilon/\epsilon_c = 0.5$ to maximum value of 81 Mj/m^3 at $\epsilon/\epsilon_c = 1.0$, it decreases dramatically to 9 Mj/m^3 (90% decrease) for $\epsilon/\epsilon_c = 1.5$ and $\epsilon/\epsilon_c = 2.0$. The fractured structures for different values of ϵ/ϵ_c reveals that the fracture happens by localized slipping of few fibers for weak interfaces ($\epsilon/\epsilon_c = 0.5$), nonlocal slipping of many fibers for twisted CNC interface ($\epsilon/\epsilon_c = 1$) and finally covalent bond breaking (brittle failure) for strong untwisted CNC interface ($\epsilon/\epsilon_c = 2.0$) as shown by Figure 9.2c. This behavior can also be observed through elastic-plastic and brittle behavior of stress-strain curves for $\epsilon/\epsilon_c = 1$ and $\epsilon/\epsilon_c = 2$ for twisted and untwisted interfaces respectively. In addition, the reason that after $\epsilon/\epsilon_c = 1.5$ strength saturates to 1.7 GPa and toughness drops to 9 Mj/m^3 (90% decrease), as shown in Figure 9.2b, can be explained by covalent bond breaking which leads to brittle failure. The results indicate that optimum mechanical performance (high strength, elasticity and toughness) can be achieved through weaker twisted interface ($\epsilon/\epsilon_c = 1$) through nonlocal fiber pull out.

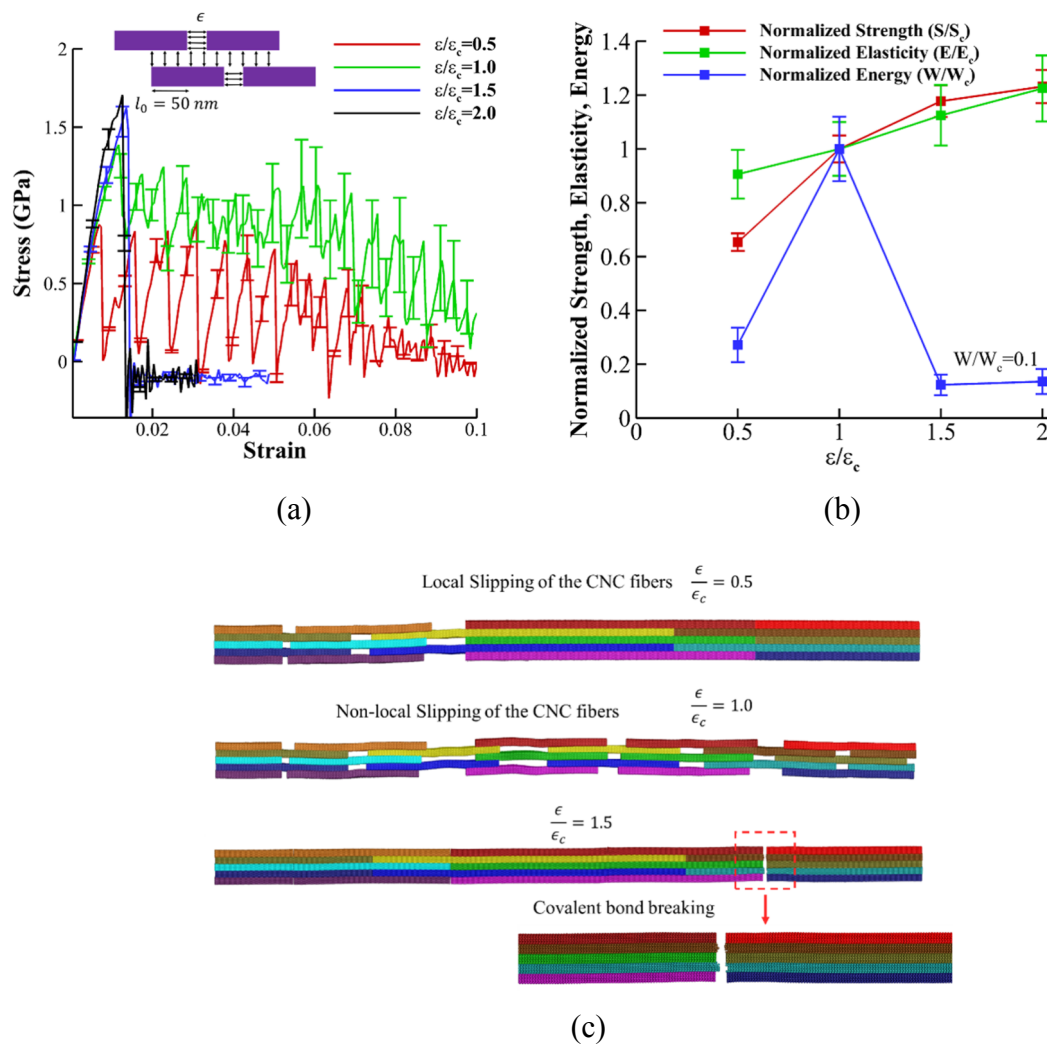


Figure 9.2 Stress-Strain curves for staggered structure with different interface strength (a) stress-strain curve. (b) Comparing the normalized strength, elasticity and fracture energy for different interface properties. The values are normalized with respect to their values at $\epsilon_c = 5.0$. (c) Different fracture mechanism for different interfacial strength.

9.3 Mechanical Properties of A Bouligand Structure

Here, we examine the effect of interfacial properties on the mechanical performance of staggered Bouligand CNC. The Bouligand structure we study here is 6 layers of twisted

staggered CNCs with 50 nm overlap length and pitch angle of 30 degree (from bottom to top layers, fibers have 0° , 30° , 60° , 90° , 120° and 150° orientations with respect to z direction as shown in the schematic of Figure 9.3a and the movement of atoms in the x direction is fixed during the equilibration to keep the orientation of CNCs intact). The properties of the interface in our CG model are changed through changing VdW depth parameter, e.g., ϵ_c and the stress-strain curves obtained from tensile test are shown in Figure 9.3a. In order to compare the variation in mechanical performance as a function of interfacial properties; strength, elastic modulus and toughness are normalized with respect to their values at $\epsilon_c = 5.0$ ($\epsilon/\epsilon_c = 1.0$) and plotted in Figure 9.3b. The results, as shown in Figure 9.3b, indicates that increasing the ϵ/ϵ_c increases the strength (from 0.3 GPa to 0.7 GPa) and elastic modulus (from 41 GPa to 55 GPa); however their values saturates after the $\epsilon/\epsilon_c = 1.5$ to 0.7 GPa and 55 GPa respectively. The toughness increases from 17 Mj/m^3 at $\epsilon/\epsilon_c = 0.5$ and peaks at $\epsilon/\epsilon_c = 1.0$ to 50 Mj/m^3 and then decreases to 25 Mj/m^3 (50% decrease) for $\epsilon/\epsilon_c = 1.5$ and $\epsilon/\epsilon_c = 2.0$. The final fractured structures for different ϵ/ϵ_c , shown in Figure 9.3c, also reveals that for weak interfaces ($\epsilon/\epsilon_c = 0.5$), failure happens before fibers are fully pulled out (less than 50% of the overlap length) while for twisted CNC interface ($\epsilon/\epsilon_c = 1$) fibers pull out occurs over the entire overlap length before failure. For stronger interfaces ($\epsilon/\epsilon_c = 1.5$ and $\epsilon/\epsilon_c = 2.0$) which is associated with untwisted interface, the failure happened due to covalent bond breaking and results in saturation in strength and decrease in toughness as discussed above .

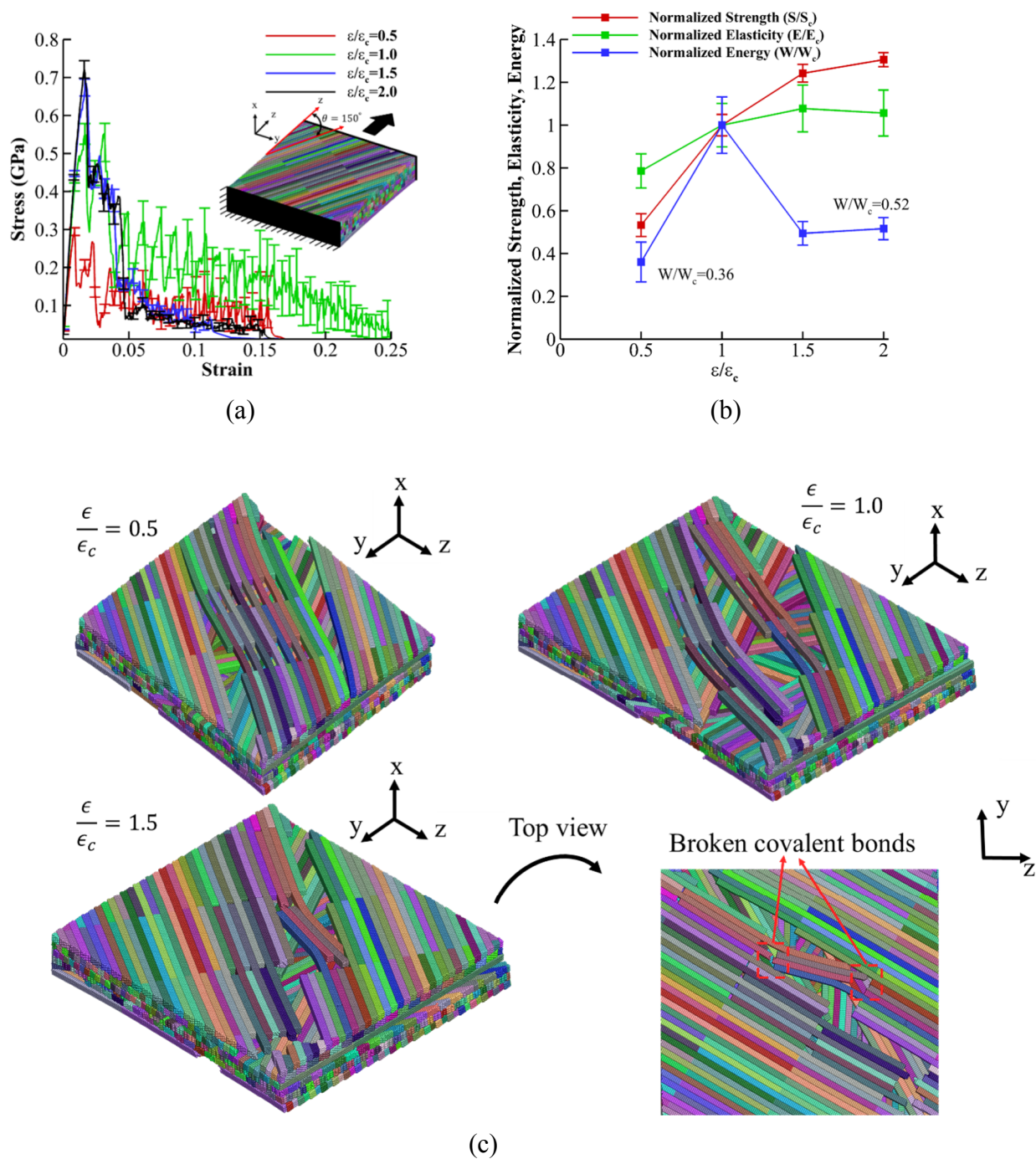


Figure 9.3 Stress-Strain curves for Bouligand structure with different interface strength (a) stress-strain curve. (b) Comparing the normalized strength, elasticity and fracture energy

for different interface properties. The values are normalized with respect to their values at $\epsilon_c = 5.0$. (c) Different fracture mechanism for different interfacial strength.

9.4 Summary and Conclusion

In this work, we presented a new CG model of CNC that is able to replicate mechanical and interfacial features obtained from experiments and/or AA MD simulations. The CG bead size in our model can predict the stick-slip behaviors observed in AA simulations with the same frequency. The model can capture Elastic modulus, strength and failure strain of CNC particle in all three perpendicular directions. Another main feature of the model is tunable interfacial properties, without affecting the mechanical properties of the individual CNC particle, for weaker (misaligned or twisted interface) or stronger (functionalized CNC) interface than the actual perfect CNC-CNC interface. We employed this capability to study the effect of interface properties on (1) bending and fracture of a CNC bundle and (2) bio-inspired staggered (brick-and-mortar) structure of CNC with 50% overlap length and (3) Staggered Bouligand structure of CNC. For CNC bundle, the results indicate that increasing interfacial properties leads to increase in elasticity and decrease in toughness with no significant differences in maximum force (the optimum properties happen at $\epsilon/\epsilon_c = 1$ which is the interfacial properties of the twisted CNCs). In the brick-and-mortar structure, by increasing the interfacial properties different failure mechanism is observed; e.g., localized slipping of few fibers for weak interfaces ($\epsilon/\epsilon_c = 0.5$), nonlocal slipping of many fibers for twisted CNC interface ($\epsilon/\epsilon_c = 1$) and finally brittle failure for untwisted CNC interface ($\epsilon/\epsilon_c = 2$) due to covalent bond breaking. The Bouligand structure shows similar trend in strength, elasticity and toughness. However,

while for staggered structure the decrease in toughness at $\epsilon/\epsilon_c = 1.5$ due to covalent bond breaking is 90% (brittle failure), for Bouligand structure toughness decreases to 50% (controlled failure) which shows the capacity of Bouligand structure to prevent localized cracking and catastrophic failure as shown by previous studies (Natarajan and Gilman, 2018; Suksangpanya et al., 2017). By taking into account the overall mechanical performance, including strength, elasticity and toughness, the results indicate that twisted CNC/CNC interface ($\epsilon/\epsilon_c = 1$) demonstrates a better mechanical performance than untwisted perfect CNC/CNC interface ($\epsilon/\epsilon_c = 2$). Although, in this paper, we only used our CG model for few applications, the model can be used or extended to model more variety of engineering applications. For example, the model can be used for different CNC sizes (different width and length) or shapes (diamond, rectangular or hexagonal) as suggested by experiments to model an RVE of CNC particles with a distribution of length and width. Furthermore, as the properties of the interface in our CG model is tunable, without affecting properties of the individual CNC particle, the model can be combined with a CG model for a polymer of interest to shed light on the mechanical properties of CNC-polymer nanocomposites. Finally, although our model was not developed for self-assembly of CNCs, our conformational results on a bundle of CNCs are promising for potential self-assembly application in the future.

CHAPTER 10. THE EFFECT OF FIBER LENGTH AND ORIENTATION

(A version of this chapter is under review for publication)

10.1 Introduction

As the most abundant organic material on earth, cellulose has been used as an engineering material for thousands of years for paper/packaging, textiles, and forest products. Recently, a new class of cellulose based particles, cellulose nanocrystal (CNC) gained much attention as a promising candidate for sustainable engineering materials due to their exceptional mechanical properties (Klemm et al., 2011, 2005; Moon et al., 2011) (Klemm et al., 2011, 2005; Luo et al., 2017; Moon et al., 2011), biocompatibility (Moon et al., 2011), abundance (Moon et al., 2011) and low production cost (Wang et al., 2015). CNCs are rod-shaped nanoparticles with a high aspect ratio (AR~50-500 nm long and AR~5-20 nm width) that can be chemically extracted from cellulose based sources such as plants, tress, bacteria, etc. through sulphuric-acid hydrolysis (Chowdhury et al., 2017; Habibi et al., 2010; Moon et al., 2011). Although most studies on CNCs are concentrated on CNC-polymer composites (Chen et al., 2014; Lee et al., 2014; Luo et al., 2017; Potulski et al., 2014), recently, researchers are investigating on the properties of neat CNC materials (all-CNCs) (Natarajan et al., 2018; Natarajan and Gilman, 2018; Reising et al., 2012). For a neat CNC film, many features could influence the overall mechanical properties such as (1) mechanical properties of the individual CNC, (2) the interfacial properties between two

CNCs, (3) microstructural design of CNCs and (4) CNC length and orientation distribution (Moon et al., 2011). Mechanical properties of individual CNCs have been reported experimentally (Moon et al., 2011; Pakzad et al., 2012; Wagner et al., 2016) and numerically (Chen et al., 2016; Dri et al., 2013; Shishehbor et al., 2018; Wu et al., 2014, 2013) by many researchers, showing anisotropic behavior due to different chemical bonds in different directions (Dri et al., 2013; Shishehbor et al., 2018). For example, DFT calculations on the elastic properties of the CNCs shows much higher elastic modulus (E) in the axial direction ($\sim 200\text{GPa}$ in the covalent bond direction) than in the transverse direction ($\sim 20\text{GPa}$ in hydrogen bond (h-bond) and van der Waals directions(vdW)) (Dri et al., 2013). Similarly, anisotropy in strength (σ_f) of CNC has also been reported showing values of 5-7 GPa and 0.5-1.0 GPa in axial and transverse directions respectively (Wu et al., 2014). The properties of the interface between CNCs in both tangential and normal directions have also been studied numerically (Sinko and Keten, 2015) and analytically (Q. Meng et al., 2017) recently. For example, Meng et al, developed shear and normal cohesive laws for CNC interface based on h-bond potential to study the fracture toughness of cellulose nanopaper and showed linear correlation between toughening and interfacial strength (Q. Meng et al., 2017). In addition, Sinko and Keten proposed analytical model for stick-slip behavior observed in shear between two CNCs (Sinko and Keten, 2015). Many recent studies considered bioinspired microstructural design, such as binary blends of short and long CNCs (Natarajan et al., 2018), brick-and-mortar (Qin et al., 2017; Zhu et al., 2015) and Bouligand structure (Natarajan and Gilman, 2018; Shishehbor and Zavattieri, 2019) of CNCs to improve the mechanical properties of neat CNC materials. In particular,

the effect of surface energy on the mechanical performance in tension test of brick-and-mortar (Qin et al., 2017) and Bouligand (Shishehbor and Zavattieri, 2019) structure of CNC showed different failure mechanism. Studies on the correlation between the alignment of Cellulose nanofibers (CNFs) and the mechanical performance shows that aligned nanofibers improves E and σ_f in the alignment direction (Håkansson et al., 2014; Reising et al., 2012; Sehaqui et al., 2012; Wang et al., 2015, 2018, 2017, Zhu et al., 2014, 2017). For example, Reising et al, fabricated shear-based casting neat CNC films with different degree of alignment (Reisingf et al., 2012). They used Hermans order parameter (S) for characterizing CNC alignment along the shear direction and showed that E scales with S (E is 15 and 30 GPa for S 0.04 and 0.53 respectively). In the recent effort to fabricate anisotropic transparent film with aligned CNFs, σ_f for an anisotropic film was shown to be 3 times (~ 350 MPa) more than the isotropic one (~ 125 MPa), while the σ_f in the transverse direction was ~ 23 MPa (Zhu et al., 2017). Increasing the alignment of nanofibrillated cellulose (TEMPO-NFC) by cold drawing suggested a linear relationship between draw-ratio and elastic modulus (10 and 33 GPa for draw ratio 1 ($S=0.34$) and 1.6 ($S=0.72$) respectively) (Sehaqui et al., 2012). The effect of CNC length on the mechanical properties of CNC nanopaper has also been studied through coarse-graining (CG) (Qin et al., 2017) and analytical models (Q. Meng et al., 2017). Meng et al, showed a linear correlation between toughening and length for long CNCs ($\sim \mu m$) (Q. Meng et al., 2017). The CG modeling of CNC nanopaper revealed that increasing the length of CNCs to ~ 100 nm leads to covalent bond breaking and brittle failure (Qin et al., 2017). However,

in all case studies, all the CNCs in the microstructure were assumed to have the same length (Dirac delta function) and no particular length distribution was considered. In most experiments, however, we have a distribution of fibers length and width instead, that could influence the mechanical properties of the material (Fu et al., 2008; Graupner et al., 2016). In this chapter, we use our previously developed CG model for CNCs (Shishehbor and Zavattieri, 2019) to investigate on the effect of CNCs alignment, length and interfacial properties on the mechanical performance of the neat CNC materials.

10.2 Method

In this section, the generation of the representative volume element (RVE) of CNCs, fiber length and orientation distribution and tuning different interfacial properties for CNC-CNC interface are discussed. Comprehensive information about the CG model we use in this paper can be found in our previous work (Shishehbor and Zavattieri, 2019). In order to obtain the mechanical properties (such as elastic modulus, strength, failure strain and work to fracture) of the RVEs of interest, tensile test is performed using steered molecular dynamics (SMD). In all the simulations, the MD package LAMMPS (Plimpton, 2007) is used and the system is first minimized and then equilibrated in the NVT ensemble at $T=0$ K (molecular mechanics (MM)) for 5 ns before performing tensile test. To understand the anisotropic mechanical behavior of samples, the mechanical tests are performed in two perpendicular directions (i.e., in the aligned and perpendicular to the aligned directions). For stretching in each direction, SMD is applied at the strain rate of $1 \times 10^{-5} \text{ ps}^{-1}$ to the boundary beads (20 nm thickness from the boundary) while the movement of the opposite

boundary beads (20 nm thickness from the opposite boundary) is kept fixed. To study the effect of length (orientation) distribution on the mechanical properties; different RVEs are generated by changing the parameters associated with the length (orientation) of CNCs, while the orientation (length) distribution is kept constant. The influence of interfacial properties on the results are studied through changing van der Waals (vdW) depth parameter, e.g., ϵ_c of the model (Shishehbor and Zavattieri, 2019), while keeping the other microstructural properties intact.

10.2.1 Mechanical properties of the rotated film

In our previous chapters, we developed a new CG model of CNC that is able to replicate mechanical and interfacial features obtained from experiments and/or ALL-atom (AA) MD simulations (Shishehbor and Zavattieri, 2019). The CG bead size in our model can predict the stick-slip behaviors observed in AA simulations with the same frequency (Shishehbor and Zavattieri, 2019). The model can capture Elastic modulus, strength and failure strain of CNC particle in all three perpendicular directions. Another main feature of the model is tunable interfacial properties, without affecting the mechanical properties of the individual CNC particle, for weaker, stronger interface than the actual perfect CNC-CNC interface.

10.2.2 Generation of 3D RVE

For a neat CNC material, generating RVEs with a relatively high CNCs volume fraction is crucial, especially for CNCs with higher aspect ratio ($AR \geq 20$), the task could be very challenging. Having CNCs with a distribution of length and width (as opposed to constant size for length and width), however, not only provides more realistic RVEs for experiments,

but also increases the volume fraction. Here, for all the RVE, we assume the width of the CNCs have a normal distribution with mean value of 4.5 nm ($\mu_w = 4.5 \text{ nm}$) and variance of 1.5 nm ($\sigma_w = 1.5 \text{ nm}$). The length and orientation of CNCs also have normal

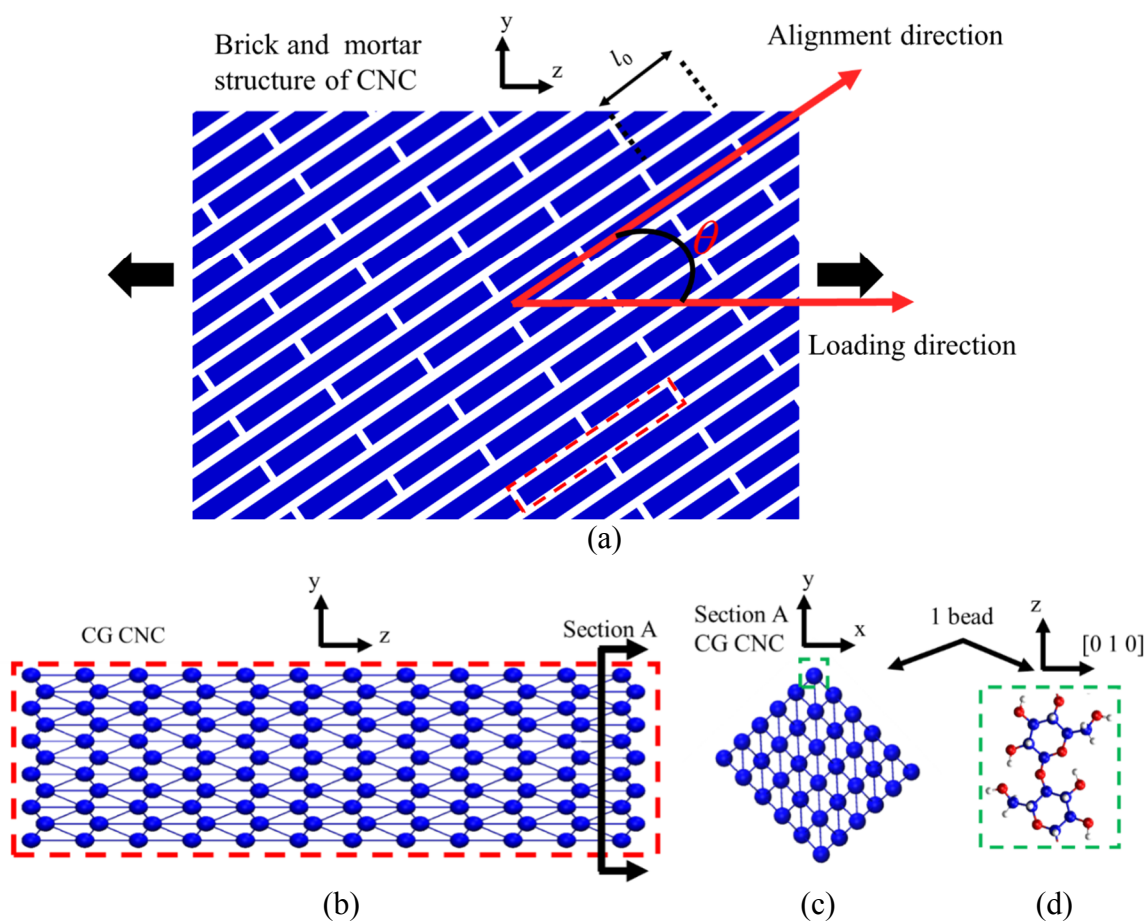


Figure 10.1. (a) ‘Brick and mortar’ structure of CNC with 50% overlap length. The overlap length is shown with l_0 and the red dashed rectangle shows the building block (CNC) of the structure (b) Side view of the CG model for CNC (c) Cross section of the CG model for CNC. (d) Molecular structure of disaccharide representing 1 bead in our CG model.

distribution, but the values for the mean (μ_L and μ_θ for length and orientation respectively) and variance (σ_L and σ_θ for length and orientation respectively) are different for each RVE

and are the parameters of this study. For RVE generation, first, a shelf of many CNCs with the desired length and orientation distribution is generated and then passed to the PackMol program (Martinez et al., 2009) for packing. The size of the box is 3 times the μ_L and the minimum distance between particles is set to 1.0 nm to avoid any CNC-CNC repulsion in the molecular dynamic (MD) simulations (the equilibrium distance between two beads in the CG model is 0.9 nm). Figure 10.2a shows a generated RVE of CNCs for $\mu_L = 20 \text{ nm}$, $\sigma_L = 3.25 \text{ nm}$ with a relatively high degree of alignment in z direction ($s=0.9$). The CG representation of one particle in the RVE is shown in Figure 10.2b with green spheres representing 1 bead in our CG model. Each bead represents 1 disaccharide in the chemical structure of CNC as shown in Figure 10.2c.

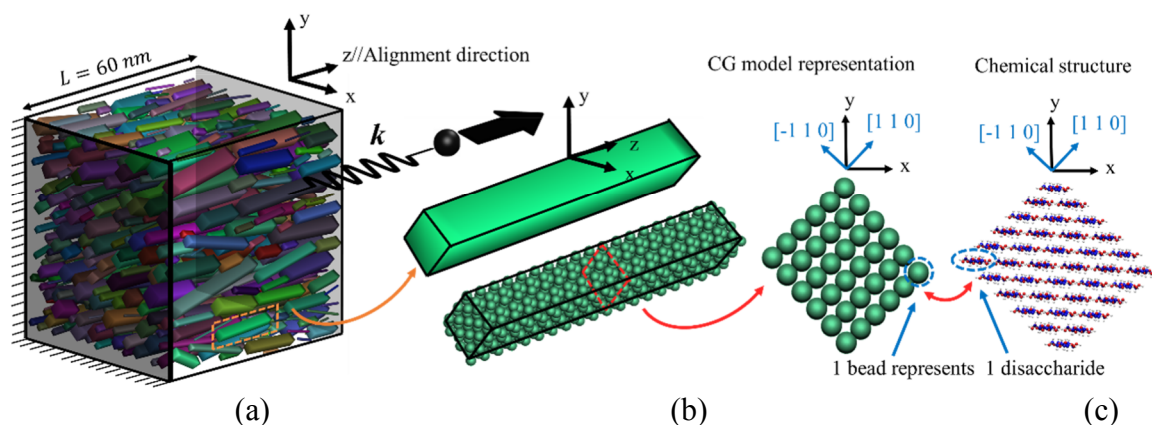


Figure 10.2. Representation of the model. (a) CNC particles with different length, width and alignment are shown with random colors in a RVE under tensile test. (b) CG representation of the CNCs are shown with green beads. (c) Chemical representation of the CNC cross-section.

10.2.3 Fiber orientation distribution (FOD)

A desired FOD function for CNCs should be able to distinguish between a highly aligned (unidirectional) and randomly distributed microstructures through variation of its parameters. Since in this study, the degree of alignment of CNCs is measured with respect to a specific direction (alignment direction); normal distribution function seems to be a good candidate to describe FOD as follow:

$$f(x|\mu_\theta, \sigma_\theta) = \frac{1}{\sigma_\theta\sqrt{2\pi}} e^{-\frac{(x-\mu_\theta)^2}{2\sigma_\theta^2}} \quad (10.1)$$

Where μ_θ is the mean value and σ_θ is the variance. The dispersion of CNCs around the aligned direction ($\mu_\theta = 0$) can be changed through changing σ_θ . Since in most experiments, the degree of fibers alignment are characterized by X-ray diffraction and Hermans order parameter (S); we also describe the generated RVE with S through the following equation (Chowdhury et al., 2017):

$$S = \frac{3\langle \cos^2 \gamma \rangle - 1}{2} \quad (10.2)$$

$$\langle \cos^2 \gamma \rangle = 1 - 2 \langle \cos^2 \varphi \rangle$$

$$\langle \cos^2 \varphi \rangle = \frac{\int I(\varphi) \cos^2 \varphi \sin \varphi d\varphi}{\int I(\varphi) \sin \varphi d\varphi}$$

To evaluate the effect of FOD on the mechanical properties, 6 different RVEs with $\sigma_\theta = 10, 20, 30, 40$ and 60 degree corresponding to $S=0.9, 0.7, 0.45, 0.26, 0.13$ and 0.05

respectively. To exclude the effect of other parameters in the microstructure and make sure that S is the only variable of the study; constant FLD is taken for all the RVEs ($\mu_L = 20$ nm and $\sigma_L = 6.25$ nm). Figure 10.3 demonstrates two different FOD with $\mu_\theta = 0$ degree and $\sigma_\theta = 10$ and 60 degree for $S=0.9$ and $S=0.05$ respectively.

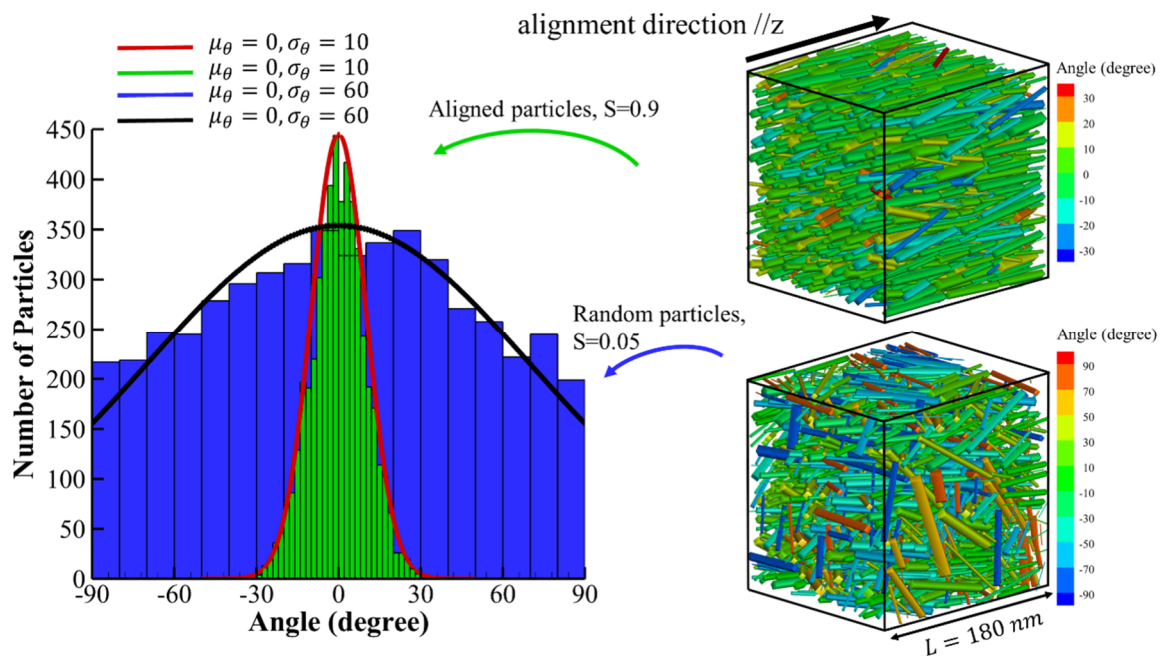


Figure 10.3. Two RVEs with two different fiber orientation distribution around the shear direction has been shown. The Herman's parameter (S) for the RVEs with aligned and random particles are 0.9 and 0.05 respectively.

10.2.4 Fiber length distribution (FLD)

We assume that CNCs length distribution is based on normal distribution function as follow:

$$f(x|\mu_L, \sigma_L) = \frac{1}{\sigma_L \sqrt{2\pi}} e^{-\frac{(x-\mu_L)^2}{2\sigma_L^2}} \quad (10.3)$$

Where μ_L is the mean value and σ_L is the variance. To evaluate the effect of FLD on the mechanical properties, 4 different RVEs with $\mu_L = 20, 40, 60$ and 80 nm and $\sigma_L = 6.25, 12.5, 18.75$ and 25 nm respectively. The values for the σ_L is scaled with the values of μ_L for each RVE in order to have a wider range of size distribution. During RVE generation, the minimum length for CNCs is limited to 10 nm to make sure the length of CNCs is not smaller than the width ($AR \geq 1$). To exclude other microstructural parameters and make sure that only the effect of FLD is considered, similar FOD is used for all the generated RVEs. We use two distinct FODs, representing highly aligned ($S=0.9$) and randomly distributed ($S=0.05$) CNCs, for each set of RVEs with different FLD to understand the influence of CNCs alignment on the results obtained for FLD. Figure 10.4 illustrates two FLDs with $\mu_L = 20$ and 60 nm and $\sigma_L = 6.25$ and 18.75 nm and the corresponding RVEs.

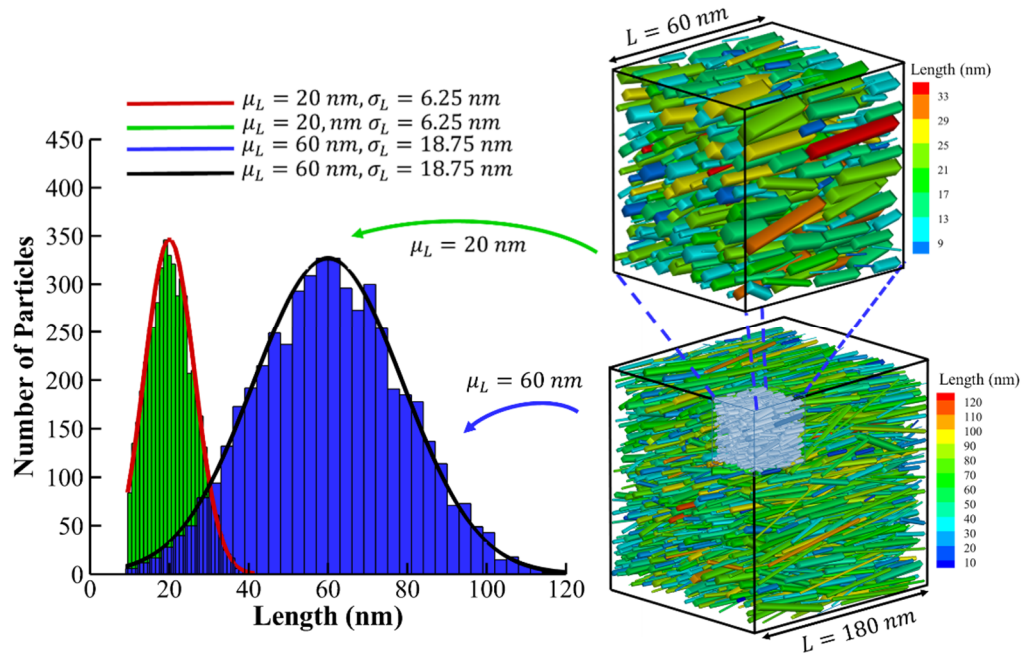


Figure 10.4. Two different FLDs with μ_L 20 and 60 nm and the corresponding RVEs have been shown.

10.2.5 The Effect of Interfacial Properties

The interfacial properties between two CNCs in our model is defined by Lennard-Jones (LJ) potential function which only needs two parameters for modeling vdW dispersion (Shishehbor and Zavattieri, 2019):

$$E_{vdW}(r) = 4\varepsilon \left[\left(\frac{\sigma}{r} \right)^{12} - \left(\frac{\sigma}{r} \right)^6 \right] \quad (10.4)$$

$$F_{vdW}(r) = 4\varepsilon/r \left[12 \left(\frac{\sigma}{r} \right)^{12} - 6 \left(\frac{\sigma}{r} \right)^6 \right] \quad (10.5)$$

Where ϵ is the energy of the potential at equilibrium, minimum energy, σ is the distance parameters and r is the distance between two beads. The interfacial energy and force displacement for different interfacial energy are shown in Figure 10.5a and Figure 10.5b respectively.

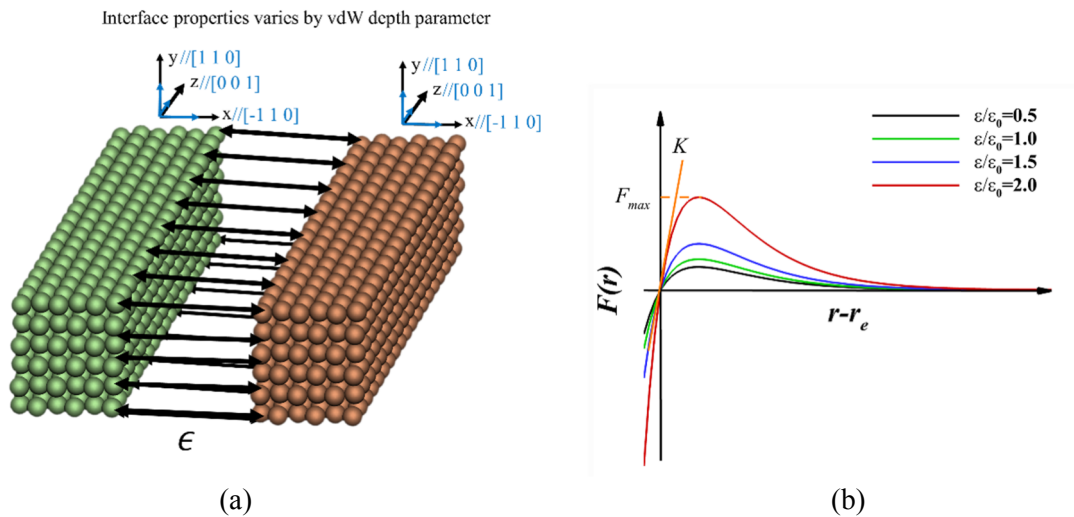


Figure 10.5. Properties of the interface between two CNCs can be varied by changing depth parameter, ϵ , of the LJ potential. (a) The interaction between two CNCs are defined. (b) The force-displacement curves for different depth parameters. The maximum force, F_{max} , and stiffness, K , varies by changing the ϵ .

To evaluate the effect of interfacial properties on the mechanical performance of aligned and randomly distributed CNCs, we use two distinct FODs, representing highly aligned ($S=0.9$) and randomly distributed ($S=0.05$) CNCs with specific FLD $\mu_L = 20$ and $\sigma_L = 6.25$ and 4 different interfacial properties ($\epsilon/\epsilon_0 = 0.5, 1.0, 1.5$ and 2.0).

10.3 Results and Discussion

10.3.1 Mechanical Properties of The Rotated Film

The elastic modulus and strength of the rotated staggered structure for rotational angles (θ in Figure 10.1a) of 0° , 15° , 30° , 45° , 60° , 75° and 90° are obtained through stress-strain curves by performing tensile test in the z direction (Figure 10.1a). In all simulations, the particles length are 50 nm ($l_0 = 25 \text{ nm}$), $\epsilon/\epsilon_0 = 1.0$ and the average value and error bar for elastic modulus and strength are obtained from 3 samples with different initial configurations. The variation of elastic modulus with respect to θ from CG modeling and the error bar associated with it are shown with solid red line and blue shape respectively in Figure 10.6a. The results show that by increasing the angle from 0° to 45° , the elastic modulus linear decrease from 125 GPa to 12 GPa (decreasing 38 GPa by every 15° increase). However, the value of elastic modulus for 45° , 60° , 75° and 90° angles are almost in the same range of values ($12 \pm 6 \text{ GPa}$). In addition, analytical solution based on the rotation of the compliance matrix of a unidirectional lamina is shown with dashed red line in Figure 10.6a. The compliance matrix is formed by having the elastic modulus for 0° and 90° (125 GPa and 12 GPa respectively), shear modulus (2.5 GPa) and Poisson ratios in two different directions (0.2 for both direction). The value of shear modulus was obtained by performing shear test. Comparing the analytical and numerical results for elastic modulus shows 25%-50% difference for $\theta \leq 45^\circ$ and 20% difference for $\theta > 45^\circ$. Note

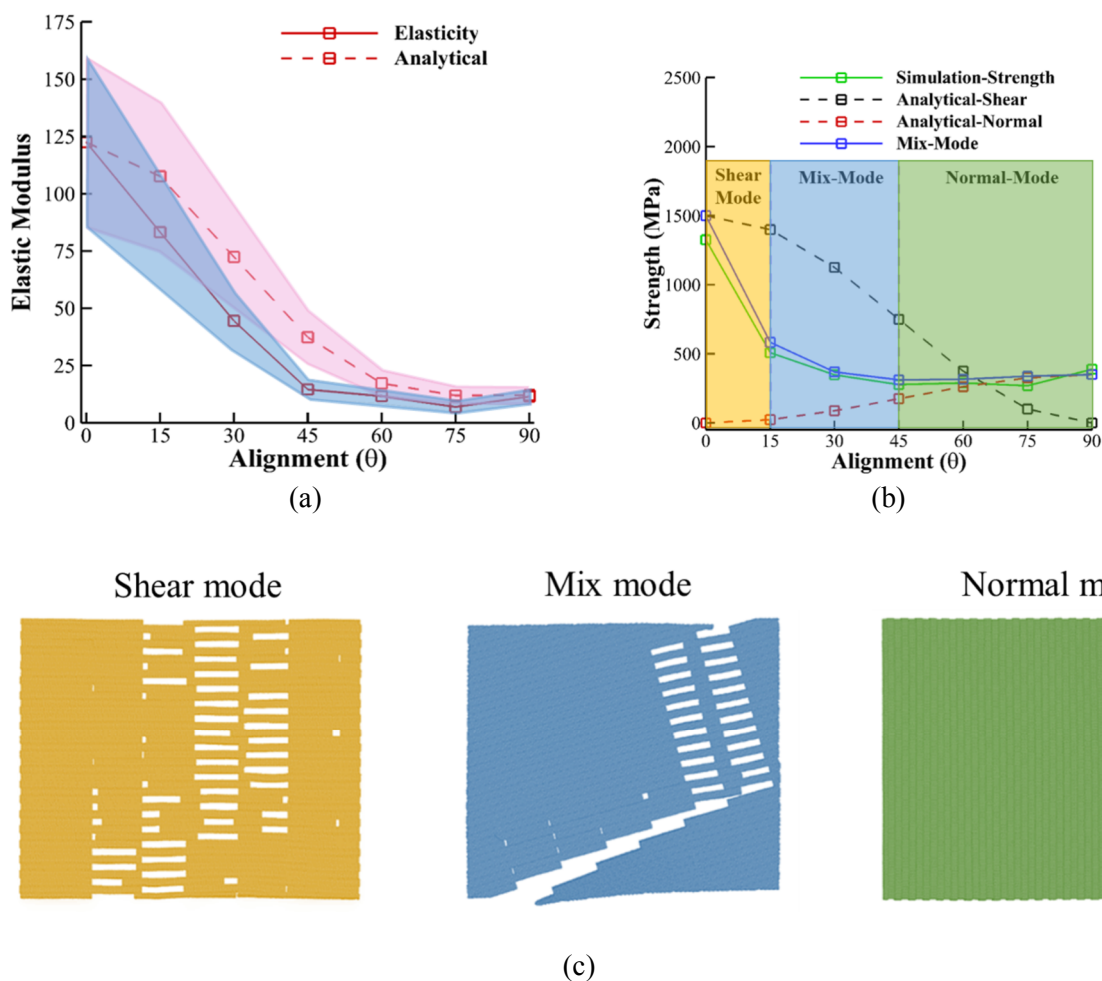


Figure 10.6. The effect of loading direction (θ) on the mechanical properties of a 2D staggered film. (a) Elastic modulus. (b) Strength. (c) failure modes for $\theta=0^\circ$, 45° and 90° .

that the analytical solution for laminas assumes the material to be homogenous solid, however, in the case of staggered CNCs with interfaces, separation and sliding of CNCs affects the elastic modulus. Figure 10.6b shows the values of strength versus θ from the simulations with green solid line. The results shows a sudden drop in strength from 1500 MPa at 0° to 600 MPa at 15° and then strength slowly decrease to 300 MPa at 45° . For $\theta \geq$

45°, there is no Significant change in strength values (300 ± 100 MPa). The failed rotated staggered structures for $\theta = 0^\circ$, 45° and 90° reveals 3 different failure mechanism dominated by shear between particles for $\theta = 0^\circ$, complete separation of particles for $\theta = 90^\circ$ and a mix mode of shear and separation of particles for $\theta = 45^\circ$ as shown in Figure 10.6c with shear model, normal mode and mix mode respectively. Based on our observations on the failed structures and their associated strength, the strength-alignment curve is divided in 3 regions associated with shear model ($0 \leq \theta \leq 15$), mix mode ($15 < \theta \leq 45$) and normal mode ($45 < \theta \leq 90$) shown with gold, blue and green regions in Figure 10.6b respectively.

The analytical formulas to obtain the elastic modulus of a lamina for different orientation (θ) for the staggered structure of CNC (Figure 10.7a). First, the compliance matrix of the structure is formed by having the elastic modulus for $\theta = 0$ (E_1) and $\theta = 90$ (E_2), shear modulus (G_{12}) and passion ratios (ν_{12} and ν_{21}) and using Eq. 10.6. The new compliance matrix for θ can be obtained by using transformation matrix and transformation relationship in equations Eq. 10.7 and Eq. 10.8 respectively.

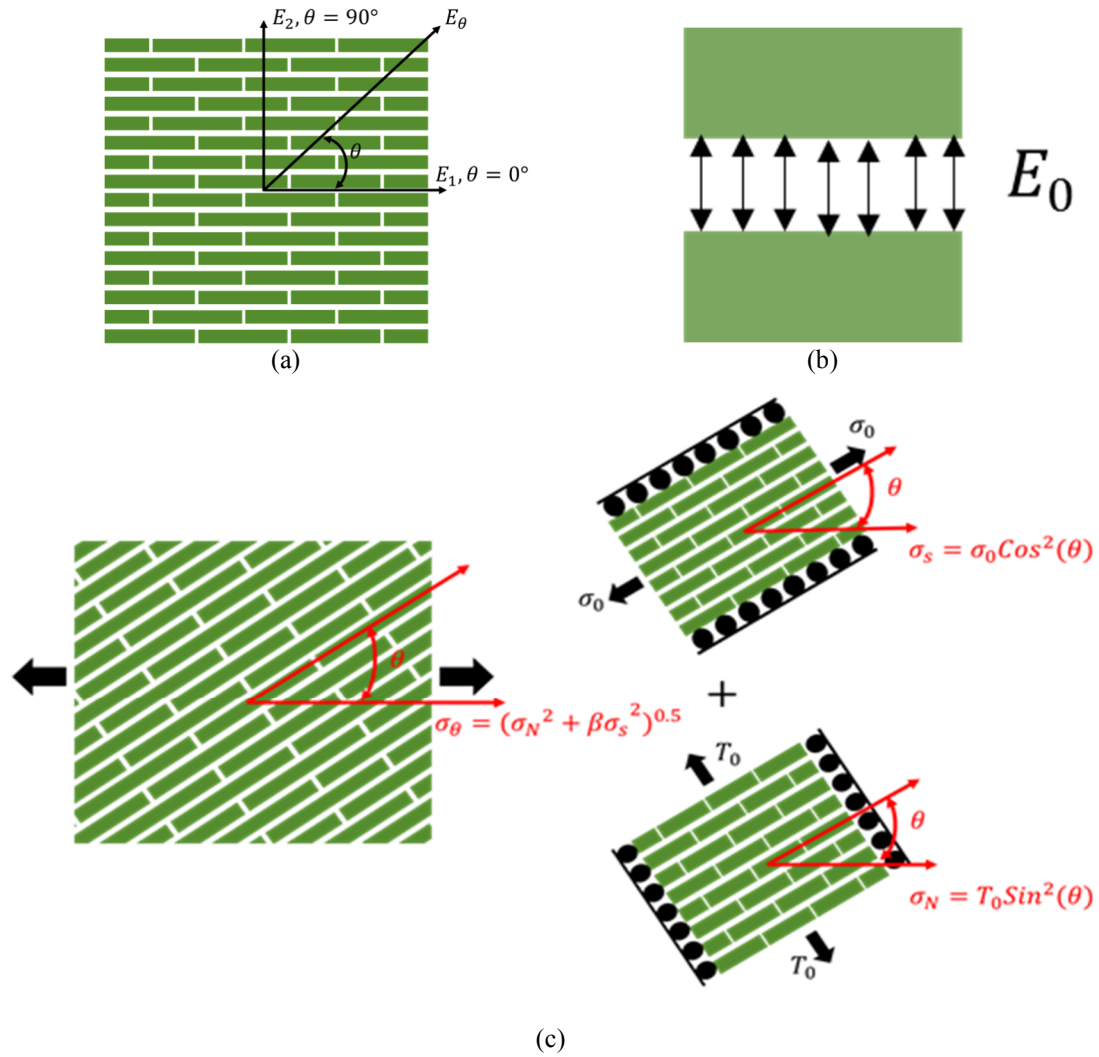


Figure 10.7. Analytical models for rotated staggered structure of CNC. (a) Main directions and the arbitrary rotation direction (θ). (b) Adhesion between particles. (c) Separation of a mix mode to shear and normal mode.

$$C = \begin{bmatrix} \frac{E_1}{1-\nu_{12}\nu_{21}} & \frac{\nu_{12}E_2}{1-\nu_{12}\nu_{21}} & 0 \\ \frac{\nu_{21}E_1}{1-\nu_{12}\nu_{21}} & \frac{E_2}{1-\nu_{12}\nu_{21}} & 0 \\ 0 & 0 & G_{12} \end{bmatrix} \quad (10.6)$$

$$T = \begin{bmatrix} \cos^2(\theta) & \sin^2(\theta) & 2\cos(\theta)\sin(\theta) \\ \sin^2(\theta) & \cos^2(\theta) & -2\cos(\theta)\sin(\theta) \\ -\cos(\theta)\sin(\theta) & \cos(\theta)\sin(\theta) & \cos^2(\theta) - \sin^2(\theta) \end{bmatrix} \quad (10.7)$$

$$\bar{C} = T^{-1}CT^{-T} \quad (10.8)$$

The analytical solution for the rotated shear mode, normal mode and a mix mode of failure for staggered structure of CNC as shown in Figure 10.7a. Here the shear mode is defined as the failure mechanism when during loading the particles slide and no separation of particles occur in the perpendicular direction ($\theta = 0$). The normal mode in this paper is defined when the failure mechanism is mainly separation of particles and sliding has not significant contribution in the strength ($\theta = 90$). A mix mode is a combination of sliding and separation of particles and both modes contribution to the strength of the structure. Figure 10.7c shows the assumptions of shear mode, normal mode and the mix mode. The rollers shown in the Figure 10.7c helps to have pure shear and normal mode during loading and are demonstrated to explain the analytical model.

The analytical solution based on rotated shear mode, rotated normal mode and rotated mix mode are shown in Figure 10.6b with black dashed line, blue solid line and red dashed line respectively. As shown in Figure 10.6b, the mix mode solution, which is a combination of

shear and normal mode formulas, can accurately predict the simulation results for regardless of θ (10% error).

10.3.2 The effect of FOD

The mechanical properties of neat CNC material verse S for axial and transverse direction are illustrated in Figure 10.8. The values of S changes from 0.05 for randomly distributed CNCs to 0.9 for highly aligned CNCs. The results for σ_f indicates that alignment of CNCs enhances and lowers the σ_f in axial and transverse direction respectively as shown in Figure 10.8a. However, improvement in σ_f is more significant for $S \geq 0.45$.

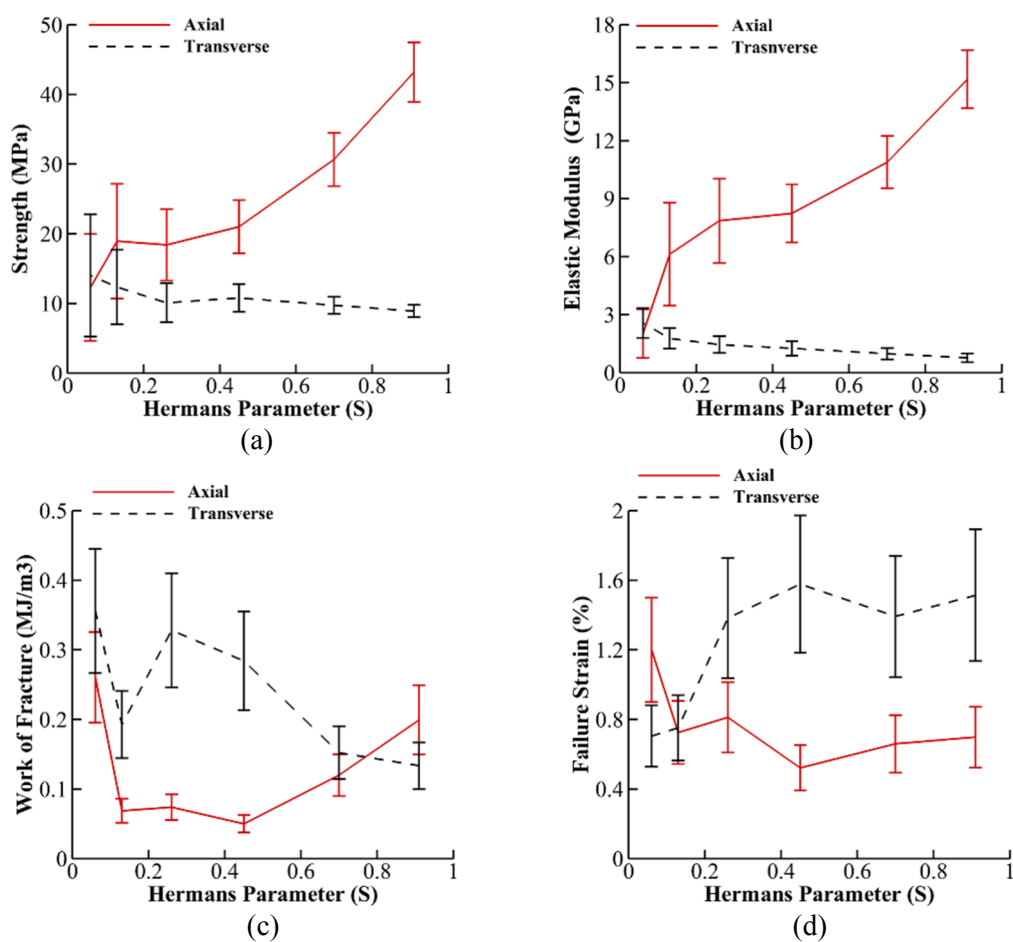


Figure 10.8. Mechanical properties of neat CNC material for different Hermans parameter (S) are shown in red solid line and dashed black line for axial (alignment direction) and transverse direction respectively. (a) Strength, (b) Elastic modulus, (c) Work of fracture, and (d) Failure strain.

10.3.3 The effect of FLD

The mechanical properties of neat CNC material versus the average length of particles (μ) for axial and transverse direction are illustrated in Figure 10.9. The values of μ changes from 20 nm for short to 80 nm for long CNCs. The results for σ_f indicates that increasing

μ of CNCs enhances and lowers the σ_f in axial and transverse direction respectively as shown in Figure 10.9a. However, improvement in σ_f is more significant $\mu = 40$ nm.

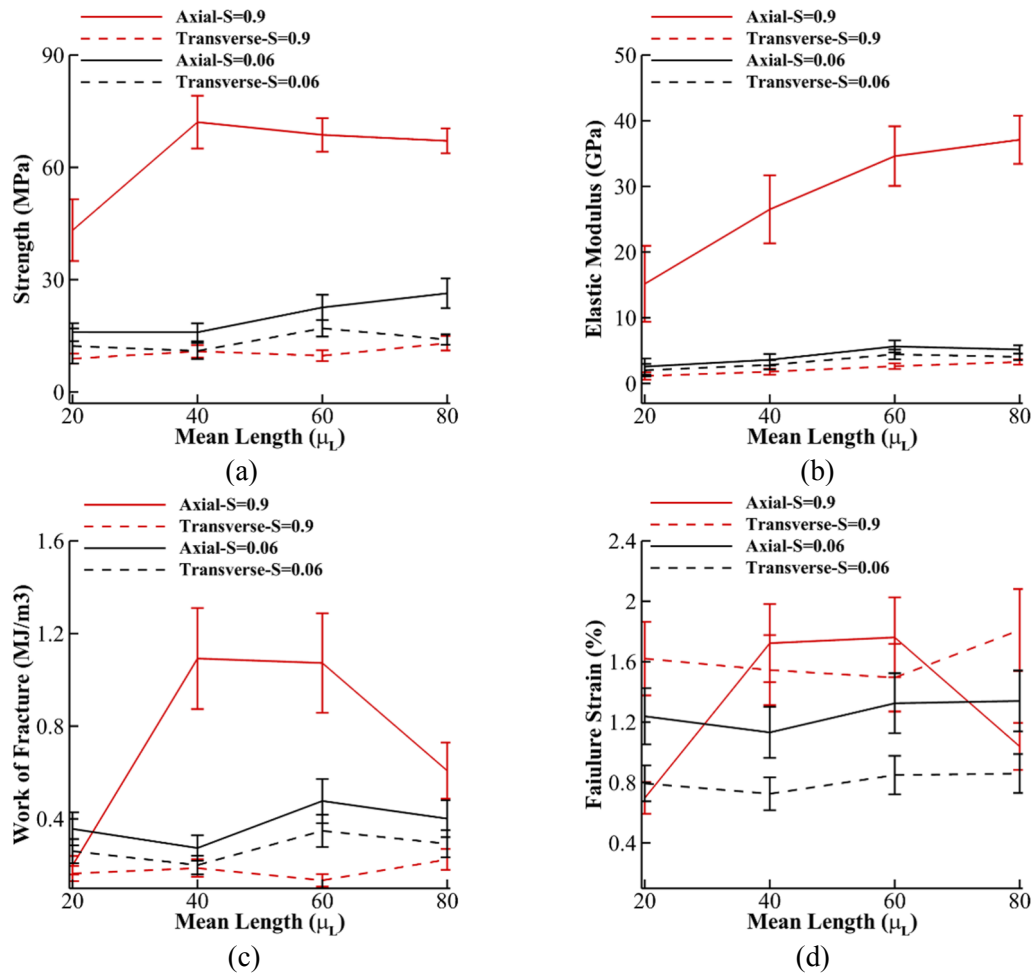


Figure 10.9. Mechanical properties of neat CNC material for different average length (μ) are shown in red solid line and dashed black line for axial and transverse direction respectively. (a) Strength, (b) Elastic modulus, (c) Work of fracture, and (d) Failure strain.

10.3.4 The effect of interfacial properties

The mechanical properties of neat CNC material verse $\varepsilon/\varepsilon_0$ for axial and transverse direction are illustrated in Figure 10.10. The values of S changes from 0.06 for randomly

distributed CNCs to 0.9 for highly aligned CNCs. The results for σ_f indicates that alignment of CNCs enhances and lowers the σ_f in axial and transverse direction respectively as shown in Figure 10.10a. However, improvement in σ_f is more significant for $S \geq 0.45$ and

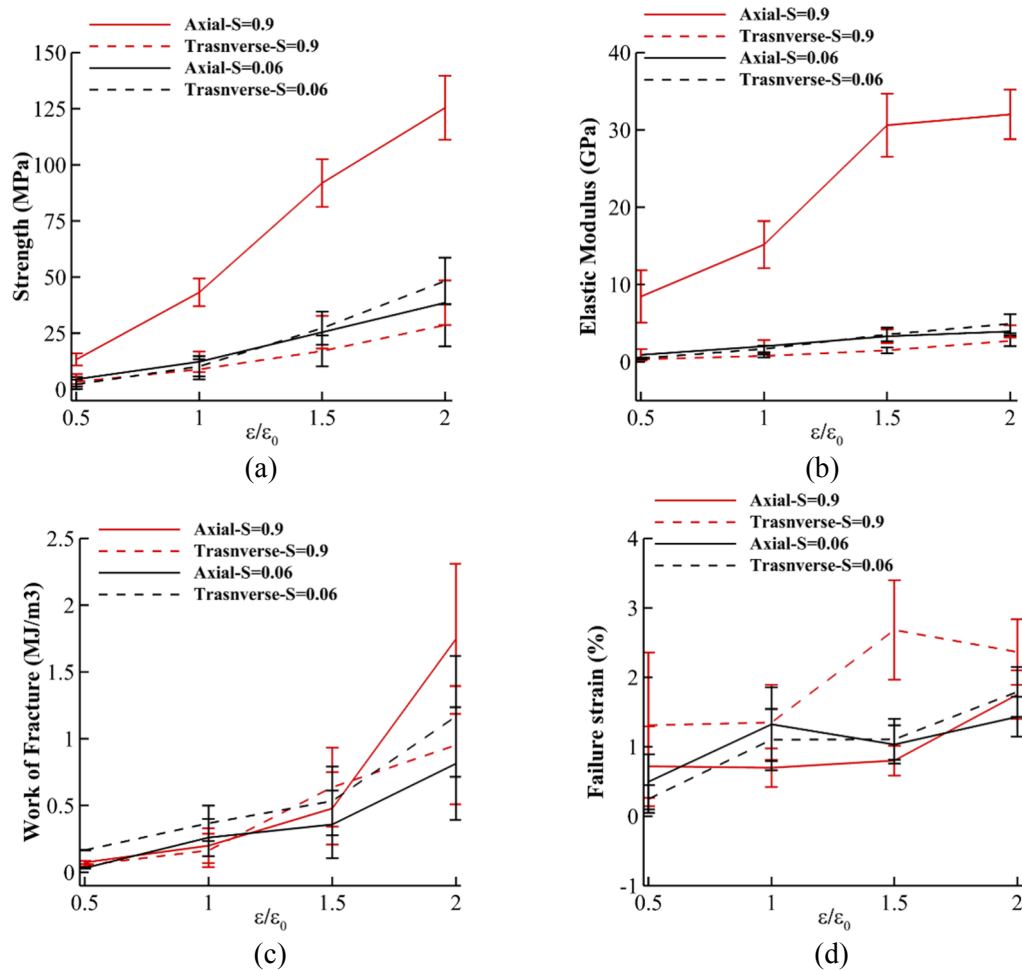


Figure 10.10. Mechanical properties of neat CNC material for different interfacial properties (ϵ/ϵ_0) are shown in red solid line and dashed black line for axial and transverse direction respectively. (a) Strength, (b) Elastic modulus, (c) Work of fracture, and (d) Failure strain.

CHAPTER 11. CONCLUSION

(A version of this chapter is published <https://doi.org/10.1016/j.jmps.2017.11.006>)

(A version of this chapter is under review for publication)

11.1 Summary and Conclusion

In summary, this work introduces a simplified continuum-based structural model (CM) that can be implemented under the finite element framework to capture the elastic response of CNC. This first elastic model, together with the analytical models, was shown to be very useful in predicting the different elastic properties and elucidating the main mechanisms that contribute to the overall stiffness of the CNC under various loading conditions. In addition, we presented a new CG model of CNC that is able to replicate mechanical and interfacial features obtained from experiments and/or AA MD simulations. The main feature of the new CG model is tunable interfacial properties for capturing weaker (misaligned or twisted interface) or stronger (functionalized CNC) interface than the actual perfect CNC-CNC interface, without affecting the mechanical properties of the individual CNC particle. We employed this capability to study the effect of interface properties on (1) bending and fracture of a CNC bundle and (2) bio-inspired staggered (brick-and-mortar) structure of CNC with 50% overlap length and (3) Staggered Bouligand structure of CNC. By taking into account the overall mechanical performance, including strength, elasticity and toughness, the results indicate that twisted CNC/CNC interface ($\epsilon/\epsilon_c = 1$) demonstrates a better mechanical performance than untwisted perfect CNC/CNC interface

($\epsilon/\epsilon_c = 2$). In addition, we employed the developed CG model for CNC particles to find the relationship between microstructural properties such as particle length distribution, particle orientation distribution and adhesion between particles; and mechanical properties such as elastic modulus and strength. First, elastic modulus, strength and failure mechanism of a 2D rotated staggered structure with constant particle length and width for $0 \leq \theta \leq 90$ under tensile loading were studied and compared with analytical solutions. The results demonstrated 3 different failure mechanism of shear model ($0 \leq \theta \leq 15$), mix mode ($15 < \theta \leq 45$) and normal mode ($45 < \theta \leq 90$) for strength. For elastic modulus, the results shows linear decrease (125 GPa to 12 GPa) in elastic modulus for $0 < \theta \leq 45$ and nearly constant values (12 ± 6 GPa) for $45 < \theta \leq 90$. To study a more realistic case studies and to understand the effect of fiber length and orientation distribution on the mechanical performance; various 3D microstructures representing different case studies were studied. For the effect of fiber orientation distribution, mechanical properties of 3D RVEs were obtained for different Herman's parameters.

11.2 Future Works

The continuum-structural model could be extended to capture the non-linear and inelastic behavior of CNC by considering debonding of the non-bonded elements. Future work will focus on developing cohesive zone type of models for the debonding between chains and even breakage of the covalent bonds. In addition, as a future work, the effect of temperature and environment (e.g., influence of water) on the mechanical properties of CNC can also

be incorporated to the proposed model. For example, almost all the studies on CNC in a water solvent confirmed that the interaction of CNC and water is mostly limited to the

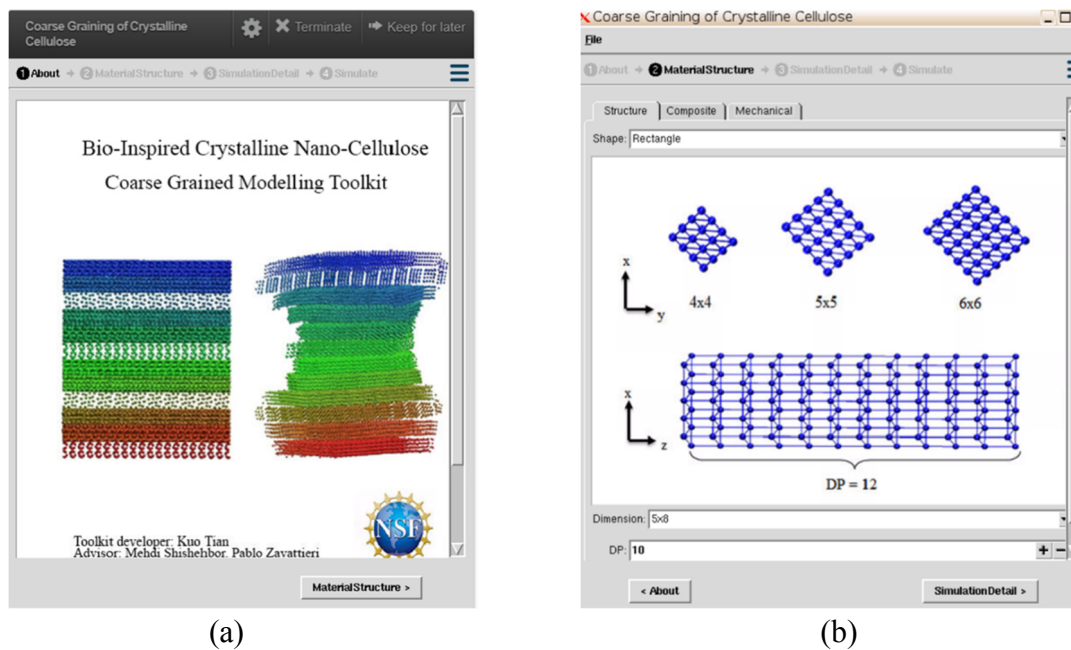
surface of the CNC and that water molecules could not get inside the CNC (Matthews et al., 2006; Lahiji et al., 2010).

Although, in this dissertation, we only used our CG model for few applications, the model can be used or extended to model more variety of engineering applications. For example, the model can be used for different CNC sizes (different width and length) or shapes (diamond, rectangular or hexagonal) as suggested by experiments to model an RVE of CNC particles with a distribution of length and width. Furthermore, as the properties of the interface in our CG model is tunable, without affecting properties of the individual CNC particle, the model can be combined with a CG model for a polymer of interest to shed light on the mechanical properties of CNC-polymer nanocomposites. Finally, although our model was not developed for self-assembly of CNCs, our conformational results on a bundle of CNCs are promising for potential self-assembly application in the future.

APPENDIX A. COARSE GRAINING OF CRYSTALLINE NANO-CELLULOSE

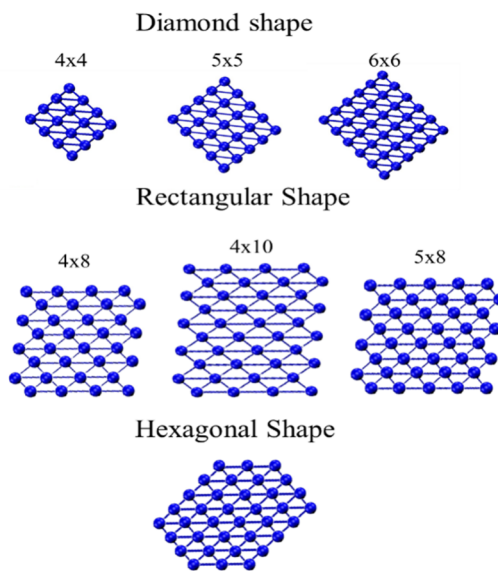
(A version of this chapter is supporting documents of [doi:10.4231/D3930NW4D](https://doi.org/10.4231/D3930NW4D))

Coarse graining of Crystalline Nano-Cellulose (Tian et al., 2016) is a Nanohub toolkit for simulation of bioinspired structures of cellulose nanocrystal (CNC). The versatility of the tool provides different cross-section type, i.e. diamond, rectangular and hexagonal shapes, and provides a user friendly key for choosing the length of the CNCs. For assembly of the structure, the tool offers two different options, (1) one is the staggered arrangement of the CNCs and (2) the second option is the Bouligand arrangement. For each arrangement, the user is able to decide on multiple structural options provided to personalize the microstructure. For example, for the Bouligand structure, the user is able to change the pitch angle between the layers to generate the desired microstructure. After defining the microstructure, In simulation detail tab, user can specify equilibration time, equilibrium temperature, direction that tensile displacement is applied, and the number of CPU cores to use .



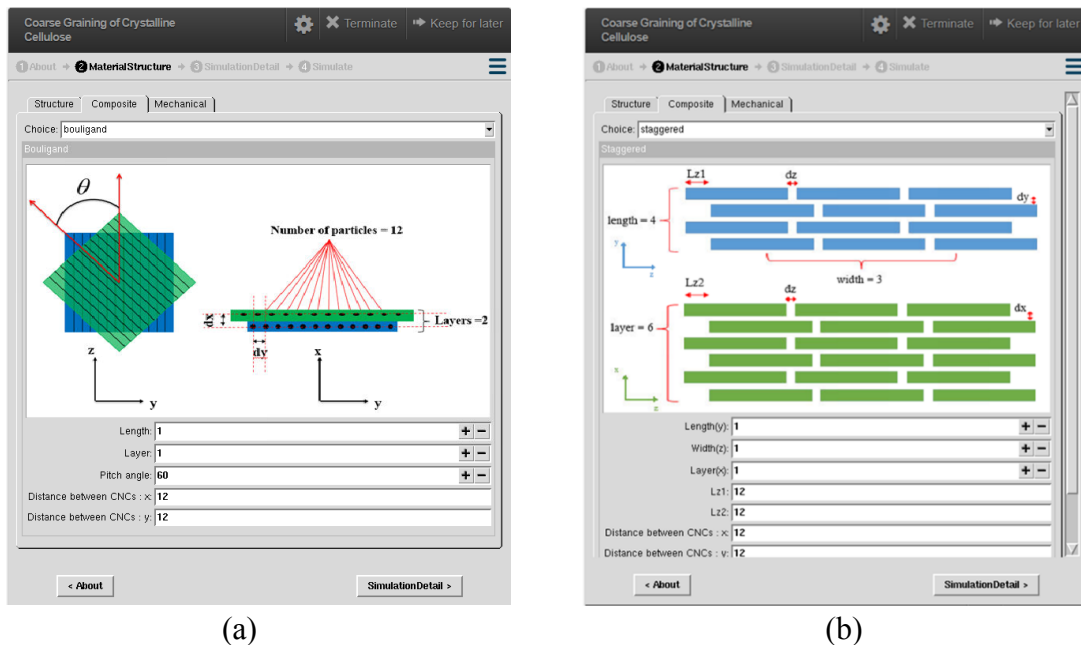
(a)

(b)



(c)

Figure A.1 (a) Bio-inspired crystalline nano-cellulose toolkit. (b) The structure tab in the toolkit allows the user to choose different cross-sections and length for CNCs. (c) Different type and size of cross-section for CNCs are shown. The 6x6 diamond and hexagonal shapes have been mostly employed in the past.



(a)

(b)

Figure A.2 In composite tab, one can choose to generate a staggered or a bouligand structure. (a) In the Bouligand tab, the number of particles in each layer, the pitch angle between layers and the distance between CNCs in and between layers can be modified. (b) The 3D staggered structure can be generated with multiple options on the overlap length in each direction.

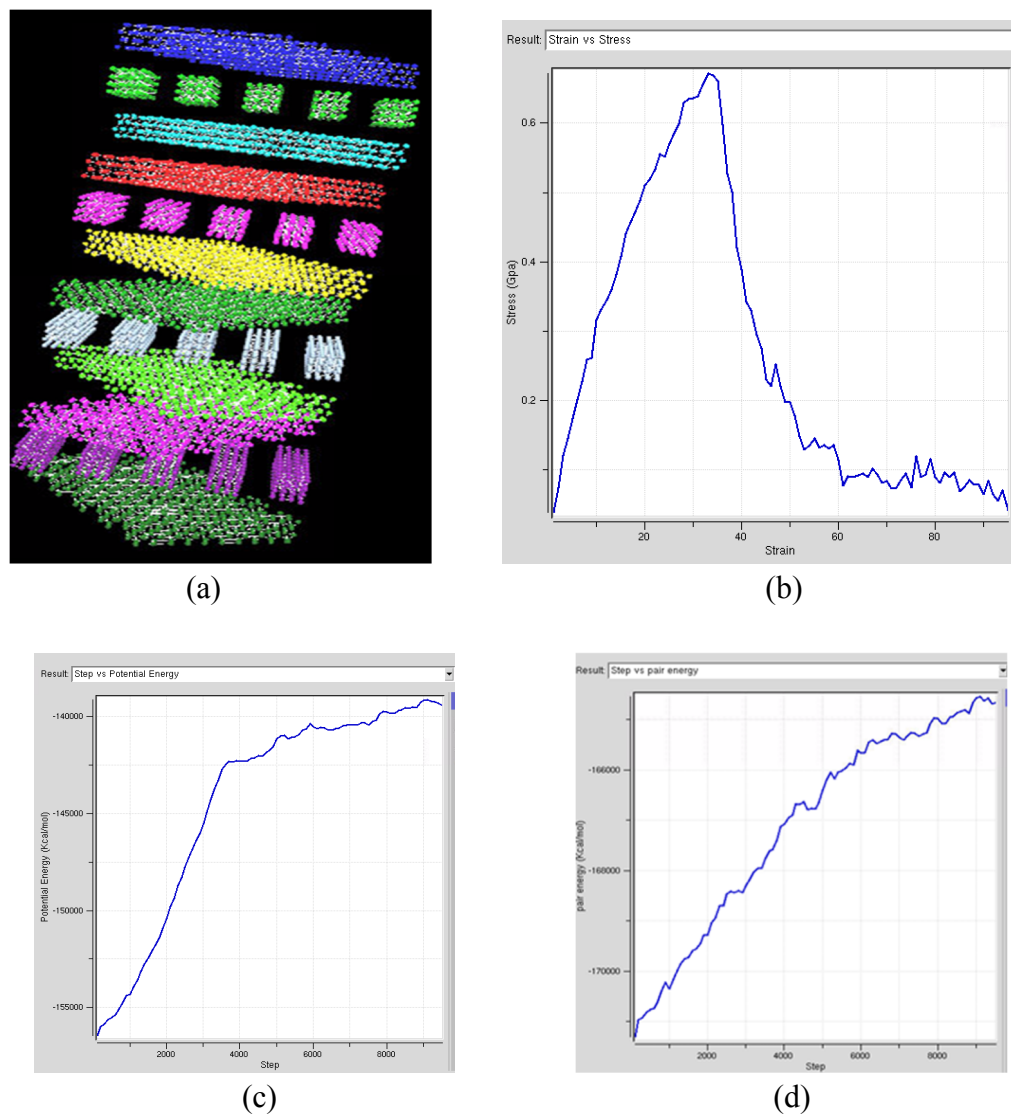


Figure A.3 The outputs from the tool is the generated structure in form of image and data structure and log files. (a) An example of generated Bouliagnd structure with 60 degree pitch angle. (b) the stress-strain curve for the tensile test. (c) Step-potential energy plot shows the variation of potential energy during the tensile test. (d) Step-pair energy plot illustrates the change in non-bonded energy during the tensile test.

APPENDIX B. MECHANICS OF CRYSTALLINE NANO CELLULOSE NANOFILM

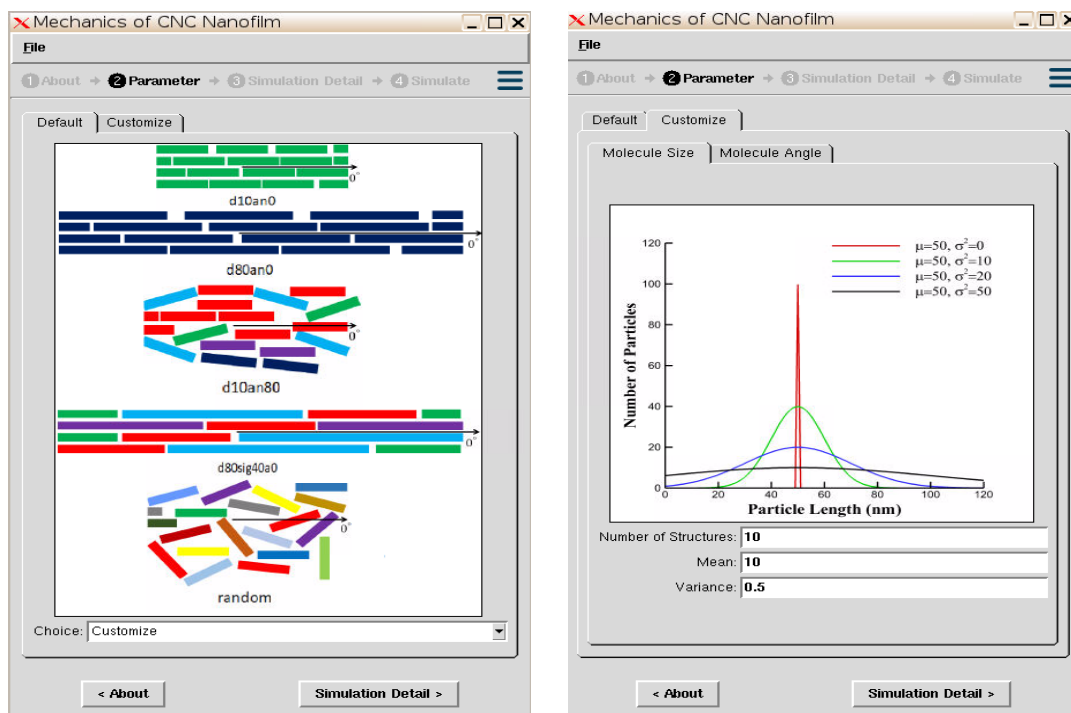
(A version of this chapter is published [doi:10.4231/D3TT4FW0D](https://doi.org/10.4231/D3TT4FW0D))

To study the effect of CNCs alignment on the mechanical properties, a new nanohub toolkit called “Mechanics of Crystalline Nano Cellulose Nanofilm” was developed (J. Leonardo, M. Shishehbor, 2017; Leonardo et al., 2017).

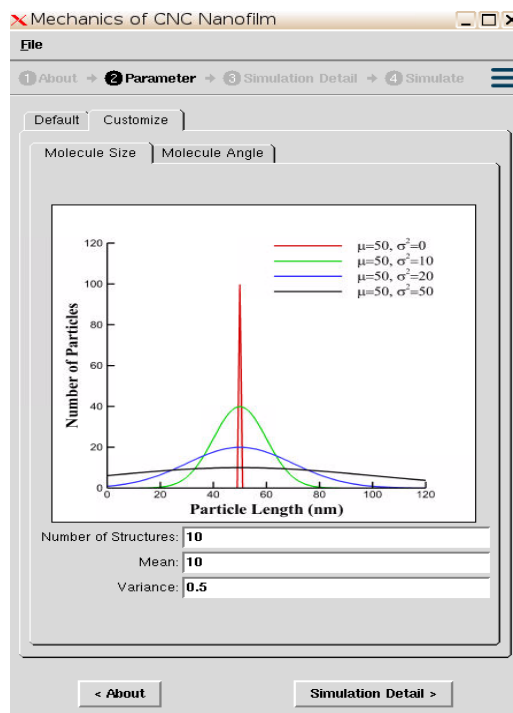
In addition to our modelling technique, we would also change our design on the input interface several times. The initial design would only consist of two tabs. One of the tabs would consist an input of number particles, length of each particles and length variance among the particles and the other tab would contain angle of each particle and the angle variance among the CNC particles. However, we reconsidered adding a preset files as generating a structures out of these parameters would take a significant amount of time. So, we added 5 preset settings that would make the process of visualization faster.

As for the output interface, we designed two parts for different purposes. We would give the user the ability to choose if they only want to visualize their own structure of Crystalline Nano Cellulose or conduct the tensile/mechanical test on the CNC structures they generated. The user would also be able to specify what kind of tensile test they want to conduct; whether it is along the x, y or z-axis. As for the total visualization part, we also let the user to choose what kind of Crystalline Nano Cellulose Structures they want to generate; it would be either the regular version or the simplified version that would only

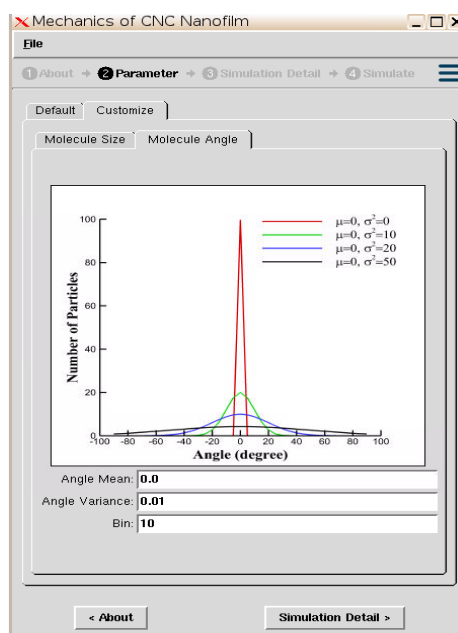
represent a CNC structure with a stick. The user input interface would start with a parameter tab which contain two main tabs such shown in Figure B.1. There is a default tab which determine if the user wants to generate preset CNC structures which has geometrics and shape that were carefully chosen.



(a)



(b)



(c)

Figure B.1 User could select a preset Crystalline Nano Cellulose Structures to speed up the visualization.

The first presents, d10an0, structures indicate homogenous CNC molecules that is mostly aligned. The second preset, d80an0, indicates longer CNC molecules, if compared to those in d10an0, that is still mostly aligned. On the third preset structure, d10an80, shows some CNC molecules that has the same length as the first, but with less alignment. On the third preset structure, d80sig40a0, we could see a completely aligned CNC molecules with different lengths throughout the structures. Finally, we would provide a completely randomized CNC structures as indicated by the name “random”. In addition, we also gave the user the ability to choose a customization option which would lead to Figure B.2. In the Customize tab, there are 3 parameters that are essential in forming different CNC structures: number of CNC molecules, length of each CNC molecule, length variance of the molecules, angular alignment of each molecules and the variance of the angular values. By changing these parameters, the user would significantly change the visualization of the CNC structures.

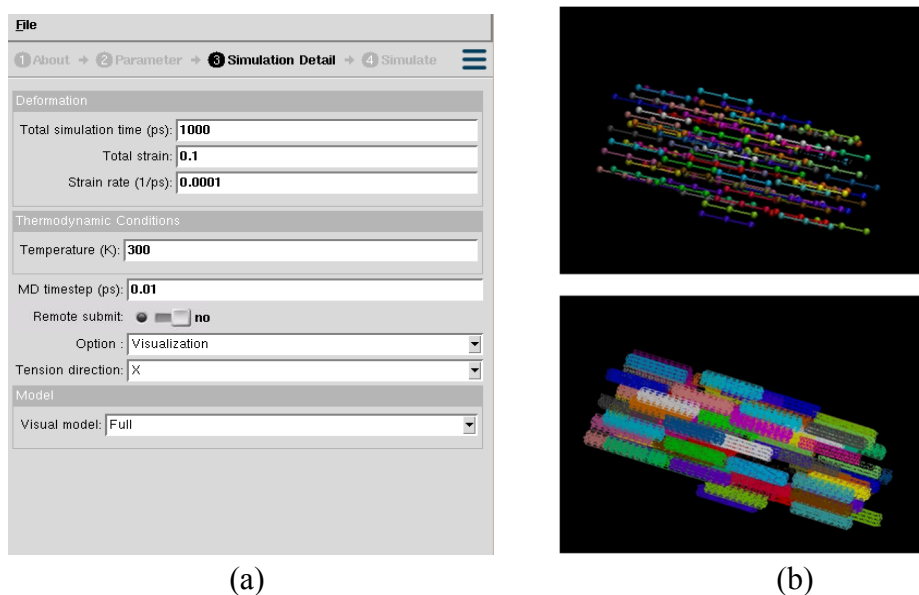
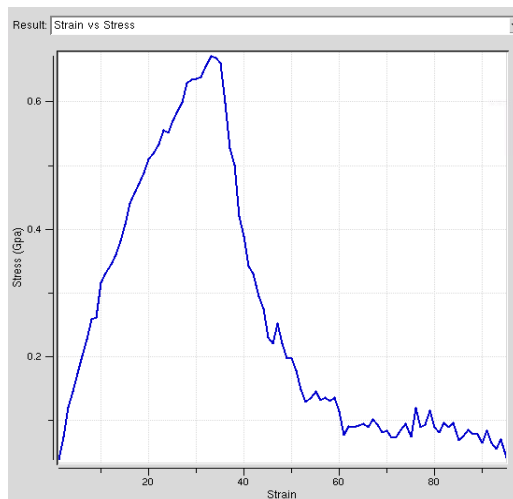


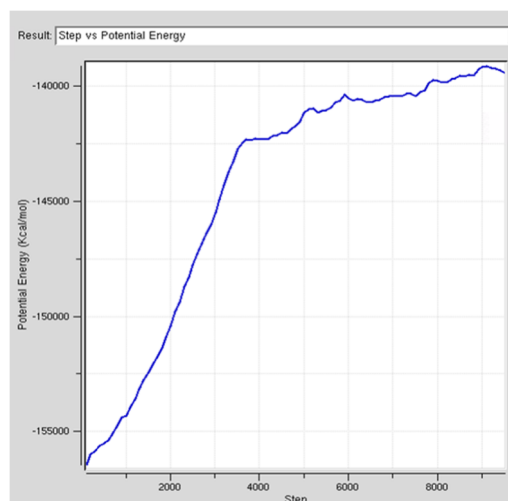
Figure B.2 Simulation details. (a) Options to choose different simulation time, temperature and visualization option. (b) Different visualization options are shown.

After going through the Parameter tab, user would stumble upon another input tab called “Simulation detail” tab. This tab would contain all the details about how the user want the simulation to run. User can specify run time, mechanical force, and temperature and CPU cores to use options. The option to whether to conduct the mechanical test or view the structure chosen is shown at the Option selection on Figure B.2. There is also the selection on what axis does the user want the tensile test to be conducted along and also whether the user want to have a structure visualization or the simplified one which would be explained in Figure B.2. As for the output, we would provide a interactive 3D visualization of the CNC structures such in Figure B.2, could be both the simplified version or the regular version, and the DATA file that contains the coordinate and bond information on the CNC structure generated if the user choose the option “Visualization” on the “Option” selection

in Simulation detail. However, if the user chooses the option “Equilibration”, the simulation would provide a video on how the CNC structure would react under a specified tensile test. As the option of tensile direction in “Simulation detail” specified, the X, Y and Z direction specified on how the tensile test is going to be conducted along. In addition to the video response of the test, users would also get the response graph as the output which could explain the trend observed from the simulation as shown in Figure B.3.



(a)



(b)

Figure B.3 Output of the tool (a) Stress-strain curve. (b) Potential energy-step curve

REFERENCES

- Abberton, B.C., Liu, W.K., Keten, S., 2013. Coarse-grained simulation of molecular mechanisms of recovery in thermally activated shape-memory polymers. *J. Mech. Phys. Solids* 61, 2625–2637. <https://doi.org/10.1016/j.jmps.2013.08.003>
- andersen, H.C., 1983. Rattle: A “velocity” version of the shake algorithm for molecular dynamics calculations. *J. Comput. Phys.* 52, 24–34. [https://doi.org/10.1016/0021-9991\(83\)90014-1](https://doi.org/10.1016/0021-9991(83)90014-1)
- Arash, B., Park, H.S., Rabczuk, T., 2015. Mechanical properties of carbon nanotube reinforced polymer nanocomposites: A coarse-grained model. *Compos. Part B Eng.* 80, 92–100. <https://doi.org/10.1016/j.compositesb.2015.05.038>
- Arash, B., Wang, Q., 2014. A Review on the Application of Nonlocal Elastic Models in Modeling of Carbon Nanotubes and Graphenes. *Springer Ser. Mater. Sci.* 188, 57–82. https://doi.org/10.1007/978-3-319-01201-8_2
- Arroyo, M., Belytschko, T., 2004. Finite element methods for the non-linear mechanics of crystalline sheets and nanotubes. *Int. J. Numer. Methods Eng.* 59, 419–456.
- Arroyo, M., Belytschko, T., 2002. An atomistic-based finite deformation membrane for single layer crystalline films. *J. Mech. Phys. Solids* 59, 1941–1947. [https://doi.org/10.1016/S0022-5096\(02\)00002-9](https://doi.org/10.1016/S0022-5096(02)00002-9)
- Barthelat, F., 2014. Designing nacre-like materials for simultaneous stiffness, strength and toughness: Optimum materials, composition, microstructure and size. *J. Mech. Phys. Solids* 73, 22–37. <https://doi.org/10.1016/j.jmps.2014.08.008>
- Barthelat, F., Dastjerdi, A.K., Rabiei, R., 2013. An improved failure criterion for biological and engineered staggered composites. *J. R. Soc. Interface* 10, 20120849–20120849. <https://doi.org/10.1098/rsif.2012.0849>
- Bergensträhle, M., Berglund, L.A., Mazeau, K., 2007. Thermal response in crystalline β cellulose: A molecular dynamics study. *J. Phys. Chem. B* 111, 9138–9145. <https://doi.org/10.1021/jp072258i>
- Brooks, B.R., Bruccoleri, R.E., Olafson, B.D., States, D.J., Swaminathan, S., Karplus, M., 1983. CHARMM: A program for macromolecular energy, minimization, and dynamics calculations. *J. Comput. Chem.* 4, 187–217. <https://doi.org/10.1002/jcc.540040211>
- Buehler, M.J., 2011. Multiscale aspects of mechanical properties of biological materials. *J. Mech. Behav. Biomed. Mater.* 4, 125–127. <https://doi.org/10.1016/j.jmbbm.2010.12.018>
- Buehler, M.J., 2008a. Atomistic modeling of materials failure, *Atomistic Modeling of Materials Failure*. Springer Science & Business Media. <https://doi.org/10.1007/978-0-387-76426-9>
- Buehler, M.J., 2008b. Atomistic modeling of materials failure, *Atomistic Modeling of Materials Failure*. <https://doi.org/10.1007/978-0-387-76426-9>
- Buehler, M.J., 2006a. Atomistic and continuum modeling of mechanical properties of collagen: Elasticity, fracture, and self-assembly. *J. Mater. Res.* 21, 1947–1961. <https://doi.org/10.1557/jmr.2006.0236>

- Buehler, M.J., 2006b. Mesoscale modelling of mechanics of carbon nanotubes: Self-assembly, self-folding, and fracture. *J. Mater. Res.* 21, 2855–2869. <https://doi.org/10.1557/jmr.2006.0347>
- Buehler, M.J., Ackbarow, T., 2007. Fracture mechanics of protein materials. *Mater. Today.* [https://doi.org/10.1016/S1369-7021\(07\)70208-0](https://doi.org/10.1016/S1369-7021(07)70208-0)
- Cao, G.X., Chen, X., 2006. Buckling of single-walled carbon nanotubes upon bending: Molecular dynamics simulations and finite element method. *Phys. Rev. B* 73, 155435. <https://doi.org/10.1103/PhysRevB.73.155435>
- Cao, Y., Tian, N., Bahr, D., Zavattieri, P.D., Youngblood, J., Moon, R.J., Weiss, J., 2016a. The influence of cellulose nanocrystals on the microstructure of cement paste. *Cem. Concr. Compos.* 74, 164–173. <https://doi.org/10.1016/j.cemconcomp.2016.09.008>
- Cao, Y., Zavaterra, P., Youngblood, J., Moon, R., Weiss, J., 2015. The influence of cellulose nanocrystal additions on the performance of cement paste. *Cem. Concr. Compos.* 56, 73–83. <https://doi.org/10.1016/j.cemconcomp.2014.11.008>
- Cao, Y., Zavattieri, P., Youngblood, J., Moon, R., Weiss, J., 2016b. The relationship between cellulose nanocrystal dispersion and strength. *Constr. Build. Mater.* 119, 71–79. <https://doi.org/10.1016/j.conbuildmat.2016.03.077>
- Carpenter, A.W., De Lannoy, C.F., Wiesner, M.R., 2015. Cellulose nanomaterials in water treatment technologies. *Environ. Sci. Technol.* 49, 5277–5287. <https://doi.org/10.1021/es506351r>
- Chang, I.-L., 2013. Molecular dynamics investigation of carbon nanotube resonance. *Model. Simul. Mater. Sci. Eng.* 21, 45011. <https://doi.org/10.1088/0965-0393/21/4/045011>
- Chang, T., Hou, J., Hou, J., 2013. Molecular dynamics simulations on buckling of multiwalled carbon nanotubes under bending. *J. Appl. Phys.* 114327, 114327. <https://doi.org/10.1063/1.2400096>
- Chen, P., Ogawa, Y., Nishiyama, Y., Ismail, A.E., Mazeau, K., 2016. Linear, non-linear and plastic bending deformation of cellulose nanocrystals. *Phys. Chem. Chem. Phys.* 18, 19880–19887. <https://doi.org/10.1039/c6cp00624h>
- Chen, S., Schueneman, G., Pipes, R.B., Youngblood, J., Moon, R.J., 2014. Effects of crystal orientation on cellulose nanocrystals-cellulose acetate nanocomposite fibers prepared by dry spinning. *Biomacromolecules* 15, 3827–3835. <https://doi.org/10.1021/bm501161v>
- Cheng, L., Thomas, A., Glancey, J.L., Karlsson, A.M., 2011. Mechanical behavior of bio-inspired laminated composites. *Compos. Part A Appl. Sci. Manuf.* 42, 211–220. <https://doi.org/10.1016/j.compositesa.2010.11.009>
- Chenoweth, K., van Duin, A.C.T., Goddard, W.A., 2008. ReaxFF Reactive Force Field for Molecular Dynamics Simulations of Hydrocarbon Oxidation. *J. Phys. Chem. A* 112, 1040–1053. <https://doi.org/10.1021/jp709896w>
- Chowdhury, R.A., Peng, S.X., Youngblood, J., 2017. Improved order parameter (alignment) determination in cellulose nanocrystal (CNC) films by a simple optical birefringence method. *Cellulose* 24, 1957–1970. <https://doi.org/10.1007/s10570-017-1250-9>

- Demille, R.C., Molinero, V., 2009. Coarse-grained ions without charges: Reproducing the solvation structure of NaCl in water using short-ranged potentials. *J. Chem. Phys.* 131, 34107. <https://doi.org/10.1063/1.3170982>
- Dri, F.L., 2012. Multiscale modeling of the hierarchical structure of cellulose nanocrystals. Thesis (Ph.D.)--Purdue University, 2013. .
- Dri, F.L., Hector, L.G., Moon, R.J., Zavattieri, P.D., 2013. Anisotropy of the elastic properties of crystalline cellulose I β from first principles density functional theory with Van der Waals interactions. *Cellulose* 20, 2703–2718. <https://doi.org/10.1007/s10570-013-0071-8>
- Dri, F.L., Wu, X., Moon, R.J., Martini, A., Zavattieri, P.D., 2015. Evaluation of reactive force fields for prediction of the thermo-mechanical properties of cellulose I β . *Comput. Mater. Sci.* 109, 330–340. <https://doi.org/10.1016/j.commatsci.2015.06.040>
- Dufresne, A., 2017. Nanocellulose: From nature to high performance tailored materials, 2. Edition, *Nanocellulose: From Nature to High Performance Tailored Materials*, 2. Edition. <https://doi.org/10.1515/9783110480412>
- Dufresne, A., 2013. Nanocellulose: A new ageless bionanomaterial. *Mater. Today* 16, 220–227. <https://doi.org/10.1016/j.mattod.2013.06.004>
- Eichhorn, S.J., Davies, G.R., 2006. Modelling the crystalline deformation of native and regenerated cellulose. *Cellulose* 13, 291–307. <https://doi.org/10.1007/s10570-006-9046-3>
- Espinosa, H.D., Rim, J.E., Barthelat, F., Buehler, M.J., 2009. Merger of structure and material in nacre and bone--Perspectives on *de novo* biomimetic materials. *Prog. Mater. Sci.* 54, 1059–1100.
- Fan, B., Maranas, J.K., 2015. Coarse-grained simulation of cellulose I β with application to long fibrils. *Cellulose* 22, 31–44. <https://doi.org/10.1007/s10570-014-0481-2>
- Fish, J., Belytschko, T., 2007. A First Course in Finite Elements, in: *A First Course in Finite Elements*. John Wiley & Sons, Ltd, pp. 1–319. <https://doi.org/10.1002/9780470510858>
- Fu, S.Y., Feng, X.Q., Lauke, B., Mai, Y.W., 2008. Effects of particle size, particle/matrix interface adhesion and particle loading on mechanical properties of particulate-polymer composites. *Compos. Part B Eng.* 39, 933–961. <https://doi.org/10.1016/j.compositesb.2008.01.002>
- Gao, H., 2006. Application of fracture mechanics concepts to hierarchical biomechanics of bone and bone-like materials. *Int. J. Fract.* 138, 101–137. <https://doi.org/10.1007/s10704-006-7156-4>
- Gates, T.S., Odegard, G.M., Frankland, S.J.V., Clancy, T.C., 2005. Computational materials: Multi-scale modeling and simulation of nanostructured materials. *Compos. Sci. Technol.* 65, 2416–2434. <https://doi.org/10.1016/j.compscitech.2005.06.009>
- Glass, D.C., Moritsugu, K., Cheng, X., Smith, J.C., 2012. REACH coarse-grained simulation of a cellulose fiber. *Biomacromolecules* 13, 2634–2644. <https://doi.org/10.1021/bm300460f>

- Graupner, N., Ziegmann, G., Wilde, F., Beckmann, F., Müssig, J., 2016. Procedural influences on compression and injection moulded cellulose fibre-reinforced polylactide (PLA) composites: Influence of fibre loading, fibre length, fibre orientation and voids. *Compos. Part A Appl. Sci. Manuf.* 81, 158–171. <https://doi.org/10.1016/j.compositesa.2015.10.040>
- Grishkewich, N., Mohammed, N., Tang, J., Tam, K.C., 2017. Recent advances in the application of cellulose nanocrystals. *Curr. Opin. Colloid Interface Sci.* 29, 32–45. <https://doi.org/10.1016/j.cocis.2017.01.005>
- Grunenfelder, L.K., Suksangpanya, N., Salinas, C., Milliron, G., Yaraghi, N., Herrera, S., Evans-Lutterodt, K., Nutt, S.R., Zavattieri, P., Kisailus, D., 2014. Bio-inspired impact-resistant composites. *Acta Biomater.* 10, 3997–4008. <https://doi.org/10.1016/j.actbio.2014.03.022>
- Habibi, Y., Lucia, L.A., Rojas, O.J., 2010. Cellulose nanocrystals: Chemistry, self-assembly, and applications. *Chem. Rev.* 110, 3479–3500. <https://doi.org/10.1021/cr900339w>
- Hadden, J.A., French, A.D., Woods, R.J., 2013. Unraveling cellulose microfibrils: A twisted tale. *Biopolymers* 99, 746–756. <https://doi.org/10.1002/bip.22279>
- Håkansson, K.M.O., Fall, A.B., Lundell, F., Yu, S., Krywka, C., Roth, S. V., Santoro, G., Kwick, M., Prahl Wittberg, L., Wågberg, L., Söderberg, L.D., 2014. Hydrodynamic alignment and assembly of nanofibrils resulting in strong cellulose filaments. *Nat. Commun.* 5. <https://doi.org/10.1038/ncomms5018>
- Hanley, S.J., Revol, J.F., Godbout, L., Gray, D.G., 1997. Atomic force microscopy and transmission electron microscopy of cellulose from *Micrasterias denticulata*; evidence for a chiral helical microfibril twist. *Cellulose* 4, 209–220. <https://doi.org/10.1023/A:1018483722417>
- Heiner, A.P., Kuutti, L., Teleman, O., 1998. Comparison of the interface between water and four surfaces of native crystalline cellulose by molecular dynamics simulations. *Carbohydr. Res.* 306, 205–220. [https://doi.org/10.1016/S0008-6215\(97\)10053-2](https://doi.org/10.1016/S0008-6215(97)10053-2)
- Hsu, D.D., Xia, W., Arturo, S.G., Keten, S., 2014. Systematic method for thermomechanically consistent coarse-graining: A universal model for methacrylate-based polymers. *J. Chem. Theory Comput.* 10, 2514–2527. <https://doi.org/10.1021/ct500080h>
- Huq, T., Salmieri, S., Khan, A., Khan, R.A., Le Tien, C., Riedl, B., Frascini, C., Bouchard, J., Uribe-Calderon, J., Kamal, M.R., Lacroix, M., 2012. Nanocrystalline cellulose (NCC) reinforced alginate based biodegradable nanocomposite film. *Carbohydr. Polym.* 90, 1757–1763. <https://doi.org/10.1016/j.carbpol.2012.07.065>
- Hynninen, A.P., Matthews, J.F., Beckham, G.T., Crowley, M.F., Nimlos, M.R., 2011. Coarse-grain model for glucose, cellobiose, and cellotetraose in water. *J. Chem. Theory Comput.* 7, 2137–2150. <https://doi.org/10.1021/ct200092t>
- Iwamoto, S., Kai, W., Isogai, A., Iwata, T., 2009. Elastic modulus of single cellulose microfibrils from tunicate measured by atomic force microscopy. *Biomacromolecules* 10, 2571–2576. <https://doi.org/10.1021/bm900520n>

- J. Leonardo, M. Shishehbor, P.Z., 2017. Mechanics of Crystalline Nano Cellulose Nanofilm. <https://doi.org/doi:10.4231/D3TT4FW0D>
- Jancar, J., Douglas, J.F., Starr, F.W., Kumar, S.K., Cassagnau, P., Lesser, A.J., Sternstein, S.S., Buehler, M.J., 2010. Current issues in research on structure-property relationships in polymer nanocomposites. *Polymer (Guildf)*. 51, 3321–3343. <https://doi.org/10.1016/j.polymer.2010.04.074>
- Jarvis, M., 2003. Cellulose stacks up. *Nature* 426, 611–612. <https://doi.org/10.1038/426611a>
- Jiang, L.Y., Huang, Y., Jiang, H., Ravichandran, G., Gao, H., Hwang, K.C., Liu, B., 2006. A cohesive law for carbon nanotube/polymer interfaces based on the van der Waals force. *J. Mech. Phys. Solids* 54, 2436–2452. <https://doi.org/10.1016/j.jmps.2006.04.009>
- Jin, K., Qin, Z., Buehler, M.J., 2015. Molecular deformation mechanisms of the wood cell wall material. *J. Mech. Behav. Biomed. Mater.* 42, 198–206. <https://doi.org/10.1016/j.jmbbm.2014.11.010>
- Karakasidis, T.E., Charitidis, C.A., 2007. Multiscale modeling in nanomaterials science. *Mater. Sci. Eng. C* 27, 1082–1089. <https://doi.org/10.1016/j.msec.2006.06.029>
- Kirschner, K.N., Yongye, A.B., Tschampel, S.M., González-Outeiriño, J., Daniels, C.R., Foley, B.L., Woods, R.J., 2008. GLYCAM06: A generalizable biomolecular force field. *carbohydrates. J. Comput. Chem.* 29, 622–655. <https://doi.org/10.1002/jcc.20820>
- Klemm, D., Heublein, B., Fink, H.P., Bohn, A., 2005. Cellulose: Fascinating biopolymer and sustainable raw material. *Angew. Chemie - Int. Ed.* <https://doi.org/10.1002/anie.200460587>
- Klemm, D., Kramer, F., Moritz, S., Lindström, T., Ankerfors, M., Gray, D., Dorris, A., 2011. Nanocelluloses: A new family of nature-based materials. *Angew. Chemie - Int. Ed.* 50, 5438–5466. <https://doi.org/10.1002/anie.201001273>
- Kohn, W., Becke, A.D., Parr, R.G., 1996. Density functional theory of electronic structure. *J. Phys. Chem.* 100, 12974–12980. <https://doi.org/10.1021/jp960669l>
- Kong, K., Eichhorn, S.J., 2005. The influence of hydrogen bonding on the deformation micromechanics of cellulose fibers. *J. Macromol. Sci. - Phys.* 44 B, 1123–1136. <https://doi.org/10.1080/00222340500324597>
- Kroon-Batenburg, L.M.J., Kroon, J., 1997. The crystal and molecular structures of cellulose I and II, in: *Glycoconjugate Journal*. pp. 677–690. <https://doi.org/10.1023/A:1018509231331>
- Kubicki, J.D., Watts, H.D., Zhao, Z., Zhong, L., 2014. Quantum mechanical calculations on cellulose-water interactions: Structures, energetics, vibrational frequencies and NMR chemical shifts for surfaces of I α and I β cellulose. *Cellulose* 21, 909–926. <https://doi.org/10.1007/s10570-013-0029-x>
- Lahiji, R.R., Xu, X., Reifenberger, R., Raman, A., Rudie, A., Moon, R.J., 2010. Atomic force microscopy characterization of cellulose nanocrystals. *Langmuir* 26, 4480–4488. <https://doi.org/10.1021/la903111j>

- Langan, P., Sukumar, N., Nishiyama, Y., Chanzy, H., 2005. Synchrotron X-ray structures of cellulose I β and regenerated cellulose II at ambient temperature and 100 K. *Cellulose* 12, 551–562. <https://doi.org/10.1007/s10570-005-9006-3>
- Launey, M.E., Buehler, M.J., Ritchie, R.O., 2010. On the Mechanistic Origins of Toughness in Bone. *Annu. Rev. Mater. Res.* 40, 25–53. <https://doi.org/10.1146/annurev-matsci-070909-104427>
- Leach, A., 2001. Need this Book.PDF.
- Lee, K.Y., Aitomäki, Y., Berglund, L.A., Oksman, K., Bismarck, A., 2014. On the use of nanocellulose as reinforcement in polymer matrix composites. *Compos. Sci. Technol.* <https://doi.org/10.1016/j.compscitech.2014.08.032>
- Leonardo, J., Shishehbor, M., Zavattieri, P.D., 2017. Development of a NanoHUB Tool: Mechanical Features of Crystalline Nano Cellulose. <https://doi.org/10.4231/D3TT4FW0D>
- Li, C., Chou, T.W., 2003. A structural mechanics approach for the analysis of carbon nanotubes. *Int. J. Solids Struct.* 40, 2487–2499. [https://doi.org/10.1016/S0020-7683\(03\)00056-8](https://doi.org/10.1016/S0020-7683(03)00056-8)
- Li, L., Pérré, P., Frank, X., Mazeau, K., 2015. A coarse-grain force-field for xylan and its interaction with cellulose. *Carbohydr. Polym.* 127, 438–450. <https://doi.org/10.1016/j.carbpol.2015.04.003>
- Li, X., Chang, W.C., Chao, Y.J., Wang, R., Chang, M., 2004. Nanoscale structural and mechanical characterization of a natural nanocomposite material: The shell of red abalone. *Nano Lett.* 4, 613–617. <https://doi.org/10.1021/nl049962k>
- Lin, N., Dufresne, A., 2014. Nanocellulose in biomedicine: Current status and future prospect. *Eur. Polym. J.* 59, 302–325. <https://doi.org/10.1016/j.eurpolymj.2014.07.025>
- Lin, N., Huang, J., Chang, P.R., Feng, J., Yu, J., 2011. Surface acetylation of cellulose nanocrystal and its reinforcing function in poly(lactic acid). *Carbohydr. Polym.* 83, 1834–1842. <https://doi.org/10.1016/j.carbpol.2010.10.047>
- Lindman, B., Karlström, G., Stigsson, L., 2010. On the mechanism of dissolution of cellulose. *J. Mol. Liq.* 156, 76–81. <https://doi.org/10.1016/j.molliq.2010.04.016>
- Lotz, B., Cheng, S.Z.D., 2005. A critical assessment of unbalanced surface stresses as the mechanical origin of twisting and scrolling of polymer crystals. *Polymer (Guildf)*. 46, 577–610. <https://doi.org/10.1016/j.polymer.2004.07.042>
- Luo, J., Chang, H., Bakhtiary Davijani, A.A., Liu, H.C., Wang, P.H., Moon, R.J., Kumar, S., 2017. Influence of high loading of cellulose nanocrystals in polyacrylonitrile composite films. *Cellulose* 24, 1745–1758. <https://doi.org/10.1007/s10570-017-1219-8>
- MacKerell, A.D., Raman, E.P., Guvench, O., 2010. CHARMM additive all-atom force field for glycosidic linkages in carbohydrates involving furanoses. *J. Phys. Chem. B* 114, 12981–12994. <https://doi.org/10.1021/jp105758h>
- Mariano, M., El Kissi, N., Dufresne, A., 2014. Cellulose nanocrystals and related nanocomposites: Review of some properties and challenges. *J. Polym. Sci. Part B Polym. Phys.* <https://doi.org/10.1002/polb.23490>

- Marshall, J., Dayal, K., 2013. Atomistic-to-Continuum Multiscale Modeling with Long-Range Electrostatic Interactions in Ionic Solids arXiv : 1310 . 2500v1 [cond-mat . mes-hall] 9 Oct 2013. *J. Mech. Phys. Solids* 62, 1–38.
- Martinez, L., andrade, R., Birgin, E.G., Martínez, J.M., 2009. PACKMOL: A package for building initial configurations for molecular dynamics simulations. *J. Comput. Chem.* 30, 2157–2164. <https://doi.org/10.1002/jcc.21224>
- Matthews, J.F., Beckham, G.T., Bergensträhle-Wohlert, M., Brady, J.W., Himmel, M.E., Crowley, M.F., 2012. Comparison of cellulose I β simulations with three carbohydrate force fields. *J. Chem. Theory Comput.* 8, 735–748. <https://doi.org/10.1021/ct2007692>
- Matthews, J.F., Skopec, C.E., Mason, P.E., Zuccato, P., Torget, R.W., Sugiyama, J., Himmel, E., Brady, J.W., Himmel, M.E., Brady, J.W., 2006. Computer simulation studies of microcrystalline cellulose I b. *Carbohydr. Res.* 341, 138–152. <https://doi.org/10.1016/j.carres.2005.09.028>
- Mattsson, T.R., Lane, J.M.D., Cochrane, K.R., Desjarlais, M.P., Thompson, A.P., Pierce, F., Grest, G.S., 2010. First-principles and classical molecular dynamics simulation of shocked polymers. *Phys. Rev. B - Condens. Matter Mater. Phys.* 81. <https://doi.org/10.1103/PhysRevB.81.054103>
- Meng, Q., Li, B., Li, T., Feng, X.Q., 2017. A multiscale crack-bridging model of cellulose nanopaper. *J. Mech. Phys. Solids* 103, 22–39. <https://doi.org/10.1016/j.jmps.2017.03.004>
- Meng, Z., Soler-Crespo, R.A., Xia, W., Gao, W., Ruiz, L., Espinosa, H.D., Keten, S., 2017. A coarse-grained model for the mechanical behavior of graphene oxide. *Carbon N. Y.* 117, 476–487. <https://doi.org/10.1016/j.carbon.2017.02.061>
- Miao, C., Hamad, W.Y., 2013. Cellulose reinforced polymer composites and nanocomposites: A critical review. *Cellulose*. <https://doi.org/10.1007/s10570-013-0007-3>
- Moon, R.J., Martini, A., Nairn, J., Simonsen, J., Youngblood, J., 2011. Cellulose nanomaterials review: Structure, properties and nanocomposites. *Chem. Soc. Rev.* 40, 3941–3994. <https://doi.org/10.1039/c0cs00108b>
- Natarajan, B., Gilman, J.W., 2018. Bioinspired Bouligand cellulose nanocrystal composites: A review of mechanical properties. *Philos. Trans. R. Soc. A Math. Phys. Eng. Sci.* 376, 20170050. <https://doi.org/10.1098/rsta.2017.0050>
- Natarajan, B., Krishnamurthy, A., Qin, X., Emiroglu, C.D., Forster, A., Foster, E.J., Weder, C., Fox, D.M., Keten, S., Obrzut, J., Gilman, J.W., 2018. Binary Cellulose Nanocrystal Blends for Bioinspired Damage Tolerant Photonic Films. *Adv. Funct. Mater.* 1800032, 1–11. <https://doi.org/10.1002/adfm.201800032>
- Neyertz, S., Pizzi, A., Merlin, A., Maigret, B., Brown, D., Deglise, X., 2000. New all-atom force field for crystalline cellulose I. *J. Appl. Polym. Sci.* 78, 1939–1946. [https://doi.org/10.1002/1097-4628\(20001209\)78:11<1939::AID-APP130>3.0.CO;2-9](https://doi.org/10.1002/1097-4628(20001209)78:11<1939::AID-APP130>3.0.CO;2-9)

- Nishiyama, Y., Johnson, G.P., French, A.D., Forsyth, V.T., Langan, P., 2008. Neutron crystallography, molecular dynamics, and quantum mechanics studies of the nature of hydrogen bonding in cellulose I β . *Biomacromolecules* 9, 3133–3140. <https://doi.org/10.1021/bm800726v>
- Nishiyama, Y., Langan, P., Chanzy, H., 2002. Crystal structure and hydrogen-bonding system in cellulose I β from synchrotron X-ray and neutron fiber diffraction. *J. Am. Chem. Soc.* 124, 9074–9082. <https://doi.org/10.1021/ja0257319>
- Noid, W.G., 2013. Perspective: Coarse-grained models for biomolecular systems. *J. Chem. Phys.* 139, 90901. <https://doi.org/10.1063/1.4818908>
- Oostenbrink, C., Villa, A., Mark, A.E., Van Gunsteren, W.F., 2004. A biomolecular force field based on the free enthalpy of hydration and solvation: The GROMOS force-field parameter sets 53A5 and 53A6. *J. Comput. Chem.* 25, 1656–1676. <https://doi.org/10.1002/jcc.20090>
- Pakzad, A., Simonsen, J., Heiden, P.A., Yassar, R.S., 2012. Size effects on the nanomechanical properties of cellulose i nanocrystals. *J. Mater. Res.* 27, 528–536. <https://doi.org/10.1557/jmr.2011.288>
- Park, S., Khalili-Araghi, F., Tajkhorshid, E., Schulten, K., 2003. Free energy calculation from steered molecular dynamics simulations using Jarzynski's equality. *J. Chem. Phys.* 119, 3559–3566. <https://doi.org/10.1063/1.1590311>
- Peng, Y., Gardner, D.J., Han, Y., Cai, Z., Tshabalala, M.A., 2013. Influence of drying method on the surface energy of cellulose nanofibrils determined by inverse gas chromatography. *J. Colloid Interface Sci.* 405, 85–95. <https://doi.org/10.1016/j.jcis.2013.05.033>
- Plimpton, S., 2007. LAMMPS-large-scale atomic/molecular massively parallel simulator. *Sandia Natl. Lab.* 18. <https://doi.org/10.1002/ejoc.201200111>
- Poma, A.B., Chwastyk, M., Cieplak, M., 2017. Elastic moduli of biological fibers in a coarse-grained model: Crystalline cellulose and β -amyloids. *Phys. Chem. Chem. Phys.* 19, 28195–28206. <https://doi.org/10.1039/c7cp05269c>
- Potulski, D.C., De Muniz, G.I.B., Klock, U., De andrade, A.S., 2014. Influência da incorporação de celulose microfibrilada nas propriedades de resistência mecânicas do papel. *Sci. For. Sci.* 40, 345–351. <https://doi.org/10.1016/j.carbpol.2011.08.078>
- Problems, O., 2007. Finite Element Formulation for. *A First Course Finite Elem.* 5.
- Qin, X., Feng, S., Meng, Z., Keten, S., 2017. Optimizing the mechanical properties of cellulose nanopaper through surface energy and critical length scale considerations. *Cellulose* 24, 3289–3299. <https://doi.org/10.1007/s10570-017-1367-x>
- Quesada Cabrera, R., Meersman, F., McMillan, P.F., Dmitriev, V., 2011. Nanomechanical and structural properties of native cellulose under compressive stress. *Biomacromolecules* 12, 2178–2183. <https://doi.org/10.1021/bm200253h>
- Raabe, D., Sachs, C., Romano, P., 2005. The crustacean exoskeleton as an example of a structurally and mechanically graded biological nanocomposite material. *Acta Mater.* 53, 4281–4292. <https://doi.org/10.1016/j.actamat.2005.05.027>

- Rahaman, O., Van Duin, A.C.T., Goddard, W.A., Doren, D.J., 2011. Development of a ReaxFF reactive force field for glycine and application to solvent effect and tautomerization. *J. Phys. Chem. B* 115, 249–261. <https://doi.org/10.1021/jp108642r>
- Rahman, R., Foster, J.T., Haque, A., 2013. Molecular dynamics simulation and characterization of graphene-cellulose nanocomposites. *J. Phys. Chem. A* 117, 5344–5353. <https://doi.org/10.1021/jp402814t>
- Reising, A.B., Moon, R.J., Youngblood, J.P., 2012. Effect of Particle Alignment on Mechanical Property of Neat Cellulose Nanocrystal Films. *J. Sci. Technol. For. Prod. Process.* 2, 3–5.
- Rho, J.Y., Kuhn-Spearing, L., Zioupos, P., 1998. Mechanical properties and the hierarchical structure of bone. *Med. Eng. Phys.* 20, 92–102. [https://doi.org/10.1016/S1350-4533\(98\)00007-1](https://doi.org/10.1016/S1350-4533(98)00007-1)
- Ruiz, L., Xia, W., Meng, Z., Keten, S., 2015. A coarse-grained model for the mechanical behavior of multi-layer graphene. *Carbon* N. Y. 82, 103–115. <https://doi.org/10.1016/j.carbon.2014.10.040>
- Saito, T., Kuramae, R., Wohler, J., Berglund, L.A., Isogai, A., 2013. An ultrastrong nanofibrillar biomaterial: The strength of single cellulose nanofibrils revealed via sonication-induced fragmentation. *Biomacromolecules* 14, 248–253. <https://doi.org/10.1021/bm301674e>
- Sakurada, I., Nukushina, Y., Ito, T., 1962. Experimental determination of the elastic modulus of crystalline regions in oriented polymers. *J. Polym. Sci.* 57, 651–660. <https://doi.org/10.1002/pol.1962.1205716551>
- Sauer, R.A., Wriggers, P., 2009. Formulation and analysis of a three-dimensional finite element implementation for adhesive contact at the nanoscale. *Comput. Methods Appl. Mech. Eng.* 198, 3871–3883. <https://doi.org/10.1016/j.cma.2009.08.019>
- Scarpa, F., Adhikari, S., Srikantha Phani, A., 2009. Effective elastic mechanical properties of single layer graphene sheets. *Nanotechnology* 20, Art. No. 065709. <https://doi.org/10.1088/0957-4484/20/6/065709>
- Sehaqui, H., Ezekiel Mushi, N., Morimune, S., Salajkova, M., Nishino, T., Berglund, L.A., 2012. Cellulose nanofiber orientation in nanopaper and nanocomposites by cold drawing. *ACS Appl. Mater. Interfaces* 4, 1043–1049. <https://doi.org/10.1021/am2016766>
- Shishehbor, M., Dri, F.L., Moon, R.J., Zavattieri, P.D., 2018. A continuum-based structural modeling approach for cellulose nanocrystals (CNCs). *J. Mech. Phys. Solids* 111, 308–332. <https://doi.org/10.1016/j.jmps.2017.11.006>
- Shishehbor, M., Zavattieri, P.D., 2019. Coarse-grained Model for elasticity and fracture of Cellulose Nano Crystals (CNC) based materials. *Nanoscale*.
- Sinko, R., Keten, S., 2015. Traction-separation laws and stick-slip shear phenomenon of interfaces between cellulose nanocrystals. *J. Mech. Phys. Solids* 78, 526–539. <https://doi.org/10.1016/j.jmps.2015.02.012>
- Sinko, R., Mishra, S., Ruiz, L., Brandis, N., Keten, S., 2014. Dimensions of biological cellulose nanocrystals maximize fracture strength. *ACS Macro Lett.* 3, 64–69. <https://doi.org/10.1021/mz400471y>

- Soler, J.M., Artacho, E., Gale, J.D., García, A., Junquera, J., Ordejón, P., Sánchez-Portal, D., 2002. The SIESTA method for ab initio order-N materials simulation. *J. Phys. Condens. Matter* 14, 2745–2779. <https://doi.org/10.1088/0953-8984/14/11/302>
- Srinivas, G., Cheng, X., Smith, J.C., 2014. Coarse-grain model for natural cellulose fibrils in explicit water. *J. Phys. Chem. B* 118, 3026–3034. <https://doi.org/10.1021/jp407953p>
- Srinivas, G., Cheng, X., Smith, J.C., 2011. A solvent-free coarse grain model for crystalline and amorphous cellulose fibrils. *J. Chem. Theory Comput.* 7, 2539–2548. <https://doi.org/10.1021/ct200181t>
- Steinhauser, M.O., 2016. Computational multiscale modeling of fluids and solids: Theory and applications, second edition, Computational Multiscale Modeling of Fluids and Solids: Theory and Applications, Second Edition. <https://doi.org/10.1007/978-3-662-53224-9>
- Suksangpanya, N., Yaraghi, N.A., Kisailus, D., Zavattieri, P., 2017. Twisting cracks in Bouligand structures. *J. Mech. Behav. Biomed. Mater.* 76, 38–57. <https://doi.org/10.1016/j.jmbbm.2017.06.010>
- Sun, H., 1998. COMPASS: An ab Initio Force-Field Optimized for Condensed-Phase Applications Overview with Details on Alkane and Benzene Compounds. *J. Phys. Chem. B* 102, 7338–7364. <https://doi.org/10.1021/jp980939v>
- Takada, S., 2012. Coarse-grained molecular simulations of large biomolecules. *Curr. Opin. Struct. Biol.* 22, 130–137. <https://doi.org/10.1016/j.sbi.2012.01.010>
- Tanaka, F., Iwata, T., 2006. Estimation of the elastic modulus of cellulose crystal by molecular mechanics simulation. *Cellulose* 13, 509–517. <https://doi.org/10.1007/s10570-006-9068-x>
- Tian, K., Shishehbor, M., Zavattieri, P., 2016. Coarse Graining of Crystalline Cellulose. <https://doi.org/doi:10.4231/D3930NW4D>
- Tozzini, V., 2005. (CUL-ID:1485975) Coarse-grained models for proteins. *Curr. Opin. Struct. Biol.* 15, 144–150.
- Van Duin, A.C.T., Dasgupta, S., Lorant, F., Goddard, W.A., 2001. ReaxFF: A reactive force field for hydrocarbons. *J. Phys. Chem. A* 105, 9396–9409. <https://doi.org/10.1021/jp004368u>
- van Duin, A.C.T., Strachan, A., Stewman, S., Zhang, Q., Xu, X., Goddard, W.A., 2003. ReaxFF_{SiO} Reactive Force Field for Silicon and Silicon Oxide Systems. *J. Phys. Chem. A* 107, 3803–3811. <https://doi.org/10.1021/jp0276303>
- Wada, M., Chanzy, H., Nishiyama, Y., Langan, P., 2004. Cellulose III I crystal structure and hydrogen bonding by synchrotron X-ray and neutron fiber diffraction. *Macromolecules* 37, 8548–8555. <https://doi.org/10.1021/ma0485585>
- Wagner, R., Moon, R.J., Raman, A., 2016. Mechanical properties of cellulose nanomaterials studied by contact resonance atomic force microscopy. *Cellulose* 23, 1031–1041. <https://doi.org/10.1007/s10570-016-0883-4>

- Wang, B., Torres-Rendon, J.G., Yu, J., Zhang, Y., Walther, A., 2015. Aligned bioinspired cellulose nanocrystal-based nanocomposites with synergetic mechanical properties and improved hygromechanical performance. *ACS Appl. Mater. Interfaces* 7, 4595–4607. <https://doi.org/10.1021/am507726t>
- Wang, J., Wolf, R.M., Caldwell, J.W., Kollman, P.A., Case, D.A., 2004. Development and testing of a general Amber force field. *J. Comput. Chem.* 25, 1157–1174. <https://doi.org/10.1002/jcc.20035>
- Wang, S., Jiang, F., Xu, X., Kuang, Y., Fu, K., Hitz, E., Hu, L., 2017. Super-Strong, Super-Stiff Macrofibers with Aligned, Long Bacterial Cellulose Nanofibers. *Adv. Mater.* 29. <https://doi.org/10.1002/adma.201702498>
- Wang, S., Li, T., Chen, C., Kong, W., Zhu, S., Dai, J., Diaz, A.J., Hitz, E., Solares, S.D., Li, T., Hu, L., 2018. Transparent, Anisotropic Biofilm with Aligned Bacterial Cellulose Nanofibers. *Adv. Funct. Mater.* <https://doi.org/10.1002/adfm.201707491>
- Weaver, J.C., Milliron, G.W., Miserez, A., Evans-Lutterodt, K., Herrera, S., Gallana, I., Mershon, W.J., Swanson, B., Zavattieri, P., DiMasi, E., Kisailus, D., 2012. The stomatopod dactyl club: A formidable damage-tolerant biological hammer. *Science* (80-.). 336, 1275–1280. <https://doi.org/10.1126/science.1218764>
- Wei, X., Naraghi, M., Espinosa, H.D., 2012. Optimal length scales emerging from shear load transfer in natural materials: Application to carbon-based nanocomposite design. *ACS Nano* 6, 2333–2344. <https://doi.org/10.1021/nn204506d>
- Wohlert, J., Berglund, L.A., 2011. A coarse-grained model for molecular dynamics simulations of native cellulose. *J. Chem. Theory Comput.* 7, 753–760. <https://doi.org/10.1021/ct100489z>
- Wu, X., Moon, R.J., Martini, A., 2014. Tensile strength of I β crystalline cellulose predicted by molecular dynamics simulation. *Cellulose* 21, 2233–2245. <https://doi.org/10.1007/s10570-014-0325-0>
- Wu, X., Moon, R.J., Martini, A., 2013. Crystalline cellulose elastic modulus predicted by atomistic models of uniform deformation and nanoscale indentation. *Cellulose* 20, 43–55. <https://doi.org/10.1007/s10570-012-9823-0>
- Xia, W., Ruiz, L., Pugno, N.M., Keten, S., 2016. Critical length scales and strain localization govern the mechanical performance of multi-layer graphene assemblies. *Nanoscale* 8, 6456–6462. <https://doi.org/10.1039/c5nr08488a>
- Yakobson, B.I., Brabec, C.J., Bernholc, J., 1996. Nanomechanics of carbon tubes: Instabilities beyond linear response. *Phys. Rev. Lett.* 76, 2511–2514. <https://doi.org/10.1103/PhysRevLett.76.2511>
- Yang, J., Han, C.R., Zhang, X.M., Xu, F., Sun, R.C., 2014. Cellulose nanocrystals mechanical reinforcement in composite hydrogels with multiple cross-links: Correlations between dissipation properties and deformation mechanisms. *Macromolecules* 47, 4077–4086. <https://doi.org/10.1021/ma500729q>
- Yang, Y., Chen, Z., Song, X., Zhang, Z., Zhang, J., Shung, K.K., Zhou, Q., Chen, Y., 2017. Biomimetic Anisotropic Reinforcement Architectures by Electrically Assisted Nanocomposite 3D Printing. *Adv. Mater.* 29, 1605750. <https://doi.org/10.1002/adma.201605750>

- Yaraghi, N.A., Guarín-Zapata, N., Grunenfelder, L.K., Hintsala, E., Bhowmick, S., Hiller, J.M., Betts, M., Principe, E.L., Jung, J.Y., Sheppard, L., Wuhler, R., McKittrick, J., Zavattieri, P.D., Kisailus, D., 2016. Biocomposites: A Sinusoidally Architected Helicoidal Biocomposite (Adv. Mater. 32/2016). Adv. Mater. 28, 6769. <https://doi.org/10.1002/adma.201670219>
- Yazdandoost, F., Mirzaeifar, R., Qin, Z., Buehler, M.J., 2017. Multiscale mechanics of the lateral pressure effect on enhancing the load transfer between polymer coated CNTs. Nanoscale 9, 5565–5576. <https://doi.org/10.1039/c7nr00312a>
- Zavattieri, F.L.D. and S.S. and L.G.H.J. and P.S. and Z.-K.L. and R.J.M. and P.D., 2014. Anisotropy and temperature dependence of structural, thermodynamic, and elastic properties of crystalline cellulose I β : a first-principles investigation. Model. Simul. Mater. Sci. Eng. 22, 85012. <https://doi.org/10.1088/0965-0393/22/8/085012>
- Zhang, Y., Meng, Z., Qin, X., Keten, S., 2018. Ballistic impact response of lipid membranes. Nanoscale 10, 4761–4770. <https://doi.org/10.1039/c7nr08879e>
- Zhao, Z., Shklyaev, O.E., Nili, A., Mohamed, M.N.A., Kubicki, J.D., Crespi, V.H., Zhong, L., 2013. Cellulose microfibril twist, mechanics, and implication for cellulose biosynthesis. J. Phys. Chem. A 117, 2580–2589. <https://doi.org/10.1021/jp3089929>
- Zhong, L., Matthews, J.F., Crowley, M.F., Rignall, T., Talón, C., Cleary, J.M., Walker, R.C., Chukkapalli, G., McCabe, C., Nimlos, M.R., Brooks, C.L., Himmel, M.E., Brady, J.W., 2008. Interactions of the complete cellobiohydrolase I from *Trichodera reesei* with microcrystalline cellulose I β . Cellulose 15, 261–273. <https://doi.org/10.1007/s10570-007-9186-0>
- Zhu, H., Fang, Z., Preston, C., Li, Y., Hu, L., 2014. Transparent paper: Fabrications, properties, and device applications. Energy Environ. Sci. 7, 269–287. <https://doi.org/10.1039/c3ee43024c>
- Zhu, H., Zhu, S., Jia, Z., Parvinian, S., Li, Y., Vaaland, O., Hu, L., Li, T., 2015. Anomalous scaling law of strength and toughness of cellulose nanopaper. Proc. Natl. Acad. Sci. 112, 8971–8976. <https://doi.org/10.1073/pnas.1502870112>
- Zhu, M., Wang, Y., Zhu, S., Xu, L., Jia, C., Dai, J., Song, J., Yao, Y., Wang, Y., Li, Y., Henderson, D., Luo, W., Li, H., Minus, M.L., Li, T., Hu, L., 2017. Anisotropic, Transparent Films with Aligned Cellulose Nanofibers. Adv. Mater. 29. <https://doi.org/10.1002/adma.201606284>
- Zienkiewicz, O., Taylor, R., 2000. The finite element method: Solid mechanics, Vasa. Butterworth-heinemann.

VITA

Mehdi received his bachelor's degree in Civil Engineering at K.N.Toosi university, Tehran, Iran in 2009. He continued his career as a master student in structural Engineering at Sharif University of Technology, Tehran , Iran from 2009 to 2011 working on material modeling and simulation. In January 2013 he joined Prof. Pablo Zavattieri's group at Purdue university as a PhD student. Mehdi worked on multiple projects during his PhD and primarily, his main contribution was on Multiscale modeling of cellulose from nano-scale to continuum.